2007

A study of stone fragmentation in shock wave lithotripsy by customizing the acoustic field and waveform shape

BOSTON UNIVERSITY

COLLEGE OF ENGINEERING

Dissertation

A STUDY OF STONE FRAGMENTATION IN SHOCK WAVE LITHOTRIPSY BY CUSTOMIZING THE ACOUSTIC FIELD AND WAVEFORM SHAPE

by

PARAG VIJAY CHITNIS

B.S., West Virginia Wesleyan College, 2000

M.S., Boston University, 2002

Submitted in partial fulfillment of the

requirements for the degree of

Doctor of Philosophy

2007

Approved by

First Reader _____
Robin O. Cleveland
Associate Professor of Mechanical Engineering

Second Reader _____
Ronald A. Roy
Professor of Mechanical Engineering

Third Reader _____
Paul E. Barbone
Associate Professor of Mechanical Engineering

Fourth Reader _____
James A. McAteer
Professor of Anatomy and Cell Biology

doing my homework. When I was tired of studying or on those occasions when we were unsupervised, my little brother was there to play and to cause every mischief imaginable. My family has been behind me through every step of the way, academic or otherwise. I dedicate this dissertation to my parents, who have always been an inspiration to me.

As a student with no background in acoustics, I would have been at a total loss without a mentor like Prof. Robin Cleveland. Robin was patient and willing to give new students, who had yet to prove their mettle, a chance in his lab. He was also a wonderful teacher who taught me everything from how to work an oscilloscope to complex concepts in shock wave acoustics. It has been a privilege to be under his tutelage. From sending me to numerous conferences, to giving career advice, Robin did everything that could be expected from an academic advisor and more. Who else would be willing to read my dissertation five times and sit through the dry-run presentations multiple times?

I would be remiss if I did not include Profs. Ronald Roy and R. G. Holt in my list of mentors. Many thanks are due to them for keeping their doors open and answering my endless questions. Their presence was similar to having two additional advisors who guided me in the lab, provided me with invaluable knowledge about bubble dynamics, gave me career advice, and in the end provided with a new and exciting opportunity to further my research experience.

A STUDY OF STONE FRAGMENTATION IN SHOCK WAVE LITHOTRIPSY BY CUSTOMIZING THE ACOUSTIC FIELD AND WAVEFORM SHAPE

(Order No.   )

PARAG VIJAY CHITNIS

Boston University College of Engineering, 2007

Major Professor: Robin O. Cleveland, Associate Professor of Mechanical Engineering

ABSTRACT

Shock wave lithotripsy is the preferred treatment modality for kidney stones in the United States. Despite clinical use for over twenty-five years, the mechanisms of stone fragmentation are still under debate. A piezoelectric array was employed to examine the effect of waveform shape and pressure distribution on stone fragmentation in lithotripsy. The array consisted of 170 elements placed on the inner surface of a 15 cm-radius spherical cap. Each element was driven independently using a 170 individual pulsers, each capable of generating 1.2 kV. The acoustic field was characterized using a fiber optic probe hydrophone with a bandwidth of 30 MHz and a spatial resolution of 100 μm. When all elements were driven simultaneously, the focal waveform was a

shock wave with peak pressures p+ $= 65 \pm 3$ MPa and p$- = -16 \pm 2$ MPa and the -6 dB focal region was 13 mm long and 2 mm wide. The delay for each element was the only control parameter for customizing the acoustic field and waveform shape, which was done with the aim of investigating the hypothesized mechanisms of stone fragmentation such as spallation, shear, squeezing, and cavitation. The acoustic field customization was achieved by employing the angular spectrum approach for modeling the forward wave propagation and regression of least square errors to determine the optimal set of delays. Results from the acoustic field customization routine and its implications on stone fragmentation will be discussed.

Contents

List of Tables

List of Figures

xv

xvi

xvii

Chapter 1

Introduction

Kidney stones, also known as renal calculi, are formed due to crystallization of dissolved minerals in urine and are found in kidneys or ureters. Kidney stones typically leave the body in the urine stream, however, if they grow relatively large before passing (diameter > 2 mm), they can cause obstruction of ureter or distention of kidney with urine leading to severe pain. Kidney stones vary in size, shape, mineral composition [88], and mechanical strength [1, 22]. The more common mineral compositions of kidney stones include calcium oxalate monohydrate (which is the most common), calcium oxalate dihydrate, struvite, apatite, brushite, uric acid, and cystine.

Shock wave lithotripsy (SWL) was introduced in 1980 as a viable treatment for kidney stones. Chaussy et al. performed the first procedure of SWL on human patients [13]. SWL is a noninvasive technique based on focusing shock waves (SWs)

1

generated outside of the body onto the kidney stone to cause fragmentation. Exposing the stones to a large number of shock waves (1500−2500) reduces the stone to small fragments (diameter < 2 mm) that can pass through the urinary tract eliminating the need for surgical intervention. Due to its effectiveness and noninvasive nature, SWL has become the predominant method of treating kidney stones. Approximately 70% of kidney stone cases in the US are treated using SWL [53, 3].

The success of SWL stimulated the development of new systems based on generation and focusing of SWs [58]. Currently, lithotripters employ electrohydraulic, electromagnetic, or piezoelectric SW generation. The three lithotripters will be discussed in detail in the following section. Based on clinical studies, the gold standard for lithotripter based on treatment efficiency is one of the first generation devices: the Dornier HM3 lithotripters (Dornier Medical Systems, Germany) which employ the electrohydraulic principle for generating SWs [58].

1.1 Shock Wave Generation

The formation of a shock wave occurs when the amplitude of the acoustic wave is large enough that the perturbation of the medium leads to a small but significant variation in the wave speed from one point to another in the wave. Thus, different portions of the wave will travel at different speeds resulting in the distortion of the wave.

In particular, the speed of the positive peaks is the highest [65] and the nonlinear distortion results in steepening of the wave front which progresses until the slope approaches infinity. The infinite slope represents a discontinuity and is referred to as a 'shock' and the resulting wave is called a shock wave.

The waves produced by electromagnetic and piezoelectric lithotripters are not SWs to begin with and rely upon nonlinear distortion for formation of the shock front. The wave generated by the electrohydraulic method is a shock wave from the beginning. The details about the SW generation methods will be presented below along with their characteristics waveforms.

1.1.1 Electrohydraulic lithotripter

The electrohydraulic lithotripter (EHL) employs an electrical breakdown (spark) for generating SWs. The spark source is positioned at one of the two focii of a hemi-ellipsoidal reflector. Water surrounding the electrode is vaporized by the spark arcing across the electrode. The vapor bubble induces a spherical SW (the expansion is supersonic) which, after reflection, is focused at the second focus of the ellipse. The patient is positioned such that the stone is at the second focus (Fig. 1.1 (a)). A characteristic feature of the EHL is the substantial pressure fluctuations (up to 50%) between the individual SWs. The large variation in the SW pressure is largely due to randomness associated with the spark arcing across the electrode.
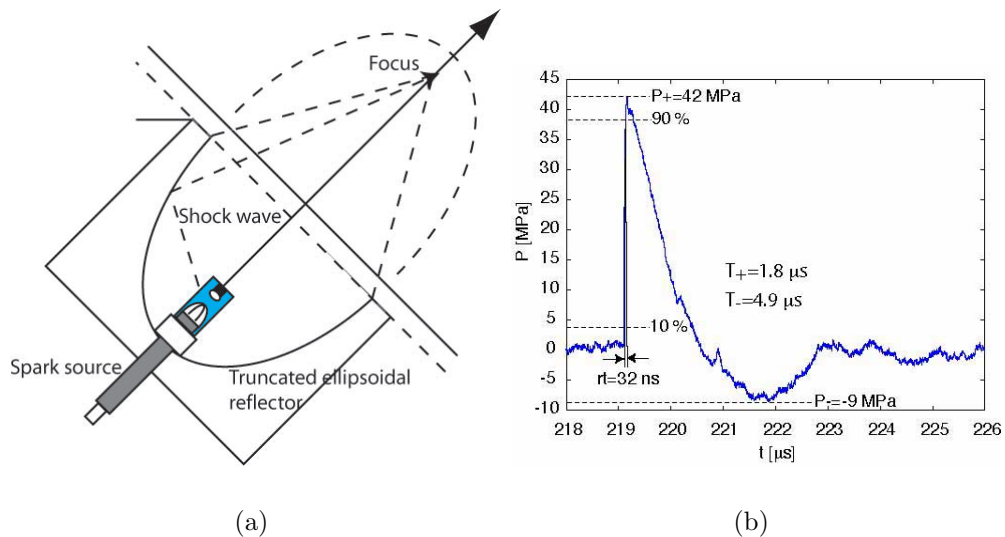
Figure 1.1: (a) Schematic for a clinical electrohydraulic lithotripter. (b) A typical shock wave measured at the focus of an electrohydraulic lithotripter (HMT LithoDiamond, Healthtronics, Kennesaw, GA). The waveform was measured at the focus by a fiber optic probe hydrophone.

Figure 1.1 (b) shows a typical shock wave generated by an electrohydraulic lithotripter. The waveform was measured in water by a fiber optic probe hydrophone [75] placed at the focus of the lithotripter. The waveform consisted of a leading triangular compression pulse with a shock front followed by a tensile phase. The peak positive pressure was 42 MPa and the peak negative pressure was -9 MPa. The rise time of the SW, defined as the time between 10 % of the peak positive pressure to 90 % of the peak positive pressure on the shock front, was measured to be 32 ns. Averkiou and Cleveland [2] modeled the shock wave produced by an electrohydraulic lithotripter using the KZK equation and predicted a rise time of less than 1 ns. The measurement of the rise time was limited by the temporal resolution of the hydrophone (due to

4

insufficient bandwidth) and therefore inaccurate. The duration of the positive phase was 1.8 μs and for the negative phase was 4.9 μs. The focal region (based on -6 dB of the peak positive pressure) was 40 mm $\times$ 9 mm.

1.1.2   Electromagnetic lithotripter

The second method of generating SWs is the electromagnetic method [83]. A strong pulsed current is transmitted through a coil, which results in rapidly changing magnetic field. A metal membrane above the coil is subjected to an opposing magnetic field thus pushing it away from the coil and generating an ultrasonic wave. Electromagnetic lithotripters (EMLs) can be subdivided into two categories. The first type employs a flat coil which generates a quasi-plane wave which is then focused by an acoustic lens. The second type of EML uses a cylindrical coil (Fig. 1.2 (a)). The resulting cylindrical wave is reflected by a paraboloidal reflector and transformed into a spherically focused wave. The initial wave produced by both types of EML is not a SW. Rather, the displacement of the plate generates a high intensity ultrasonic wave that undergoes nonlinear distortion during propagation to the focus. At the high energy settings, the nonlinear distortion results in the production of a shock in the waveform. However, at low energy settings the distortion is typically not strong enough to result in production of a SW.

Figure 1.2 (b) shows a shock wave generated by an electromagnetic lithotripter.
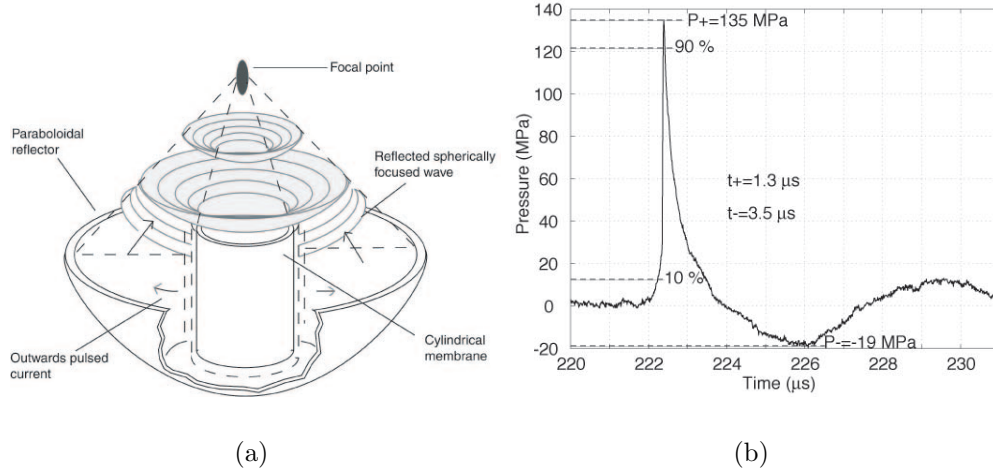
Figure 1.2: (a) Schematic for a clinical electromagnetic lithotripter. (b) A typical shock wave at the focus of an electromagnetic lithotripter (Storz Modulith SLX, Karl Storz Lithotripsy-America Inc, Atlanta, GA).

The waveform consisted of a triangular compression pulse with a shock front followed by a smooth tensile phase. The peak positive pressure was 135 MPa and the peak negative pressure was -19 MPa. The rise time of the SW was measured to be 136 ns. The duration of the positive phase was 1.3 μs and for the negative phase was 3.5 μs. The focal region (based on -6 dB of the peak positive pressure) was 28 mm $\times$ 6 mm.

1.1.3 Piezoelectric lithotripter

The third type of SW source employs piezoelectric elements [68]. In a piezoelectric lithotripter (PEL), a large number of piezoelectric elements are arranged on a spher-

6

ical bowl. The geometry of the bowl provides the focusing (Fig. 1.3 (b)). Similar to the electromagnetic source, a piezoelectric source generates a high intensity ultrasonic wave, and relies on nonlinear distortion during propagation to the focus for production of a SW. Piezoelectric lithotripters do not have wide acceptance in the US urological community due to inferior treatment efficacy [57, 6, 16] though they are employed for clinical treatment in other parts of the world, particularly in Europe.

| (a) | (b) |
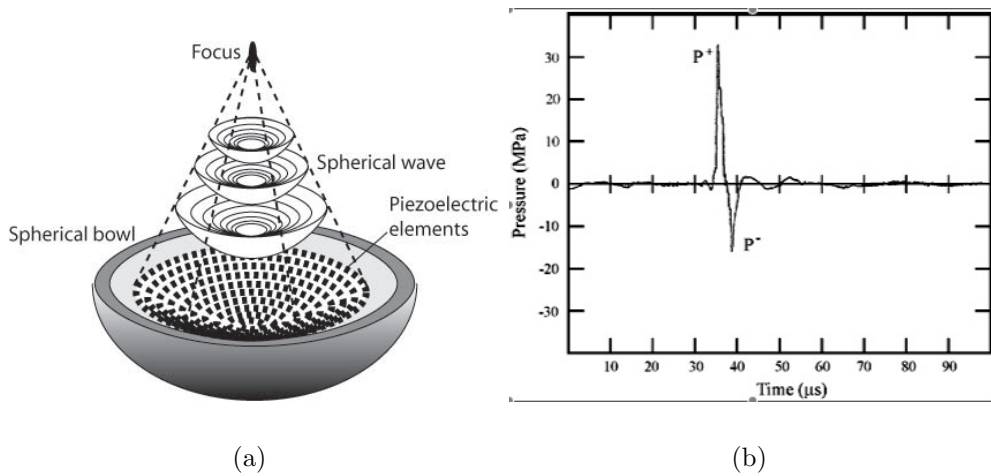
Figure 1.3: (a) Schematic for a clinical piezoelectric lithotripter. (b) A typical shock wave measured at he focus of a piezoelectric lithotripter (Wolf Piezolith 2300, Richard Wolf GmbH, Knittlingen, Germany). Waveform published by Loske et al. [61] in Physics in Medicine and Biology, 2002.

Figure 1.3 (b) shows a representative shock wave generated by an piezoelectric lithotripter [61]. The peak positive pressure was 38 MPa and the peak negative pressure was -18 MPa. The duration of the main positive phase is 2 μs. The main tensile phase is also 2 μs long. Unlike the waveforms observed from electrohydraulic and electromagnetic devives, the PEL waveform has a pronounced tail with several

cycles sustained for over 10 μs, which can be attributed to the 'ring down' of the piezoelectric elements. The dimensions of focal region PELs are comparable to that of most EMLs such as the Storz Modulith SLX (Karl Storz Lithotripsy-America Inc, Atlanta, GA) although some of the recent designs of lithotripters have a wider focal region. The significance of the size of the focal region to effective stone fragmentation will be discussed in later chapters.

1.1.4   Roadblocks in Lithotripsy

Despite more than 25 years of technological advancements and continued clinical success, there has not been a significant improvement in treatment efficacy of lithotripsy [58]. This could be attributed to the fact that although there have been a number of noteworthy changes in equipment design, none have involved a fundamental change in the acoustics of the lithotripter [18]. The shock waves produced by clinical devices currently in use are virtually the same as the first generation lithotripters and a concentrated effort to customize the shock wave pressure-time profile and/or spatial distribution of pressure is lacking.

Further hindering the improvement in treatment efficacy is the fact that continued research in the field of lithotripsy has yet to determine the mechanisms for stone fragmentation. The relative importance of different parameters of the shock wave such as peak positive and peak negative pressures and duration of the compressive

and tensile phases of the SW is still under debate. Better understanding of the interaction of SWs with stones can lead to better lithotripters.

1.2 Shock Wave and Stones

Several mechanisms for SW induced stone comminution have been hypothesized: spallation, shear, squeezing, superfocusing, fatigue, and cavitation. The relative importance for each process is yet to be determined. The first five mechanisms are associated with direct interaction between the SWs and the stone, while cavitation is related to interaction of SW with the surrounding host medium and the consequent indirect effects on the stone.

1.2.1 Spallation

Spallation is contingent on the fact that the specific acoustic impedance (product of density and sound speed) of the stone is roughly twice that of urine. The cartoon in Fig. 1.4 (a) shows an incident lithotripsy pulse entering the stone and traveling from the proximal surface of the stone to the distal surface of the stone. At the distal face of the stone, the SW encounters a stone/fluid interface resulting in reflection and inversion of the wave (Fig. 1.4 (b)). Subsequently, the inverted portion of the wave (leading positive phase of the SW) will add to the tensile stress of the still-incoming
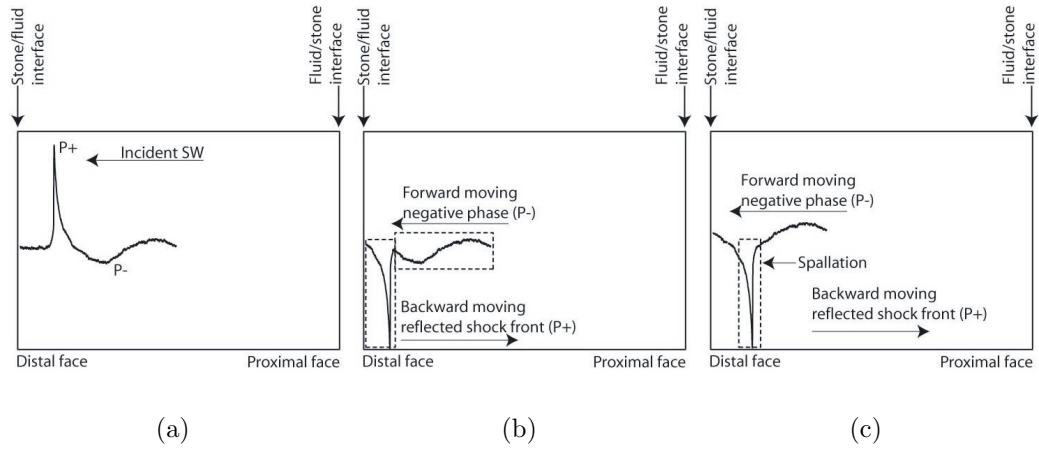
Figure 1.4: Illustration of the spallation. (a) The SW enters the stone (b) The SW reflects from the distal surface and the reflected wave is inverted (c) The reflected shock front adds to the still incoming negative phase leading to large tensile stresses resulting in fracture.

wave (trailing negative phase of the SW) resulting in a large tensile stress as shown in Fig. 1.4 (c). Most brittle solids are more susceptible to failure in tension than in compression. The large tensile stresses generated in this manner can then lead to fractures and cleaving and is a referred to as spallation [13, 70].

The development of spallation cracks can lead to fragmentation and these fragments can further undergo spallation in the same manner. Extended exposure of the stone to SWs can therefore lead to several smaller fragments. However, the spallation depends critically on the stone's dimension, particularly the distance between the proximal and distal surfaces. The critical stone dimension depends on the temporal separation between the peak positive and peak negative pressures of the SW and the speed of sound in the stone. Stones that are smaller than the critical size do not

10

allow effective superposition of the reflected shock front and the incoming negative tail. The critical dimension for a stone with sound speed of 3 mm/μs and temporal separation of 2 μs is ∼4 mm. Therefore, spallation is considered to be more dominant in the early stages of the treatment.

Efficient coupling of the incident lithotripsy SW into the stone resulting in a strong compressive wave in the stone is essential for effective spallation effects. Therefore, lithotripters with large pressure amplitude and tight focus (EMLs and PELs) are likely well-suited for generating spallation effects.

1.2.2   Shear

The incident lithotripter SW couples into the stone leading to compressional and shear waves. The generation of shear waves is contingent upon an oblique angle of incidence, therefore, shear waves typically originate from the periphery of the stone. The tensile stresses generated by the shear waves can exceed those induced by spallation. The interaction of the shear waves and the reflected compressive wave can lead to large tensile stresses which could lead to stone fragmentation [19, 87].

Furthermore, materials that consist of layers, such as kidney stones, are often weak in shear as the bonding strength of the matrix between layers can have a low ultimate shear stress [13, 87]. The stone's weakness under shear is further compounded by the

fact that that binder of kidney stones is softer than the crystalline phase resulting in large shear stresses at the binder/crystal interfaces which enhance stone fragmentation [19].

In order to generate strong shear waves, large pressure amplitudes at the periphery of the stone (region of oblique incidence) are desirable. Therefore, lithotripters with sufficiently high pressure amplitudes and a focal region wider than the stone diameter, particularly the EHLs, are particularly well-suited for generating shear wave effects.

1.2.3   Squeezing

For lithotripter acoustic fields that have a focal region wider than the stone diameter, a portion of the incident SW travels in the host medium (urine/water) and a portion enters the stone. Since the speed of sound in kidney stone is roughly twice that of water, the wave traveling in the stone moves ahead of the wave outside of the stone. The pressure wave traveling in the fluid results in a circumferential force or a hoop stress. This stress leads to dilation stresses in the proximal and distal faces of the stone as well as the central region of the stone. The stresses generated at the two ends of the stones are perpendicular to the axis of SW propagation while the stress in the stone center is parallel to SW propagation. These stresses may lead to cleavage (see Fig. 1.5) thus resulting in stone fragmentation [36].
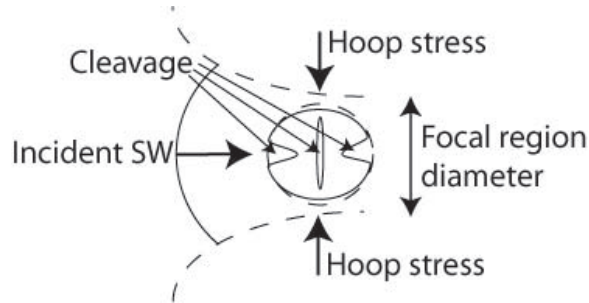
Figure 1.5: Illustration for the squeezing mechanism. Hoop stress results in cleavage parallel and perpendicular to the SW propagation.

Squeezing will be most effective when the entire stone is within the focal region of the lithotripter and has been predicted to act at pressure amplitudes ∼20 MPa. Therefore, lithotripters with moderate pressure output and a very broad focal region are well suited for enhancing the squeezing mechanism [37].

1.2.4 Superfocusing

When the incident SW pulse enters the stone, the wave traveling within the stone subsequently undergoes reflection at stone/fluid interface. Depending upon the geometry of the stone, the waves reflected from the distal region of the stone can be focused by a combination of reflection, refraction and diffraction, leading to localized amplification of stresses (stress concentrations) inside the stone. This phenomenon is referred to as super-focusing [45, 87]. The high concentration of stress can form micro-cracks which can ultimately lead to stone fragmentation.

Super-focusing can be achieved as long as SWs with large peak pressures can be effectively introduced into the stone. However, effective super-focusing depends critically on the geometry of the stone and the stone needs to be large enough for focusing to be effective, also, focusing is typically enhanced for symmetrical stone shapes, such as a sphere.

1.2.5   Fatigue

A lithotripsy treatment involves repetitive exposure of the kidney stone to as many as 2500 incident SWs. Consequently, stone fragmentation is not an instantaneous event, rather it is a gradual effect indicative of low cycle fatigue. Fatigue acts through small imperfections that are present in most materials, including kidney stones. The imperfections result in stress concentrations which result in the growth of micro-cracks after repetitive exposure to shock waves. Subsequently, these micro-cracks grow into larger cracks leading to stone fragmentation. This mechanism of stone fragmentation is referred to as fatigue [78].

Since fatigue is enhanced in the regions where high stresses coincide with material imperfections, fatigue is likely to contribute to fragmentation in a manner synergistic with other mechanisms of stone fragmentation. The role of fatigue in stone comminution is supported by the fact that internal structure of the stones affect how they break [19] and typically more than a 1000 SWs are needed to progressively fragment the

stones [78] into fragments that can be passed through the ureter.

1.2.6 Cavitation

Cavitation refers to growth and subsequent collapse of small bubbles (cavities) under the influence of the large tensile pressure subjected by the negative tail of the SW. Unlike the mechanisms described above, cavitation is a phenomenon that occurs in the surrounding fluid - urine for the case of kidney stones. When a cavitation bubble collapses near the stone boundary, it can act on the stone in several ways.

In the case where the bubble is very close to the stone, it collapses asymmetrically resulting in a micro-jet of fluid that pierces the bubble and can impact the stone wall at speeds on the order of 100 m/s [23, 28]. These micro-jets might lead to pitting and surface erosion of the stone, particularly at the proximal surface of the stone. Micro-jets can also act within fissures created by incident SWs [70]. The fissures are filled by the surrounding fluid and this fluid acts as a host for cavitation inside the stone. The microjets from the collapsing bubbles within these fissures also contribute to stone destruction. The localized pressure generated by an impacting jet can be approximated by the following equation [55].

$$P = \alpha \rho c \nu \tag{1.1}$$

where ρ is liquid density, c is the sound speed in the fluid, ν is the jet velocity, and α

represents a multiplicative constant that takes into account the transfer of momentum to the stone due to an elastic impact ($\alpha = 1$ for perfectly rigid stone).

If the bubble is far enough from the stone such that it can collapse symmetrically, it produces secondary SWs [82, 29, 55] that are comparable to the incident lithotripsy SW in magnitude and pulse duration [15, 87]. The secondary shock waves may also act on the stone via one or more stress related mechanisms described above.

Cavitation in lithotripsy is not just a single bubble phenomenon, rather it acts on the stone through a cluster of bubbles that grow and collapse in unison [66]. The presence of bubble clusters is hypothesized to enhance the destructive potential of cavitation. Cavitation depends critically on the time integral of the negative tail of the SW, therefore, a lithotripter capable of producing a SW with a large negative tail is well suited to produce cavitation effects.

1.2.7 Study of fragmentation mechanisms

Understanding the mechanisms of stone fragmentation has been one of the main thrusts behind research in the field of lithotripsy. Although it has been challenging to selectively activate a particular mechanism to distinguish the dominant ones, studies have been performed to probe various ways shock waves might interact with the kidney stone. The mechanism of stone fragmentation continue to be one of the

primary areas of research in lithotripsy and some of studies are discussed below while others involving customization of acoustic output are discussed in the next subsection.

Xi and Zhong [87] studied transient stress fields in stones using photoelastic and shadowgraph imaging techniques during shock wave lithotripsy. The leading tensile pulse of the internally reflected wave (spallation) was deemed responsible for the initiation of cracks. In addition shear waves were determined to play a critical role in fragmentation as well. The characteristic patterns of spallation were found to be significantly dependent on stone size and geometry.

Delius et al. [30] conducted a cavitation study in gall stones. Although gallstones are different from kidney stones, the physical process involving cavitation's role in stone comminution is expected to be similar. Gallstones were immersed in either a cesium chloride solution or glycerol and administered with shock waves. Glycerol solution had the same acoustic impedance as the cesium chloride solution but a much higher viscosity resulting in reduced propensity for cavitation and inhibited stone comminution. An overpressure of about 100 atm was also observed to inhibit stone fragmentation which was attributed to increase in threshold pressure for cavitation due to the overpressure.

Zhu et al. [92] administered incremental doses of shock waves to plaster of paris stones using an EHL. Stones were immersed either in degassed water or castor oil to delineate the contribution of stress related effects from cavitation effects in stone

fragmentation. Although stone fragmentation was observed under both conditions, the percentage of stone converted to debris smaller than 2 mm (a clinically passable fragment) was significantly higher for the stones immersed in degassed water. This disparity was attributed to cavitation. Contribution of cavitation alone was also examined by moving the stone transversely out of the beam focus where cavitation is still present. Though both stress and cavitation effects induced fragmentation individually, synergistic presence of both types of mechanisms was deemed necessary for effective treatment.

1.2.8 Customization of acoustic output

Coleman and Saunders [25] conducted a survey of the acoustic output of various commercial lithotripters. They used a PVDF hydrophone for acoustic pressure measurements. Coleman and Saunder's survey showed that differences in SW generation and focusing mechanisms resulted in waveforms of different magnitudes as well as different focal pressure distribution. Shock waves produced from different lithotripters were qualitatively similar.

However, if there was a correlation between a SW waveform feature and a fragmentation mechanism, then tailoring the pressure-time profile or the waveform shape could enhance that mechanism. For instance, if one device produces SWs with large peak positive pressure but small negative pressure tail, then direct stress related

mechanisms (e.g. spallation) would be dominant while the stone breakup due to cavitation would be limited as cavitation depends directly on the negative phase of the SW [56].

Chuong et al. [16] used a standard stone phantom to compare the stone damage after a SW administration with different lithotripters. They observed that with the same number of SWs, different lithotripters cause distinctly different sized damage craters, in width and depth, correlating to the different size and shape of the focal region. Since different lithotripters produce SWs that have different peak pressures and subtle differences in the waveform shapes, these studies indicate that customizing the waveform shape could alter cavitation induced stone fragmentation.

Various efforts have been made to customize waveform shapes. Riedlinger [68] proposed optimization of the pressure-time profile and the spatial pressure distribution to achieve better stone fragmentation. Four different types of piezoelectric transducers were designed and their pulse shapes were compared. Riedlinger concluded that the quasi-unipolar pulse (large $P+$ and small $P-$) produced optimal fragmentation while minimizing lesions and skin-reddening.

The method to control waveform shape suggested by Riedlinger was extended by Lewin et al [56]. The $P+/P-$ ratio of the shock wave pulses was manipulated by using three piezoelectric sources of different frequencies. Shock waves were produced from the nonlinear interaction of the pulses in the focal region. The pulse shape

was adjusted by controlling the delays to each of the source with the intention of controlling cavitation. Their results were consistent with Riedlinger's conclusions.

Bailey et al. [4][5] modified the waveform shape of an electrohydraulic lithotripter by using a pressure–release reflector to focus the SW. The pressure release reflector resulted in a focused SW with a leading tensile phase followed by a compressive phase. Their results led to the conclusion that the inverted SW was not optimal for stone fragmentation as trailing positive pressure grossly inhibited cavitation bubbles from growing.

Zhong and Zhou [91] modified the rigid reflector in an electrohydraulic lithotripter with inserts to selectively diminish the rarefactional tail in order to reduce any bio-effects related to cavitation. The inserts in the reflector produced a second positive peak coincident with the tensile phase thus reducing the negative peak pressure. The reflector inserts were demonstrated to reduce cavitation mediated stone comminution while retaining stress effects. The size of the -6 dB focal region was also reduced by the inserts thus concentrating the damage inflicted to a localized region.

Xi and Zhong [86] integrated a piezoelectric annular array (PEAA) shock wave generator with an electrohydraulic lithotripter to modify the dynamics of the cavitation field produced by the lithotripter. The PEAA SWs were triggered such that they could interact with cavitation bubbles during different stages of cavitation. *In vitro* stone fragmentation tests in conjunction with high speed camera images indi-

cated that the secondary acoustic emissions resulting from bubble collapses and stone comminution due to cavitation was significantly enhanced (an increment of 60–80 %) when the SWs from the PEAA source interacted with bubbles during cavitation collapse.

Sokolov et al. [73] developed a dual pulse lithotripter consisting of two SW sources facing each other that are confocal and triggered simultaneously to intensify and localize the cavitation field. Synchronous arival of the SWs at the focus resulted in pressure doubling and intensified cavitation while the asynchronous arrivals elsewhere resulted in weaker cavitation events outside the focus. High speed camera images showed that the cavitation field produced by the dual pulse device was 4 cm × 5 cm compared to the cavitation field from the conventional lithotripter 2 cm × 10 cm in dimension.

Zhu et al. [93] proposed the use of an acoustic diode consisting of two peripherally secured membranes having opposite surfaces held in contact under partial vaccum to truncate the negative tail. The diode constructed in this manner was hypothesized to allow the passage of the positive (compressional) phase of the SW. However, the negative (tensile) phase would result in separation of the membranes resulting in a cavity thus interfering with the propagation of the negative phase of the SW. Their hypothesis was experimentally validated using a piezoelectric SW generator [94]. Acoustic diode reduced the pulse intensity integral of the negative phase of the SW by 58 %

and reduced the collapse times for cavitation bubbles by 11 % .

To date, the primary focus of acoustic customization has been cavitation control via waveform shaping. The modification of pressure distribution has not been widely implemented in lithotripsy. One notable example where the spatial pressure distribution was altered is the wide-focus lithotripter developed by Eisenmenger [37]. It employs an electromagnetic source and generates a relatively low pressure amplitude of 20 MPa but a relatively wide focal width of 18 mm (2-4 times the diameter of a typical stone). This "wide-focus" lithotripter was reported to trigger the squeezing mechanism [36] leading to successful treatment while reducing patient discomfort and long term bio-effects. Recently, other lithotripter manufacturers are also developing devices capable of adjusting the size of the focal region, such as the Modulith SLX-F2 (Karl Storz Lithotripsy-America Inc, Atlanta, GA) , albeit with limited flexibility and only a few focal-size settings

Currently, clinical lithotripters do not posses the ability to produce a prescribed waveform shape or spatial pressure distribution for optimizing the treatment for a particular patient. A system with more flexibility over the waveform shape and spatial pressure distribution might lead to higher treatment efficacy. Furthermore, control over the acoustic characteristics might provide ability to selectively "switch on or switch off"a fragmentation mechanism.

1.2.9 Localization of kidney stone

The effectiveness of lithotripsy treatment could also be improved through better localization and targeting of the kidney stone. Clinical observations indicate that the amplitude of the displacement of a kidney associated with respiration can reach 2 cm [12]. Currently, the stone is localized using X-ray or ultrasound intermittently through the course of the treatment. Inaccurate targeting of the stone might lead to different degrees of fragmentation for different devices depending on their peak pressures and spatial pressure distribution. Since a kidney stone is in a constant state of motion induced by respiration and movement of the patient, continuous tracking of the stone is desirable.

Solutions for addressing stone motion include gating the firing of SWs to occur only when stone is at the focus [47] and synchronizing the pulse repetition frequency with the respiration cycle [48]. These methods rely on knowing the location of the stone *a priori* and cannot account for any exterior or body movement during the treatment, therefore, are not ideal solutions to stone localization problem.

A more sophisticated solution using a high power piezoelectric transducer at low power for localization was proposed by Ueberle [81]. This method allowed the use of one sound source for both localization and treatment of the stone. Localization was achieved stereophonically using two clusters of elements on the transducer and

amplitude of the echo was used to monitor stone disintegration. This method inherently requires a piezoelectric SW generator and therefore is not widely used in clinical practice (since piezoelectric lithotripters are not widely accepted).

Another method that can be applied for tracking kidney stones employs the mean normalized correlation of ultrasonic images and its real time implementation was first developed by Devevey et al. [35]. Diagnostic ultrasound is not widely used for localizing kidney stones because it does not provide a strong contrast making stone detection difficult.

In order to implement real time tracking into treatment and correct for the stone motion, electronic steering of the shock waves was proposed and demonstrated by Cathignol et al. [12]. Similar to the arrays used for imaging, inter-delay of each element was adjusted to steer the beam in a given direction. They achieved effective steering (with appropriate amplitude) in a ellipsoidal region of about 4 cm in diameter and 6 cm in length but did not implement their system in conjunction with a localization scheme.

Thomas et al. [80] developed a technique based on autofocusing property of a time reversal mirror to achieve self targeting of SWs on the stone. Although the time reversal mirror provided a robust solution for real time tracking and targeting, which can be implemented *in vivo*, it is cost prohibitive.

1.3 Shock Waves and Tissue

Although lithotripsy is a noninvasive treatment and is considered highly successful, it is not a benign procedure and can induce trauma to kidneys [52, 39, 41]. The trauma induced by SWs is especially significant for lithotripters that produce large pressure magnitudes at the focus as the focal region is an elongated cigar shape longer than the stone dimension. Furthermore, since the kidney stone is in a constant state of motion, for devices with a static focus, the tissue in the focal region suffers maximum exposure to the SWs when the stone is not at the focus.

Exposure to shock wave dosage sufficient to comminute kidney stone can cause several adverse side effects such as hematuria (blood in urine) and renal and perirenal hemorrhage which is indicative of damage concentration in soft tissue [40]. The trauma induced by lithotripsy can lead to long term complications such as new-onset hypertension [49, 54, 9] and diabetes mellitus[54]. Pediatric patients and patients with preexisting renal conditions are particularly at risk when undergoing lithotripsy as their kidneys are more prone to abuse. The SWs are hypothesized to act on tissue through shear and/or cavitation.

1.3.1 Shear

The shock waves consist of positive or compressive phase consisting of large pressure amplitude. Tissue exposed to an incident lithotripter SW can undergo significant compression. Furthermore, the SW consists of a shock front with a very short rise time (less than 100 ns) which corresponds to a length scale on the order of 100 μm. Therefore, the SW will result in large variation in stresses in small structures as it passes through the tissue leading to non-uniform strains resulting in shear forces [18]. The shear induced in the tissue due to incident SW might lead to tissue damage as tissue structures are sensitive to shear stresses [60].

The inhomogeneities in tissue can also lead to shear. Spatially variations in the sound speed of the tissue can dramatically distort the incident wavefront, which could lead to shear stresses in the tissue strong enough to induce tissue damage [18].

1.3.2 Cavitation

Lithptripsy is known to induce cavitation in tissue. The presence of *in vivo* cavitation was confirmed by physical measurements acquired in both humans and pigs (pig kidney closely resembles a human kidney [39]) using passive cavitation detection [89, 24, 69]. Cavitation is most pronounced in a fluid environment where the bubbles are not constrained and grow large enough to result in violent collapse.

These collapsing bubbles might damage tissue in three ways. First, the bubbles can collapse asymmetrically leading to micro-jets that could damage the neighboring tissue walls. Second, a symmetric collapse can generate secondary SWs that are of the same magnitude as the incident lithotripsy SW and these waves can induce shear in the tissue leading to tissue damage. Third, bubbles in blood vessels can grow resulting in rupture of the vessel walls [90]. Onset of hematoma can result in stagnant pools of blood which serves as an effective host medium for cavitation, particularly because bubble fragments are not removed by blood flow and act as nuclei for subsequent cavitation [24, 69].

1.3.3   Study of bio-effects

Despite continued research in the bio-effects of lithotripsy, the physical processes responsible for tissue damage in lithotripsy are not known, though tissue damage is primarily attributed to cavitation. Cavitation's role in inducing bio-effects was confirmed by Delius et al. [34] by exposing a piglet liver to shock waves. Upon dissection, they found tissue damage in the regions coresponding to the cavitation events. Reduction in cavitation activity due to minimal over-pressure was demonstrated to significantly reduce cell damage without significantly affecting stone comminution [33].

Several parameters have been identified as relevant to tissue damage inflicted dur-

27

ing lithotripsy. Renal injury, particularly the lesion size was determined to be correlated to the charging voltage for an electrohydraulic lithotripter [27]. The number of hematomas and the lesion size also increased with increase in the number of SWs administered to a kidney [31, 84]. Delius et al. [32] have shown that an increase in the pulse repetition rate of SWs administered to the kidney corresponds to an increase in renal damage. These trends are consistent with cavitation being responsible for much of bio-effects induced during lithotripsy. Lesion size was correlated with kidney size in that juvenile kidneys suffered larger lesions [84].

Manipulating the cavitation field resulting from a lithotripter can also reduce tissue damage. Evan et al. [38] used an electrohydraulic lithotripter consisting of a pressure release reflector to suppress cavitation by transposing the compressive and the tensile phases of the SW. Inhibiting cavitation resulted in a reduction in tissue damage inflicted by the lithotripsy SWs to a pig kidney.

Sokolov et al. [74] localized the cavitation effects using a modified electrohydraulic lithotripter with dual SW generators facing each other. This lithotripter both intensified and localized cavitation activity at the focus thus improving fragmentation and reducing cell lysis during *in vitro* experiments.

Willis et al. [85] discovered that although lesion size increases dramatically with increase in the charging voltage, vasoconstriction induced by incident SWs was determined to be unaffected by a change in charging voltage. Further, they discovered

that vasoconstriction can be induced in a matter of seconds while it can sustain for up to 10 minutes. Kidneys that were pre-treated (small dosage) at a charging voltage setting of 12 kV first and then exposed to SWs generated at 24 kV (clinical dosage) suffered a 0.3 % lesion compared to the 6 % lesion suffered by kidneys exposed to the SWs generated at 24 kV alone.

Study of bio-effects induced during lithotripsy is hindered by the fact the acoustic output of lithotripters varies over different modes of generating and focusing SWs onto the kidney stones. These differences in acoustic parameters translate into differences in degree of renal damage. Therefore, a system capable of inducing several different acoustic outputs is desirable. For a more detailed overview of bio-effects induced by lithotripsy SWs, readers may refer to reference [41].

1.4   Motivation and Goals

In summary, the work done by researchers up to date indicates that several possible mechanisms such as spallation, shear waves, squeezing, super-focusing, fatigue, and cavitation can be responsible for stone fragmentation and tissue damage. Dependent upon the specific acoustic output of a lithotripter, different mechanisms might be dominant. A better understanding of how the SWs interact with the kidney stone and tissue could lead to improvements in treatment efficacy while reducing harmful

bio-effects.

Knowledge of mechanisms can be best implemented by designing a device capable of customizing the pressure-time profile as well as the focal pressure distribution, so that the acoustic output may be optimized for each specific case. Incorporating such a design with real time target tracking could further improve the success of the treatment. Current clinical lithotripters are rigid in nature in that they do not typically posses the ability to vary the acoustic output without making significant changes to the hardware. This study presents a design for a piezoelectric lithotripter that can potentially achieve these goals. The work here will focus on stone fragmentation only, the study of bio-effects is beyond the scope of this work.

The primary goal of this research was two fold, to provide a formulation that predicts the inter-element delay for each transducer element in order to obtain a desired waveform shape and focal pressure distribution, and to implement the formulation in an experimental system to evaluate the roles of different mechanisms in SWL. The correlation between different waveform shapes and stone breakage could be investigated using this device by administering different SWs to standard test stones. The proposed design is based on the piezoelectric device presented by Cathignol et al. [12] with multiple elements arranged in a spherical bowl. An inverse filter formulation based on spatio-temporal inverse filter developed by Tanter et al. [79] was implemented to determine the inter-element delays.

Chapter 2

Materials and Methods

The instrumentation employed for developing the lithotripter system used in the current study and the pertinent experimental methods will be presented in this chapter. The chapter addresses three topics: the development of the shock wave source, the instrumentation and methods for acoustic and cavitation measurements, and the methods and protocols for stone fragmentation study.

2.1 Piezoelectric Lithotripter Array

In this work, a piezoelectric array was employed to generate SWs. The main advantage of using a piezoelectric array is that it provides much greater control over the acoustic field. Given arbitrary waveform generators, the individual elements can

be driven with arbitrary waveforms and allow waveform shaping and beam steering through electronic control. Further, the elements can also be used as receivers and have the potential to be employed for imaging or target tracking during SW treatment. Finally, piezoelectric sources have a stable acoustic output over a very large number of SWs. Arranging a significant number of piezoelectric elements in a bowl of sufficient curvature can produce desirable focusing leading to large cumulative peak pressure at the focus due to the focusing gain.
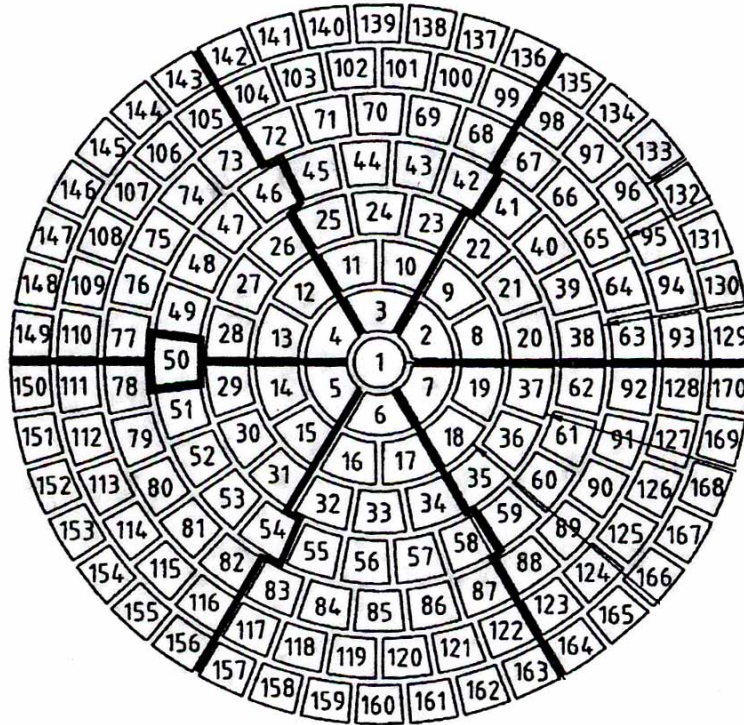
Figure 2.1: A diagram of transducer elements in the spherical bowl and their numerical identification.

The piezoelectric system in this study composed of a 170 element focused array

(Imasonic S. A., Besancon, France) with a radius of curvature of 150 mm, aperture diameter of 154 mm, and a center frequency of 600 kHz (Q=2) constructed in a circular polymer housing. The transducer was constructed from a "1-3" piezo-composite material which consists of thin ceramic rods encapsulated within a polymer matrix. The 1-3 structure of the composite reduces radial vibration modes in the elements resulting in improved beam pattern and pulse shape and limits the cross coupling between neighbor elements (further details on cross coupling in Chapter 3). The layout of the elements (identified as e_1 through e_{170}) across the face of the transducer is shown in Fig. 2.1. The array consisted of a central element of circular cross-section and seven axisymmetric rings with elements of trapezoidal cross-section. Each element had a surface area of 88 mm^2. The maximum permissible driving voltage was 6 kV. The average electrical impedance of an element when the array was acoustically loaded with 1.5 MR at the center frequency was $Z = 313\Omega - j504\Omega$.

2.2   Electronic Driving System

The piezoelectric array described in the previous section was driven by a 170-channel high voltage pulser (Gammell Applied Technologies, LLC, Exmore, VA). Each channel of the pulser employed a 220 nF capacitor which can be charged to 1200 V. A high voltage insulated gate bipolar transistor (IGBT) was used to discharge the capacitor

through the transducer element. Each channel was independently controlled by a TTL-level pulse generated by a pulse-pattern generator (81104A, Agilent, Palo Alto, CA). Both the duration and the timing of the TTL pulse for each channel could be adjusted independently with a 100 ns resolution. A supply voltage of 1200 V was used at all times unless stated otherwise. For further details on this pulser circuit, readers may refer to reference [42], the version employed in this work is the non-doubling circuit.

A typical voltage output from the pulser (wired to a transducer element) when triggered using a 0.5 μs TTL pulse is shown in Fig. 2.2. The rise time determined as the duration from 10 % magnitude to 90 % magnitude was 22 ns. The pulse duration of 0.5 μs was determined to be optimal in producing the maximum acoustic pressures from a driving signal that was fixed in shape and amplitude.

2.3   Test Tank

The transducer was mounted into the wall of a cast-acryllic test tank (shown in Fig. 2.3) of dimensions 0.5 m $\times$ 0.9 m $\times$ 0.5 m. The tank was fitted with a filtration and degassing system. A 5 μm sub-particle filter (Cole–Parmer, Vernon Hills, IL) along with a magnetic non-submersible pump (Tecumseh Products Company, Oklahoma City, OK) was used for filtering the water. A pinhead degassing system [51] was used
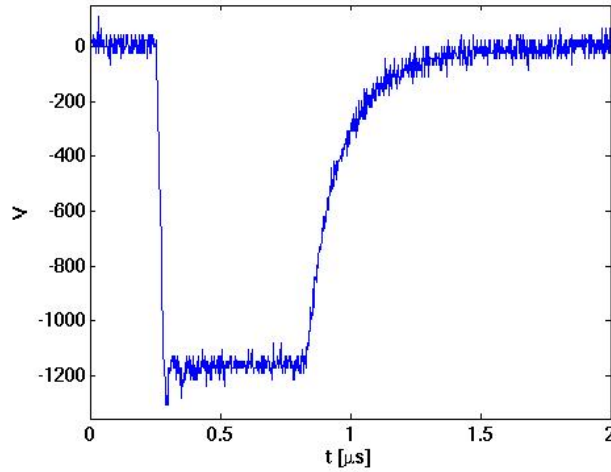
Figure 2.2: A typical high voltage pulse produced by the pulser (when wired to the transducer element) given a charging voltage of 1200 V.

for degassing the water. The dissolved gas content of the water in the test tank was maintained roughly at 50 %. Positioning in the test tank was accomplished using a computer controlled three axis positioner (Velmex, Inc., Bloomfield, NY) with a spatial resolution of 5 μm.

2.4 Acoustic Measurements

A polyvinylidene fluoride (PVDF) membrane hydrophone (0200, Precision Acoustics, Dorchester, England) with a 0.2 mm diameter active area and a bandwidth of 30 MHz was used for all acoustic measurements produced by driving only one element at a time. The hydrophone, referred to as the PA hydrophone hereon, used in conjunction
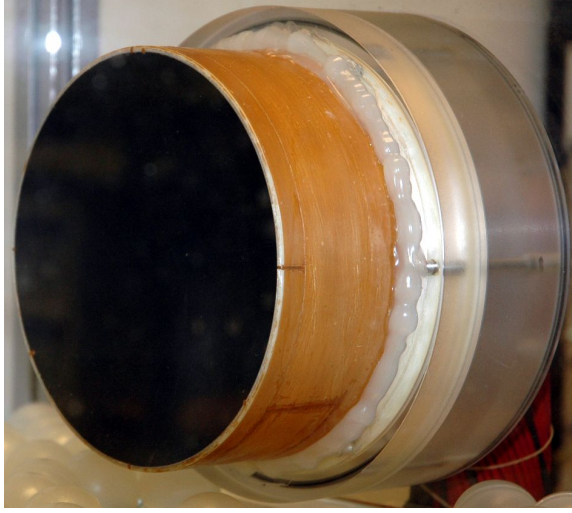
Figure 2.3: Picture of the piezoelectric array mounted in the test tank.

with a 20 dB preamplifier (50 Ω termination) had a sensitivity of 33.3 MPa/V (flat over a frequency range of 0.1−20 MHz). The PA hydrophone signal was passed through a tunable high pass filter (Model 3940, Kron-hite, Avon, MA) with a cut-off frequency of 10 kHz and gain of 20 dB with a nominal frequency range of 0-10 MHz to further improve the signal to noise ratio. The input impedance of the high pass filter was 1 MΩ and output impedance was 50 Ω.

When all the elements of the array were driven simultaneously, the resulting acoustic pressures exceeded maximum permissible incident pressure for the PA hydrophone, therefore, acoustic measurements were performed using a fiber optic probe hydrophone (FOPH) [75] or a PVDF membrane hydrophone developed especially for measuring large amplitude pressures at the University of Washington [63]. The bandwidth and a receiving aperture size of the FOPH were 0.1−30 MHz and 100 μm

respectively. The PVDF hydrophone, referred to as UW hydrophone hereon, had a bandwidth of $0.1-20$ MHz and a receiving aperture size of 0.5 mm.

Individual waveforms were recorded on a digital oscilloscope (Waverunner 6000A, Lecroy, Chestnut Ridge, NY) with a 8 bit resolution and input impedance of 50 Ω and transferred to a computer and post-processed using Matlab (Mathworks, Natick, MA).

A set of ten waveforms obtained from a single element (e_1) driven at 1.2 kV pulse repetition frequency (PRF) of 1 Hz is shown in Fig. 2.4. The received signal was highly reproducible with a temporal jitter of less than 30 ns and is characteristic of waveforms produced by all of the elements. The maximum jitter between any two elements was determined to be within 50 ns. The peak positive pressure produced from a single element was observed to be around 0.2 MPa at the focus of the piezoelectric array.

The piezoelectric lithotripter array was characterized while all elements were driven synchronously. Figure 2.5 shows the waveform produced by driving all the elements of the array in phase with a 1.2 kV pulse. The waveform shown was obtained by first measuring ten waveforms with the PVDF hydrophone, aligning their main shock fronts and then averaging the waveforms. The alignment was performed by matching the arrival time corresponding to 50 % of P_{1+} and facilitates coherent averaging of shock waves. Incoherent averaging might lead to 'smearing'of the shock front errors
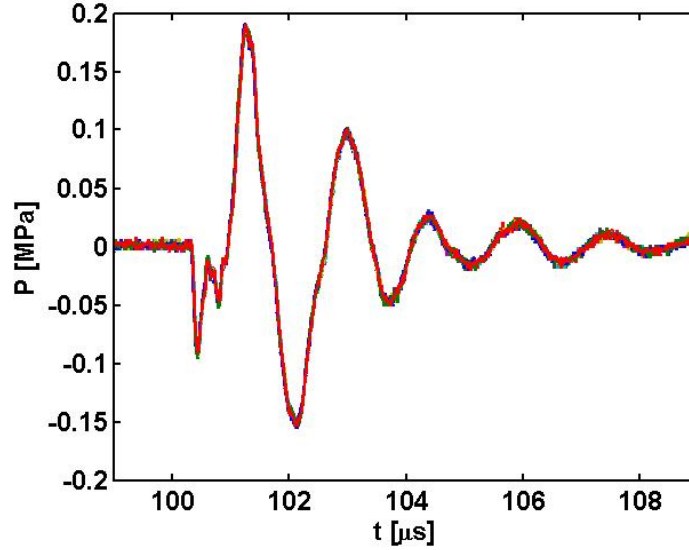
Figure 2.4: Overlay of ten consecutive waveforms obtained from e_1 when driven with 1.2 kV pulse lasting 0.5 μs at PRF of 1 Hz.

in measurements of peak positive pressure. Unlike the more typical lithotripsy waveforms generated by the electrohydraulic and electromagnetic devices, the waveform has four distinct features. The waveform consists of a negative precursor (P_1-) 0.5 μs long and a negative pressure of -10 MPa followed by the main shock front with a positive peak (P_1+) of 68 MPa. The rise-time determined by the hydrophone (bandwidth limited) was 30 ns and the duration of the positive phase (t_+) was 0.4 μs. The negative phase following the positive peak was 1 μs long with peak negative (P_2-) pressure of -15 MPa. The second shock front has a peak positive pressure (P_2+) of 36 MPa. The entire shock wave pulse had a duration (t) of 5 μs. The implications of this waveform shape on stone fragmentation will be discussed in detail in following

38
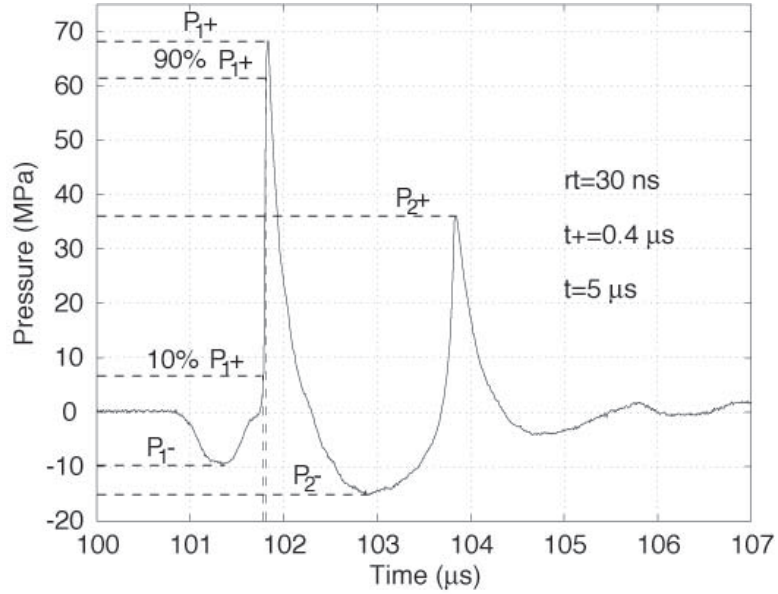
Figure 2.5: A characteristic waveform produced by the piezoelectric lithotripter array when all elements were driven synchronously. The displayed waveform is an average of ten waveforms recorded consecutively at PRF of 1 Hz.

chapters.

Figure 2.6 shows the mean P_{1+} and P_{2-} as a function of charging voltage. The error bars represent the standard deviation of 10 samples for each charging voltage. Measurements indicated a monotonic increase in pressure with increase in the driving voltage. The spatial pressure distribution of the acoustic field produced by the array source was also characterized while driving the elements in phase. Since the the maximum operational voltage for the IGBTs used in the high voltage drivers was 1.2 kV, pressure maps were acquired while driving the piezoelectric array lithotripter at 1 kV to prevent overload due to any voltage fluctuations. Pressure measurements were acquired (with the FOPH) along the X, Y, and Z (focal) axes and the focus
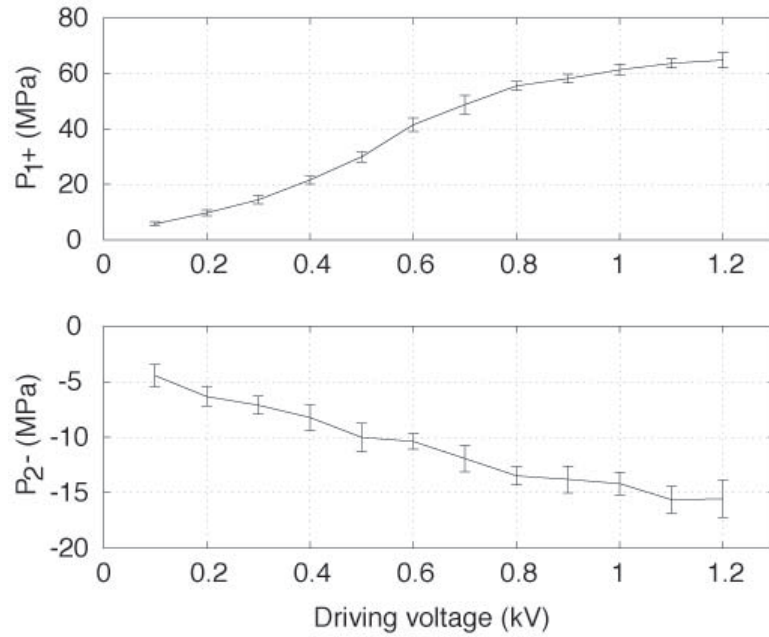
Figure 2.6: Peak positive pressure (P_{1+}) and peak negative pressure (P_{2-}) as a function of driving voltage. Peak pressures increased monotonically with increase in driving voltage.

| (a) | (b) | (c) |
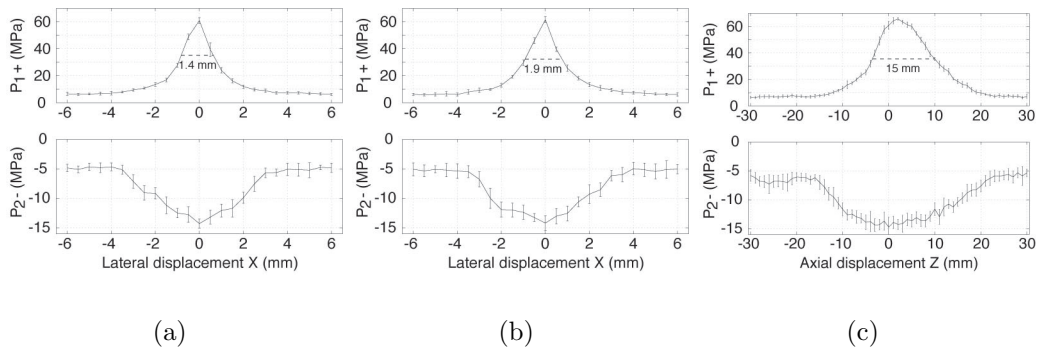
Figure 2.7: Peak pressure measurements along the X, Y, and Z (focal) axes. The -6 dB focal region based on the primary peak positive pressure was 15 mm long and between 1.4 and 1.9 mm wide.

was at $(0, 0, 0)$ and the central element of the array (e−1) was at (0,0,150 mm). The X-axis was in the horizontal plane and the Y-axis was in the vertical plane. Figure 2.7 shows the acoustic field maps along all three axes. The top curve in each figure shows P_{1+} and the lower curve P_{2-} with respect to displacement from the focus. The International Electrotechnical Commission (IEC) standards [46] for acoustic measurements in lithotripsy dictates that the focal width be determined using -6 dB of the peak positive pressure (P_{1+}). The focal region was thus determined to be 1.4 mm × 1.9 mm × 15 mm.

2.5   Waveform Shaping

Waveform shaping was motivated by the need to control cavitation. Cavitation depends on the negative phases of the waveform and manipulating these portions of the waveform can lead to cavitation control. As stated in Section 2.2, the electronic driving system for the piezoelectric lithotripter array allows control over time delay imposed on each element with a resolution of 100 ns. The waveform shape was manipulated in ad hoc manner by manually adjusting the delays for each element.

Figure 2.8 illustrates the waveform shape that can be achieved by firing 130 elements simultaneously and firing the remaining 40 with some delay. The waveform shape was modified significantly by increasing the delay with increments of 100 ns.

(a) no delay   (b) 100 ns   (c) 200 ns

(d) 300 ns   (e) 400 ns   (f) 500 ns
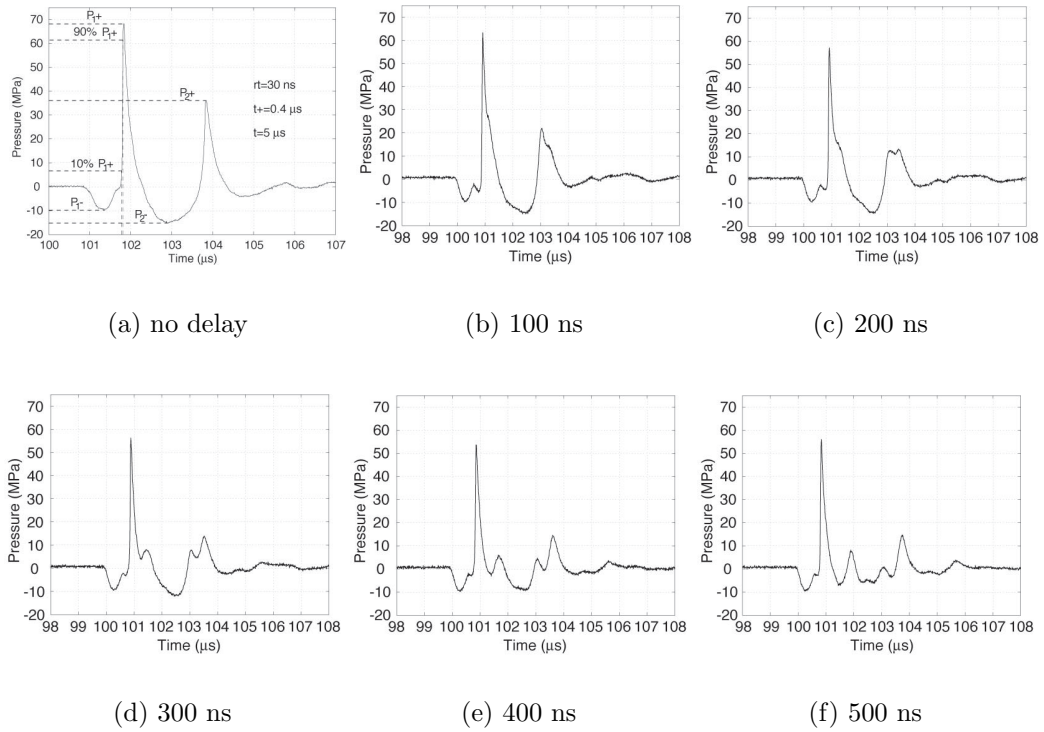
Figure 2.8: Waveforms obtained by firing 130 elements simultaneously and the remaining elements with delays from 0 to 500 ns.

A delay of 500 ns (Fig. 2.8(f)) resulted in a decrease in P_2- from -16 MPa to -7 MPa, which would inhibit cavitation. Different delay configurations were chosen for different desired waveforms using a trial and error approach similar to one shown above.

2.6 Gilmore model

Shock wave measurements were used to predict the response of a single bubble to the incident acoustic field using the Gilmore formulation [43][17]. The Gilmore model is an appropriate choice as it accounts for the compressibility of the fluid which is important for large driving pressures. The Gilmore equation was integrated using the Runga Kutta method ("ODE45") provided in Matlab (Mathworks, Natick, MA). The underlying assumptions for the Gilmore model are given as follows:

- The SW was assumed to interact with a single air bubble.

- The bubble is in the free field, that is, it is not near any boundaries or other bubbles

- The bubble remained spherical at all times.

- The gas within the bubble was assumed to be an ideal gas.

- The bubble radius was small compared with the acoustic wavelength.

- Body forces, such as gravity, were negligible.

- No energy was transferred in or out of the bubble in form of heat.

- Gas diffusion was ignored.

The Gilmore equation is written as:

$$R\ddot{R}\left(1 - \frac{\dot{R}}{C}\right) + \frac{3}{2}\dot{R}^2\left(1 - \frac{\dot{R}}{3C}\right) = H\left(1 + \frac{\dot{R}}{C}\right) + \frac{R\dot{H}}{C}\left(1 - \frac{\dot{R}}{C}\right). \qquad (2.1)$$

R is the bubble radius and the first and second derivatives of R are denoted as $\dot{R}$ and $\ddot{R}$ respectively. H is enthalpy and C is time varying sound speed in the medium. The pressure term is incorporated in the Gilmore equation (Eq. 2.1) as

$$H = \int_{P_\infty}^{P(R)} \frac{dP}{\rho}. \qquad (2.2)$$

P_∞ consists of incident acoustic pressure and static ambient pressure. $P(R)$ is the pressure at the bubble wall and is given as a balance between the gas pressure (P_g) inside the bubble and pressure terms associated with surface tension and viscosity of the medium (Eq. 2.3). σ and μ are surface tension and viscosity respectively.

$$P(R) = P_g - \frac{2\sigma}{R} - \frac{4\mu}{R}U. \qquad (2.3)$$

The relationship between pressure and density is given by the equation of state:

$$\frac{P}{P_0} = A\left(\frac{\rho}{\rho_0}\right)^m - B, \qquad (2.4)$$

where $A = \frac{c_0{}^2\rho}{P_0 m}$ and $B = A - 1$. P and ρ are time varying pressure and density respectively. P_0 and ρ_0 are static ambient pressure and density respectively. Sound speed C can be written in terms enthalpy and ambient sound speed C_0 as:

$$C = \sqrt{C_0{}^2 + (m-1)H},\tag{2.5}$$

where m is constant in equation of state (Eq. 2.4) and $m = 7$ for water.

Gilmore model is limited to the single bubble assumption only and does not accurately predict or quantify the cavitation damage inflicted upon the stone. Furthermore, many of the underlying assumptions such as sphericity of the bubble, absence of boundaries, and absence of gas diffusion are violated in the experimental situation. Therefore, the Gilmore model is used in this work merely as a tool to predict the response of a single bubble to an incident shock wave for the purposes of comparing and contrasting the cavitation induced by different waveforms to first order. In reality, cavitation on stones administered with shock waves is a bubble-cluster effect where the bubble clouds grow and collapse on stone surface collectively in response to the incident shock wave. The response of bubbles in bubble cluster is analogous to set of coupled oscillators. The length and time scales of the bubble cloud response are an order of magnitude higher than those for the single bubble. Therefore, it is reasonable to assume that the damage inflicted by a bubble cluster on the stone surface will be

significantly higher in comparison to a single bubble.

The Gilmore model predicts that a bubble under the influence of an incident SW will collapse violently producing a strong secondary acoustic emission. The numerical predictions of bubble's response to the incident shock wave and their interpretations will be presented in Chapter 4. The acoustic signature associated with the collapse of the bubble is an ideal signal for detecting and quantifying cavitation and can be observed effectively using a passive cavitation detection [21].

2.7   Cavitation Measurements

Two experimental methods were used to observe and quantify cavitation: one for single bubble dynamics in the free field, other for bubble cluster activity on the proximal surface of the stone. The free field cavitation was experimentally characterized using a combination of a dual passive cavitation detector (PCD) and a high speed camera. Another higher frequency single PCD was employed to measure cavitation on the stone surface. Cavitation mediated shielding effect in front of the stone was monitored using a diagnostic ultrasound system.

2.7.1 Dual Passive cavitation detector

The Dual PCD employed in this study was based on the detector developed by Cleveland et al. [20] and consisted of two focused 1 MHz transducers (A392S, Panametrics Inc., Waltham, MA) with $Q = 2$, aligned orthogonally and confocally with the lithotripter focus as shown in Fig. 2.9. The transducers had a focal length of 63.5 mm and aperture of 38.1 mm. Two transducers were used for improved localization of the origin of the cavitation induced acoustic emissions. The sensitive region of the DPCD was determined to be 5 mm in diameter dictated by the intersection of the -6 dB focal regions of the two transducers.

Traces from both the PCDs were recorded using the oscilloscope and stored on a computer. Each PCD trace consisted of two signatures, one corresponding to the arrival of SWs, other corresponding to the inertial collapse of bubbles. Signals originating from the mutual focus of the two transducers were identified by means of coincidence detection, that is, an event that resulted in signatures with the same arrival times for both the PCDs. Based on the 5 mm diameter focal region of the dual PCDs, a tolerance of 3.4 μs was allowed for the arrival times. For each cavitation event at the mutual focus of the PCDs, the time difference between the two signatures referred to as the characteristic time t_c was determined and used as a parameter to quantify the strength or violence of the cavitation collapse. The violence of cavita-
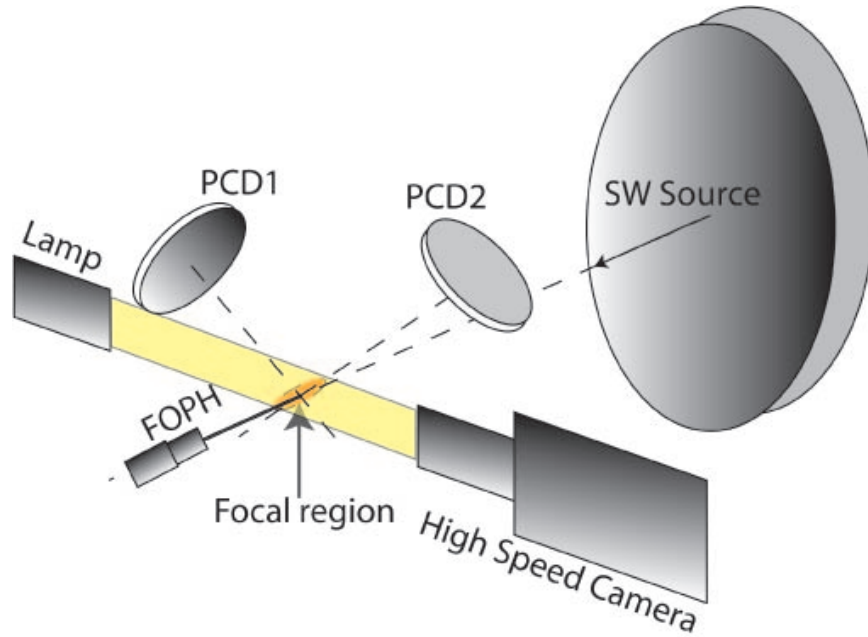
Figure 2.9: Schematic for free field cavitation characterization.

tion collapse refers to a cavitating bubble's potential to inflict damage to the stone. Longer t_c implies longer growth phase of the cavitating bubble, which in turn implies larger expansion ratio (R_{max}/R_0) of the bubble. The strength of the bubble collapse is proportional to the expansion ratio. The magnitude of the signal corresponding to the acoustic emission from the inertial collapse (P_{rad}) was also used to quantify the violence of the collapse.

2.7.2 High speed camera

A high speed camera (Imacon 200, DRS Hadland, New Jersey, NJ) was also used to observe cavitation induced by the lithotripter. The camera was oriented normal to

the transducer's focal axis and the focal region was backlit by a diffused white light source (Fig. 2.9). A spatial resolution of 2 μm/pixel was achieved by attaching a long distance microscope (Model K2, Infinity-USA, Boulder, CO) for free field cavitation characterization. The camera was operated with an exposure time of 100 ns and a frame rate of 12 μs.

The images were processed Using Matlab's image processing toolbox. A fifth order Wiener filter was implemented to reduce the pixilation noise. The image was then converted into an binary image using a threshold level of 0.1. The pixels on the image that visibly did not belong to the bubble of interest were logically suppressed. The image processing steps are illustrated in Fig. 2.10. The image processing technique is able to produce an image that retains all the key bubble features while eliminating noise from rest of the image. The frame shown in Fig. 2.10 corresponds to R_{max} and cavitating bubbles are expected to be spherical in this regime. The degradation in the sphericity of the bubble might be an indication that the bubble is influenced by the presence of another bubble in its vicinity or a second bubble might be directly behind the visible bubble and collapsing with a jet. However, 2-D projection of the bubble captured by the bubble is not sufficient to determine the reason for the non-spherical bubble.

The processed images were used to determine the area of the bubbles in each frame by counting the number of pixels that constitute the bubble. The bubble radius in
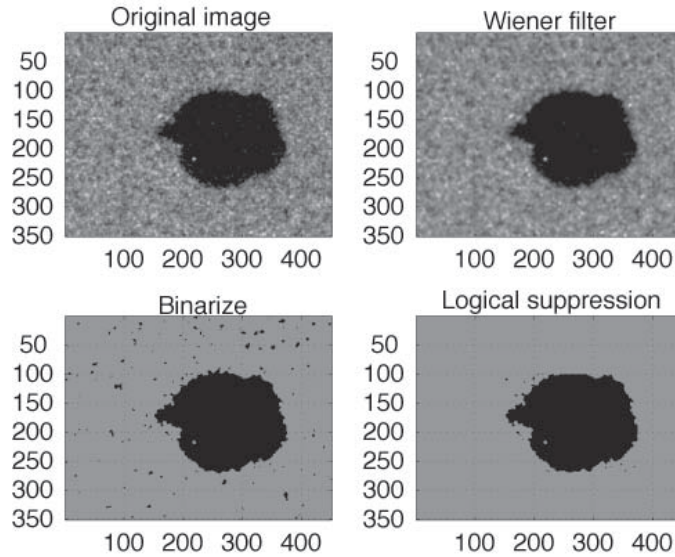
Figure 2.10: Four steps of image processing performed prior to bubble area estimation.

each frame was determined by fitting the area of the bubble to a circle. Radius-time profiles were obtained from the high speed camera images which provide the characteristic time and the maximum bubble radius. Agreement in the characteristic time obtained by the high speed camera and that obtained using the dual PCD was an indication that the bubble was in the focal region of the dual PCD which in turn indicated that the bubble was in the focal region of the piezoelectric lithotripter array.

2.8   Single PCD

Cavitation on the proximal surface of a phantom stone (details about the phantom stone presented in the following section) was measured using a single PCD. A 3.5 MHz
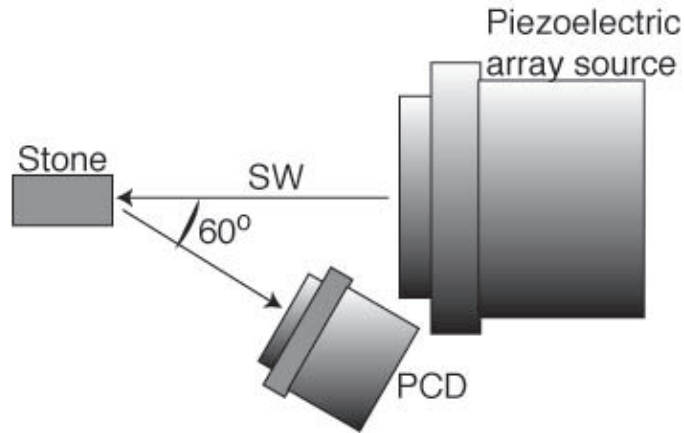
Figure 2.11: The schematic for characterization of cavitation on the proximal surface of the stone.

transducer with a focal length of 50.8 mm, an aperture of 25.4 mm, and a $Q = 2$ was chosen to obtain a narrow sensitive PCD region. The -6 dB beam diameter of the PCD was determined to be 1.3 mm. The stone's proximal surface was aligned at the lithotripter focus. The PCD focus was aligned with the stone by maximizing the scattered lithotripter pulse from the stone. The PCD was positioned such that its focal axis was at an angle of approximately 60° relative to the focal axis of the piezoelectric lithotripter array. The schematic of the PCD-stone arrangement is shown in Fig. 2.11.

The violence or strength of cavitation collapses on the proximal surface was described in terms of characteristic time (t_C) and the magnitude of the inertial collapse signal (P_{rad}). Cavitation on the stone surface was characterized for three waveforms, waveform produced by driving all elements in phase, waveform designed to reduce

P_{1-}, and the waveform designed to reduce P_{2-}. In order to probe cavitation bubble clusters characteristic of lithotripsy 30 shock waves were fired and the PCD measurements were acquired for the cavitation induced by the last 20 shock waves. In order to investigate the influence of rate, the shock waves were administered at either 1 Hz or 0.5 Hz. The t_c and P_{rad} were then averaged for each waveform shape and pulse repetition frequency.

2.9 Stone Fragmentation Studies

Stone fragmentation studies were performed using phantom stones made from Ultracal-30 gypsum cement. Ultracal-30 gypsum cement was mixed with water in equal parts. The mixture was then cast in plastic multi-well plates. The plates with stones were immersed in chloroform to free the stones which were then stored in water. The Ultracal-30 stones have acoustical properties similar to natural stones [11][64]. The stone had a density of 1700 kg/m^3. The longitudinal and shear speeds of sound in stone were 2590 $\pm$ 55 m/s and 1270 $\pm$ 76 m/s respectively. The stones were approximately rectangular in shape with a cross-section 3 mm $\times$ 3 mm and 5 mm in length. Figure 2.12 shows an image of an artificial stone.

Stones were degassed for 90 minutes in a petri-dish filled with distilled water. Stones were then clamped in a holder constructed from a plastic pipette as shown in
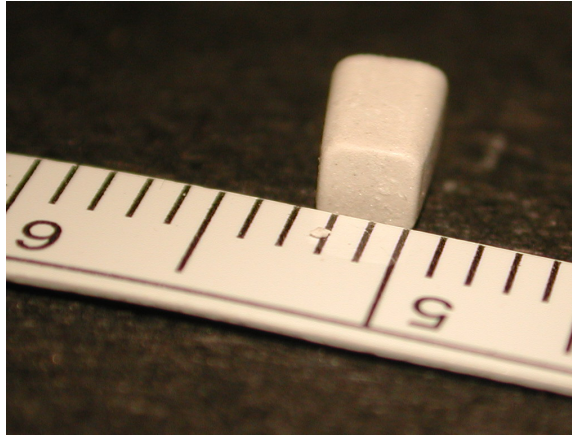
Figure 2.12: Image of an artificial stone.

Fig. 2.13 (a). The proximal surface of the stone was placed at the focus (0,0,0) of the transducer array such that minimal surface of the stone was in contact with the holder. Alignment of the stone was achieved by using elements e_2-e_{170} to transmit a weak interrogatory pulses (25 V) and using the central element (e_1) as a receiver. The stone was scanned along the lateral axes and the location producing a maximum return signal was designated as the focus. The alignment along the focal axis was achieved based on the travel time of the pulse-echo. Ten stone samples were treated for each type of acoustic pressure distribution or waveform shape.

Stone fragmentation was assessed either by a measurement of mass or a measurement of tensile strength. Since the stones did not exhibit a characteristic spallation fracture, the mass measurements were in fact a measure for cavitation induced stone erosion. Mass of the treated stones were measured using a digital scale and compared with the mass of the untreated stone (46 mg). Post-treatment mass measurements

(a) Stone holder   (b) Tensile test
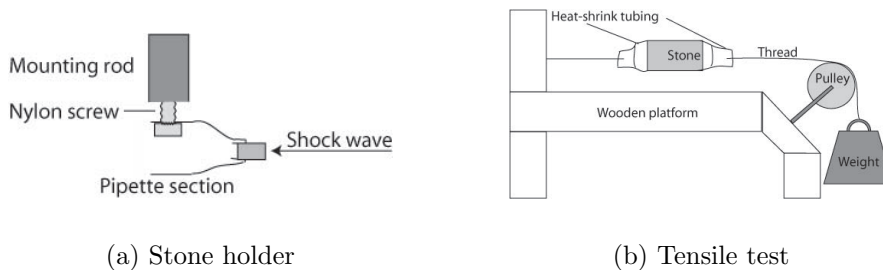
Figure 2.13: Schematics for stone fragmentation studies.

were acquired for stones treated with different acoustic fields and waveform shapes at either PRF of 1 Hz or 0.5 Hz.

Since the stones did not exhibit any visible signs of stress induced fragmentation, tensile strength measurements were performed on the treated stones in order to quantify effect of stress on the stones. The stones were first placed in the holder shown in Fig. 2.13 (a) for shock wave treatment. The stones were then removed and air-dried. The dry stones were then placed in the tensile strength measurement apparatus as shown in Fig. 2.13 (b). Stones were held in place using two sections of 2 cm long heat shrink tubing. The tubing was placed on either side of the stone so that it covered about 1 mm of the stone on either side. The tubing was then exposed to heat causing it to shrink creating a tight hold on the stone. To facilitate a better hold by the heat shrink tubing, less cavitation induced erosion was desired, therefore, the stones were under-treated (200 shock waves). The two ends of the tubing were then attached to fishing line and subjected to tension by incrementally increasing the mass hanging

from the pulley. Minimum tension required to break the stones apart was determined for stones treated using each of the acoustic fields and waveform shape (10 stone samples each) and compared to that for the untreated stones. The reproducibility of this approach to quantify stress induced damage was verified by comparing 3 sets of 10 untreated stones, each resulting in an average tensile strength of $\sim$12.5 N.

Chapter 3

Theory of Acoustic Field

Customization

The method utilized in this study to customize the acoustic output of the piezoelectric lithotripter array is loosely based on the approach by Tanter et al. [79]. There it was demonstrated that an arbitrary pressure-time profile and spatial pressure distribution can be achieved by implementing a spatio-temporal inverse filter. Though they presented a viable solution to the inverse problem, the implementation of spatio-temporal inverse filter is instrumentation intensive as it requires the ability to excite each element with an arbitrary signal.

The hardware available for this study consisted of 170 pulse discharge circuits where the only control parameters were the time that each element could be fired.

The challenge was to find the appropriate timing for each element that resulted in a field that approximated the desired result. We applied an inverse problem approach where the acoustic field was modeled using angular spectrum theory. A cost-function between the predicted and desired fields was defined and an optimization routine was employed to minimize the cost function. A satisfactory approximation to the desired waveform shape and spatial pressure distribution was achieved.

3.1   Spatio-Temporal Inverse Filter

We first present the spatio-temporal inverse filter (STIF) approach in this section before adapting it to the problem at hand. The wave propagation model implemented in this work will be presented in the next section.

Consider a linear array with L elements as shown in Fig. 3.1. The goal of the inversion is to determine the required excitation on each element $e_l(t)$, where $l = 1..L$ is the element number, such that a prescribed acoustic field is generated. The prescribed field is defined in terms of M control points where the pressure at each control point $p_m(t)$ is given. The solution of the inverse problem requires the knowledge of the impulse response $h_{ml}(t)$ between element l and control point m, where $h_{ml}(t)$ accounts for the electro-acoustic transfer function and the wave propagation from the lth element to the mth control point.
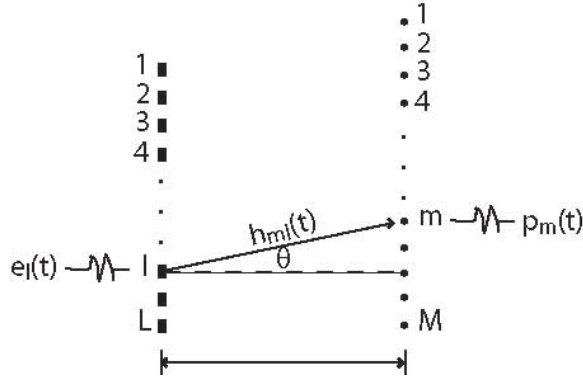
Figure 3.1: Schematic diagram for Tanter's formulation of spatio-temporal inverse filter.

For the input signals $e_l(t)$, the signal received at control point m can be written as

$$p_m(t) = \sum_{l=1}^{L} h_{ml}(t) * e_l(t), \tag{3.1}$$

where $*$ indicates convolution in time. The received signal can be represented in the frequency domain as

$$P_m(\omega) = \sum_{l=1}^{L} H_{ml}(\omega) E_l(\omega). \tag{3.2}$$

The optimal set of L broadband input signals $e(t)$ required to satisfy the control conditions can be expressed as

$$e_l(t) = \mathcal{F}^{-1} \sum_{m=1}^{M} H_{ml}^{-1}(\omega) P_m(\omega), \tag{3.3}$$

where $\mathcal{F}^{-1}$ denotes the inverse Fourier transform. The inversion shown in Eq. 3.3 is only possible if $H(\omega)$ is a square matrix. In an event where $M \neq L$, regularization

of the propagation operator matrix is necessary prior to the inversion. Tanter et al. employed singular value decomposition for this purpose. Typically, M is chosen to be greater than L resulting in an over-determined problem.

3.2   Wave Propagation Model

For an ideal STIF, the excitation signal would be arbitrary both in shape and amplitude. In practice, the bandwidth of the transmit elements restricts the waveforms that can be created. Further in the piezoelectric lithotripter array employed here, the driving signal was restricted to an impulse in which case the elements responded with their impulse response. Therefore, the timing of the generation of the pulse was the only control variable.

As described previously, the piezoelectric source consists of 170 elements arranged on a spherical bowl. The curvature of an individual element is small. Therefore individual elements might be expected to behave like ideal planar baffled pistons. However, measurements of the acoustic pressure along the focal axis (when the central element was excited with a 10 cycle tone burst at the center frequency (0.58 MHz) of the transducer) indicated that the overall curvature of the region surrounding each element resulted in complex diffraction effects and focusing as shown in Fig. 3.2. The measurement acquired along the focal axis (in the range well beyond the Rayleigh
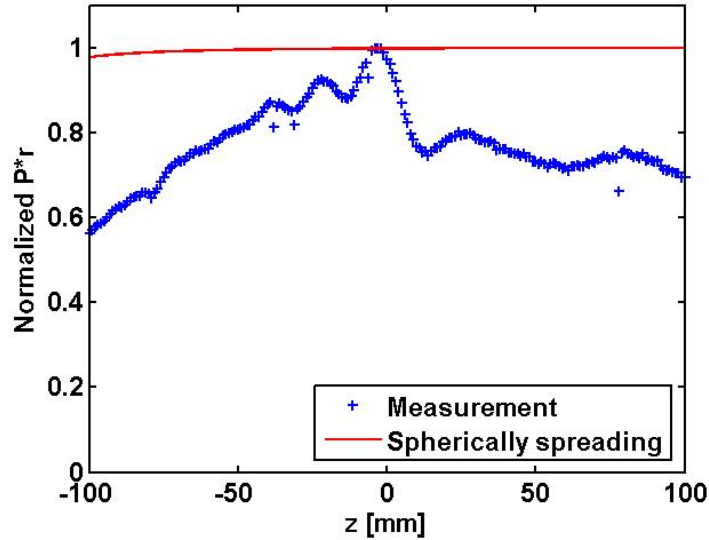
Figure 3.2: Normalized amplitude times the distance from the transducer element with respect to the focal axis, z. The measurements do not exhibit a spherically spreading pressure field as predicted by the analytical expression for radiation from a planar baffled piston.

distance of 34 mm) does not exhibit a spherically spreading pressure field as predicted by the analytical expression for radiation for a planar baffled piston. Hence, individual elements of the piezoelectric source cannot be approximated by baffled pistons.

We used the angular spectrum source characterization technique [76][71][59] to confirm that the observed focusing effect was a by-product of diffraction from the curved region surrounding the element. The acoustic field from the central element (10.6 mm in diameter) driven with a tone burst at 0.58 MHz was mapped along the focal plane. Angular spectrum theory was applied to back-propagate this planar measurement on to the source plane in order to determine the source characteristics; see Fig 3.3. The
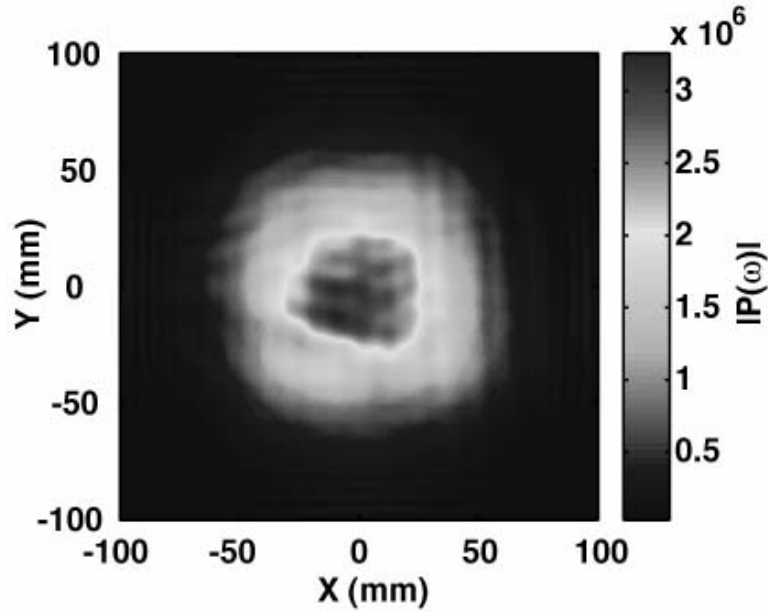
Figure 3.3: Source characteristics obtained by applying angular spectrum theory to back propagate pressure measurements from the central element (10.6 mm in diameter) driven with a tone burst at the center frequency.

source characterization performed using this method indicated that acoustic waves were radiated from an area of the transducer array approximately 100 mm in diameter rather than the 10.6 mm diameter of the element. This discrepancy could be due to two reasons: cross-coupling between elements; or reflection of diffracted waves from the curved region of the transducer. Laser Doppler vibrometry was used to determine that there was no significant cross-coupling between transducer elements as shown in Fig. 3.4. Thus we conclude that the diffraction was the dominant effect observed in the measurements.

The goal of this work is to customize the acoustic pressure distribution in the focal
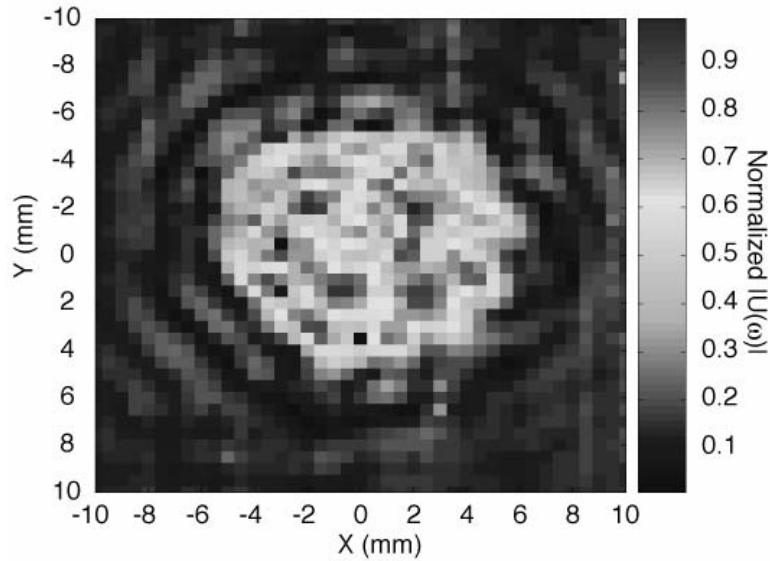
Figure 3.4: Map of particle velocity magnitude at the surface of the transducer array obtained using a laser doppler vibrometer when only the central element is driven with a tone burst at the center frequency (600 kHz). Measurements indicate that there is no significant cross-coupling between neighboring elements. The velocity had a -6 dB width of 10 mm, which is consistent with this element.

plane. Accurate inclusion of propagation effects including diffraction is essential for obtaining a reasonable model for forward wave propagation. The results shown here indicate that treating each element as a baffled piston will not be sufficient to achieve this goal.

3.3   Angular Spectrum Theory

The angular spectrum method provides a convenient accurate model for predicting diffractive wave propagation from one plane to any other parallel plane. The angular

spectrum technique is not easily adapted from a curved source to a plane at the focus. Therefore the approach employed in this study involved measuring the impulse response of each element individually on a pre-focal plane and then propagating each measurement forward to the focal plane using the angular spectrum theory while incorporating the time delay applied to each element.

The salient features of the angular spectrum theory will be presented in this section. Readers may refer to [59] for further details. Let the pressure $p(x, y, z, t)$ be monochromatic pressure with a temporal behavior $e^{-i\omega t}$. The propagation of the wave is assumed to be predominantly along the z axis. The pressure can be described in the frequency domain by taking a Fourier transform which is defined here as

$$P(x, y, z, \omega) = \int_{-\infty}^{\infty} p(x, y, z, t) e^{i\omega t} dt. \tag{3.4}$$

Given values of $P(x, y, z, \omega)$ on some $z = z_0$ plane, the angular spectrum is defined as the spatial Fourier transform of P with respect to x and y, defined here as

$$\widetilde{P}(k_x, k_y, z_0, \omega) = \int_{-\infty}^{\infty} \int_{-\infty}^{\infty} P(x, y, z_0, \omega) e^{-i(k_x x + k_y y)} dx dy. \tag{3.5}$$

Since $P(x, y, z, \omega)$ obeys the Helmholtz equation, the angular spectrum at any other plane of interest $z = z_1$ ($\forall \, z > z_0$) can be obtained b multiplication of the initial

angular spectrum by a k-space propagation operator G,

$$\tilde{P}(k_x, k_y, z_1, \omega) = \tilde{P}(k_x, k_y, z_0, \omega)G(k_x, k_y, z_1 - z_0), \tag{3.6}$$

where

$$G(k_x, k_y, z_1 - z_0) = e^{i(z_1 - z_0)\sqrt{k^2 - k_x^2 - k_y^2}}. \tag{3.7}$$

k is the free-space wave number. The propagation operator $\hat{G}$ required for determining

the the angular spectrum at a plane z_2 preceding the z_0 plane was shown to be the

complex-conjugate of $G(k_x, k_y, z_2 - z_0)$ [59]. The relationship described as a product

in k-space (Eq. 3.6) can be written as a convolution in the space domain:

$$P(x, y, z_1, \omega) = \int_{-\infty}^{\infty} \int_{-\infty}^{\infty} P(\acute{x}, \acute{y}, z_0, \omega)g(x - \acute{x}, y - \acute{y}, z_1 - z_0)d\acute{x}d\acute{y}, \tag{3.8}$$

where $g(x, y, z - z_0)$ is the inverse Fourier transform of the propagation operator:

$$g(x, y, z_1 - z_0) = \frac{1}{2\pi} \int_{-\infty}^{\infty} \frac{1}{2\pi} \int_{-\infty}^{\infty} G(k_x, k_y, z_1 - z_0)e^{i(k_x x + k_y y)}dk_x dk_y. \tag{3.9}$$

Stephanishen [77] showed that the space-domain propagation operator g in Eq. 3.9

can be written explicitly as

$$g(x, y, z_1 - z_0, \omega) = \frac{e^{ikr}}{2\pi r}\left(\frac{1}{r} - ik\right)\frac{z_1 - z_0}{r}, \tag{3.10}$$

64

where $r = \sqrt{x^2 + y^2 + (z_1 - z_0)^2}$. For the purposes in this work, the angular spectrum method was implemented in the form given in Eqs. 3.8 and 3.10.

3.4 Wave propagation model for the array source

Consider a source with L elements and focal axis along the z direction. Let the transducer focus be at (0,0,0). The pressure at any point (x, y) on the $z = z_0$ plane can then be defined as

$$p(x, y, z_0, t) = \sum_{l=1}^{L} h_l\left(x, y, z_0, t - \Delta t_l\right) \tag{3.11}$$

where $h_l\left(x, y, z_0, t - \Delta t_l\right)$ is the response of element l measured at (x, y, z_0) with a delay Δt_l. Equation 3.11 can be rewritten in the frequency domain as

$$P(x, y, z_0, \omega) = \sum_{l=1}^{L} H_l\left(x, y, z_0, \omega\right) e^{i\Delta t_l \omega}. \tag{3.12}$$

Defining a delay operator $D_l(\omega) = e^{i\Delta t_l \omega}$, the angular spectrum of P can then be obtained as

$$\widetilde{P}(k_x, k_y, z_0, \omega) \; = \; \int_{-\infty}^{\infty} \int_{-\infty}^{\infty} \sum_{l=1}^{L} H_l\left(x, y, z_0, \omega\right) D_l(\omega) e^{-i(k_x x + k_y y)} dx dy$$

$$= \sum_{l=1}^{L} \left(\int_{-\infty}^{\infty} \int_{-\infty}^{\infty} H_l\left(x, y, z_0, \omega\right) e^{-i(k_x x + k_y y)} dx dy \right) D_l(\omega)$$

$$= \sum_{l=1}^{L} \widetilde{H_l}\left(k_x, k_y, z_0, \omega\right) D_l(\omega). \tag{3.13}$$

where $\widetilde{H_l}\left(k_x, k_y, z_0, \omega\right)$ is the angular spectrum of $H_l\left(x, y, z_0, \omega\right)$. The resulting angular spectrum $P(k_x, k_y, z_0, \omega)$ can then be projected to another plane, for example $z = z_1$, as a convolution in spatial domain (Eq. 3.8). This procedure captures both the diffraction from each element and the delay.

The waveforms that will be employed in this work are relatively compact in time. This requires a large number of frequency components to be used for the angular spectra. The minimum number of frequency components necessary was determined by converting the signal into frequency domain, retaining a subset of the harmonic components and then converted back into a time domain signal. The procedure was repeated until a smallest possible set of frequency components that still faithfully represented the original wide-band signal was obtained (shown in Fig. 3.5). The wave propagation model presented above was implemented for all frequency components in this set. Pressure at any location in space can be obtained by taking an inverse Fourier transform.

Our implementation of the angular spectrum method was validated numerically by comparison with the analytical solution for a circular baffled piston (radius 10 mm,
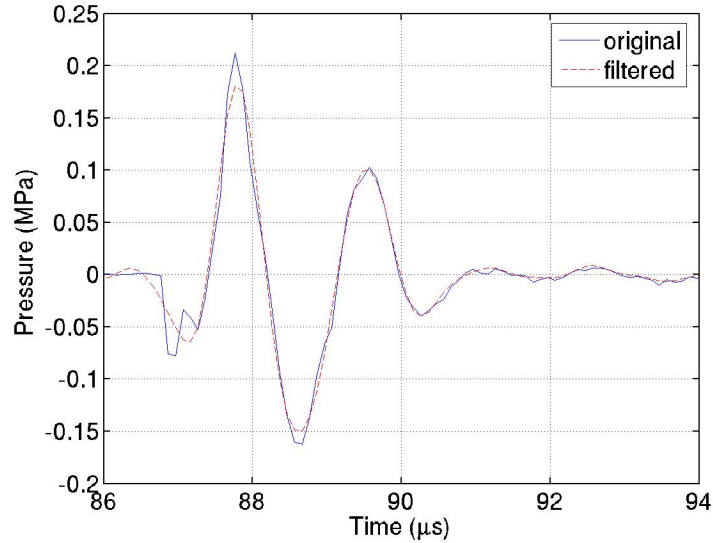
Figure 3.5: The original and filtered response obtained when the central element of the piezoelectric lithotripter array was excited with a 1.2 kV impulse. The filtered signal was obtained by applying the inverse Fourier transform to the smallest possible subset of the frequency components in the original response that adequately represented the original signal.

frequency 1 MHz). The axial pressure distribution for the piston was calculated by implementing the angular spectrum method and also by employing the direct analytical expression. The angular spectrum method was implemented using a discretization grid along the source plane that was 100 mm × 100 mm with an incremental distance of 1 mm. The analytical expression was taken from reference [7]. Figure 3.6 shows the axial pressure calculated using both methods. The result from the angular spectrum method agreed well with that obtained using the analytical expression. The discrepancy in the near-field magnitude could be attributed to insufficient discretization of the source plane.

67
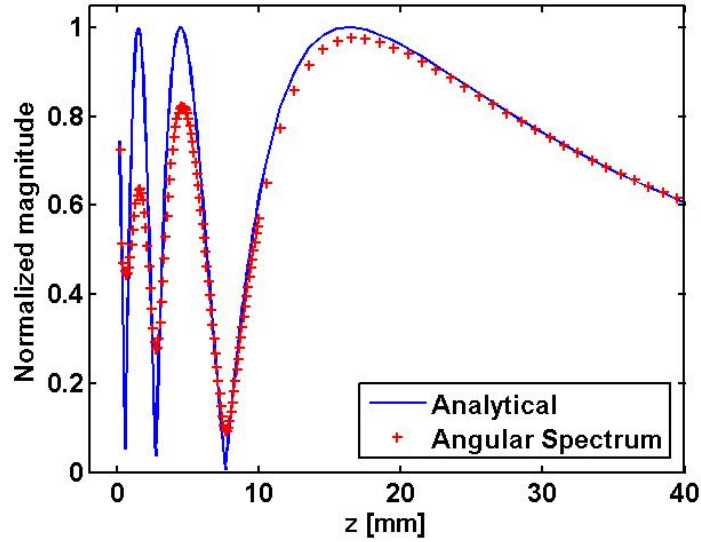
Figure 3.6: Pressure along the focal axis for a circular piston calculated using an analytical expression and the angular spectrum method.

The angular spectrum method was also validated experimentally for a single element, e_1. A 600 kHz tone burst (20 cycles) was used to drive the element. Pressure measurements were taken on a uniform grid 60 mm × 60 mm across the focal plane with an incremental distance of 1 mm. The acquired data was converted into the frequency domain and the 600 kHz component is shown in Fig. 3.7. The measurements indicate that the field is approximately axis-symmetric. The angular spectrum method was then used to project this field onto different z-planes and the pressure distribution along the focal axis was obtained. The pressure along the focal axis was also measured. The comparison between the measured axial pressure and the derived axial pressure is shown in Fig. 3.8. The theoretical axial pressure agreed well with
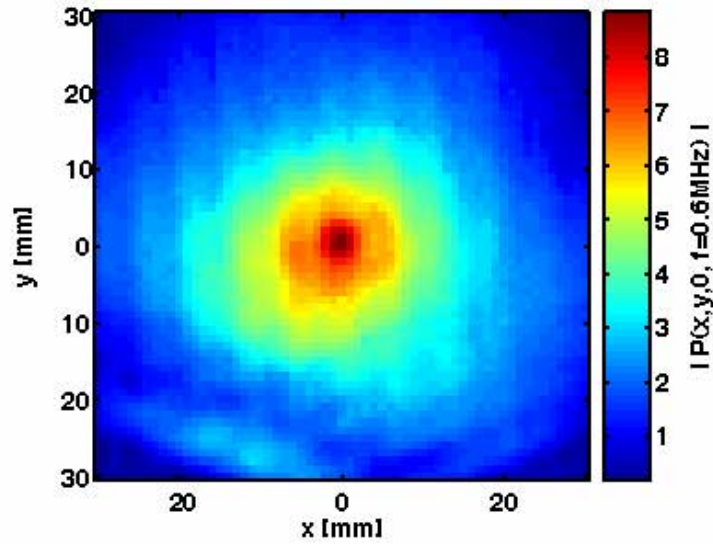
Figure 3.7: The magnitude 600 kHz component of the measured pressure across the focal plane.
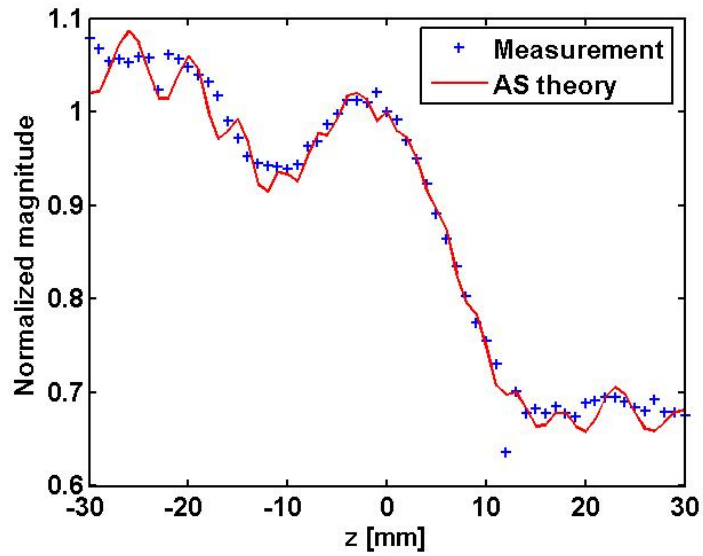
Figure 3.8: Comparison between the measured axial pressure and the axial pressure calculated using the angular spectrum method for 600 kHz component obtained from the central element.

the measurement (within 6 %). The agreement was good up to a range of -20 mm and 20 mm. These data confirm that the angular spectrum method is capable of capturing the details of the acoustic field in a way that the piston model could not accomplish (recall Fig. 3.2).
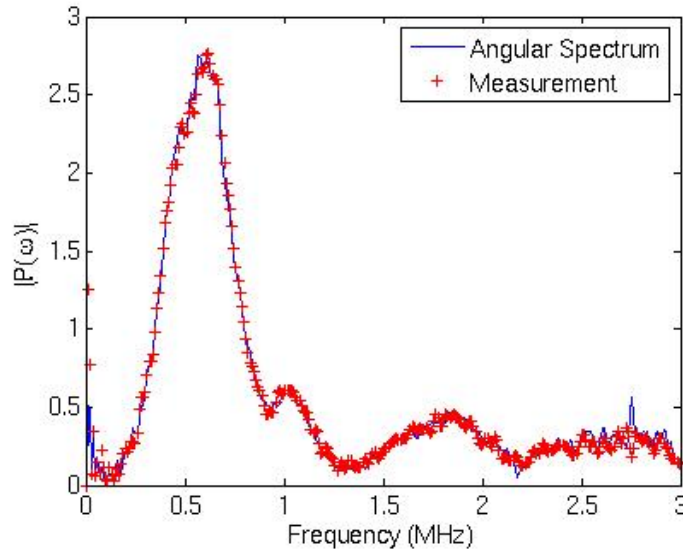
Figure 3.9: Comparison between the frequency spectrum of the measured focal waveform from the central element and the corresponding waveform simulated using the angular spectrum method.

The applicability of this method over a range of frequencies was verified in a similar fashion and Fig. 3.9 shows the frequency spectrum of a pulse waveform measured at the focus shown using "+". Overlaid is the frequency spectrum of a pulse waveform generated by simulating wave propagation to the focus from $z = -20$ (20 mm pre-focal) plane to the focal plane using the angular spectrum method shown in solid line. The simulations for the propagation from a single element to the focus are in good

agreement with the measurement.

The forward projection of the pressure field using the angular spectrum approach for a single element was extended to model the piezoelectric lithotripter array by linear superposition. For each element, pre-focal plane measurements were obtained and the field from that element could then be predicted at any other plane. Linear superposition of the acoustic field for each element resulted in the field for the entire array.

This method does not account for nonlinear effects. Therefore, it is unable to predict waveform asymmetry and peak pressures correctly as nonlinear distortion significantly increases the peak positive pressure. Furthermore, shifts in the field due to self-refraction will not be included in this model. However, all other propagation effects including diffraction are considered thus providing a relative prediction of the spatial pressure distribution and this was sufficient for customizing the acoustic field.

3.5   Optimization Scheme

The optimization scheme was implemented with the goal of determining the delays of each element so that the difference between a prescribed pressure field $\hat{P}(x, y, z, \omega)$ and a simulated pressure field was minimized. The prescribed pressure field was defined on a plane at $z = z_1$ over M control points $\hat{P}(x_m, y_m, z_1, \omega)$. The simulated

pressure at the $z = z_1$ plane resulting from a set of delays Δt_l is given by Eqs. 3.12 and 3.8 as

$$P(x, y, z_1, \omega) = \sum_{l=1}^{L} \left(\int_{-\infty}^{\infty} \int_{-\infty}^{\infty} H_l \left(\acute{x}, \acute{y}, z_0, \omega \right) g \left(x - \acute{x}, y - \acute{y}, z_1 - z_0 \right) \right) e^{i\Delta t_l \omega} d\acute{x} d\acute{y}.$$

(3.14)

Equation 3.14 can be rewritten for each point m in the control plane as the following sum over L elements:

$$P_m(\omega) = \sum_{l=1}^{L} \hat{H}_{ml}(\omega) e^{i\Delta t_l \omega}$$

(3.15)

where $\hat{H}_{ml}(\omega) = H(x, y, z_0, \omega) * g(x, y, z_1 - z_0)|_{x_m, y_m}$. The simulated pressure at all M points can be represented using M equations which can be written in matrix form as

$$\mathbf{P}(\omega) = \hat{\mathbf{H}}(\omega) \mathbf{D}(\omega)$$

(3.16)

where $\mathbf{D}(\omega) = e^{i\boldsymbol{\Delta t} \omega}$. Optimization can then be achieved by choosing $\mathbf{D}(\omega)$ such that the simulated pressure matches the prescribed pressure $\hat{\mathbf{P}}(\omega)$.

One optimization approach is to employ a direct inverse filter, *à la* Tanter et al. [79], in which Eq. 3.16 can be solved for $\mathbf{D}(\omega) = \left(\hat{\mathbf{H}}(\omega) \right)^{-1} \hat{\mathbf{P}}(\omega)$. Implementation of the inverse solution obtained in this manner results in a $\mathbf{D}(\omega)$ which typically will varying amplitude and phase. The high-voltage drivers used to drive the transducer array, however, produce a pulse of fixed amplitude and shape. That is, the hardware

imposes a constraint of $|\mathbf{D_1}(\omega)| = 1$. Further, because the only control available is over the time delay Δt_l of an element, the phase must be linear in frequency of the form $\Delta t_l \omega$.

Therefore, in this work an alternate method involving nonlinear regression of squared error was used to solve for optimal delays. For our purposes, the error function was defined as square of the difference in the amplitude:

$$\Pi = \sum_{n=1}^{N} \left(\sum_{m=1}^{M} \left(|\hat{\mathbf{P}}_{\mathbf{m}}(\omega_n)| - |\mathbf{P}_{\mathbf{m}}(\omega_n)| \right)^2 W_m \right), \qquad (3.17)$$

where W_m was a weighting function defined across M control points to allocate sensitivity of the optimization routine to the error at the m_{th} point. The frequency components used in the optimization (ω_n) are shown in the following section (Fig. 3.12). The weighting function was constant over the frequency range and was dependent on space alone. The Levenberg-Marquardt algorithm in the "lsqnonlin" function of the Matlab optimization toolbox [62] was used to search for the optimal set of delays Δt_l that minimized Π. An initial set of delays was used to determine $\mathbf{P}(\omega)$ using Eq. 3.15. The details of the trends for the error and directional derivatives are shown in the appendix.

3.6 Implementation

The details related to implementing optimization are presented in this section. Due to the computationally intensive nature of the optimization problem, careful implementation was necessary to allow for timely convergence to the prescribed acoustic field. All calculations that did not include the delay term, were performed prior to the optimization and stored for use at each iteration.

The response $h(x, y, z_0, t)$ was obtained for each element at $z_0 = -20$, that is 20 mm pre-focal, on a 50 mm $\times$ 50 mm grid with inter-node distance of 0.5 mm and then zero-padded to 80 mm $\times$ 80 mm to reduce wraparound errors that may occur during convolution in space. As mentioned in Sec. 2.2, the elements of the transducer array are arranged on the transducer bowl axis-symmetrically and for a time-invariant medium the response of any element on a ring can be obtained by appropriately rotating the response from another element on the same ring because all elements on any given ring have the same shape. The angle of rotation is given simply by the difference of the angles of the two elements. For instance the response of e170 on the axisymmetric plane $z = z_0$ can be obtained by rotating the response of e135 measured on the same plane by 60° as shown in Fig. 3.10. The rotation of the field was performed using a Matlab function IMROTATE while emplying a linear interpolation scheme. The response for each plane was then projected forward to the

(a) e_{135} rotated by 60°   (b) e_{170}
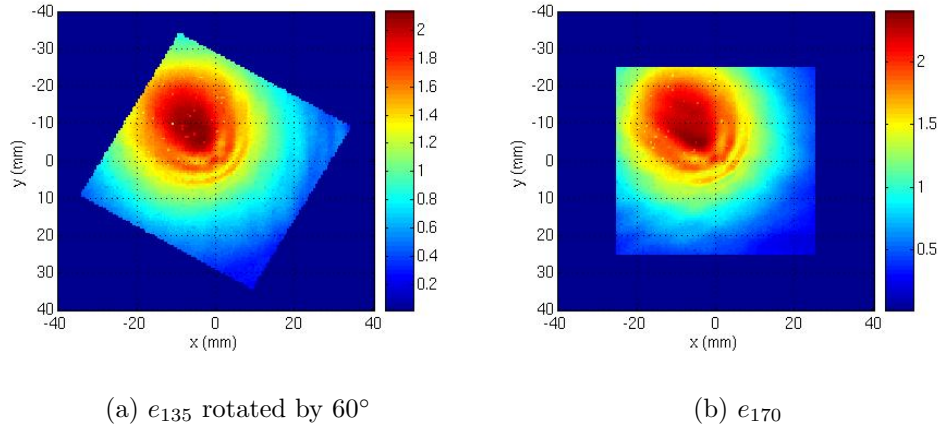
Figure 3.10: (a) Impulse response of e_{135} measured at 20 mm pre-focal and rotated by 60°
(b) Impulse response of e_{170} measured at 20 mm pre-focal.

focal plane using angular spectrum theory.

The optimization routine was implemented for either customizing the -6 dB focal width or for manipulating the spatial pressure distribution to create a ring shaped pressure distribution of a prescribed diameter. The optimization scheme requires an initial guess for the delays. The results from the optimization routine for a prescribed acoustic field of increased -6 dB focal width were not heavily dependent on the initial guess for the delays. In order to assign an initial state of no delay, a constant delay (1 μs or 3 μs) was applied to all the elements. This was done to prevent negative results for time delays.

Alternately, the initial delays were obtained such that they were associated with the range from the elements to various points on ring on the focal plane. This method

(a) Wide focus optimization (b) Ring focus optimization
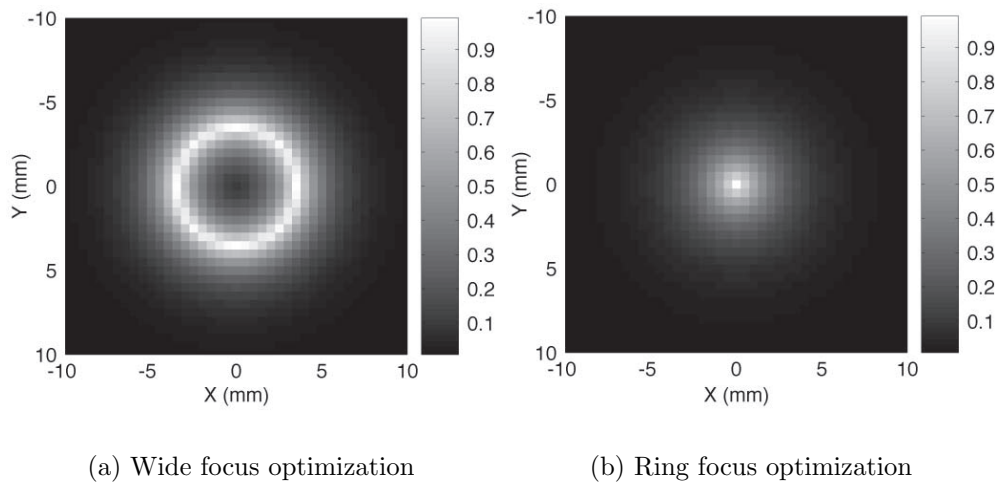
Figure 3.11: The weight function employed to control the emphasis given to error at each node on the optimization plane for customizing the spatial distribution of pressure.

could be used for widening the focus (by choosing small ring diameters) or for obtaining a ring shaped focal pressure field. Successful results for ring focal fields were especially dependent on the initial guess for the time delays. In this case the elements were divided into 8 groups, for instance, elements 1,9,17...169 comprised the first group, elements 2,10,17...170 were in the second group and so on. For each group, a corresponding point was chosen on the ring focus of the desired diameter and the initial delays set so that the group focused to that point. The initial delays and the corresponding results are presented in the appendix.

The control points for prescribed pressure consisted of a 10 mm × 10 mm grid with inter-node distance of 0.5 mm. Pressure at each node was scaled according to the desired spatial pressure distribution. The error function was defined over the control

76

points in terms of the difference between the magnitude of the predicted pressure and the magnitude of the prescribed pressure according to Eq. 3.19. The weight function W_m was employed to control the emphasis given to the error at each node. The error-weight functions for the wide focus optimization and the ring focus optimization are shown in Fig. 3.11. The weight function for obtaining the wide focus was given by $W(x, y) = e^{-\left(\frac{|r-\hat{r}|}{r_0}\right)}, r_0 = 1.5$ mm and placed emphasis over a ring wider than the desired -6 dB focal width ($\hat{r}$ has a value equivalent or up to 2 mm greater than the desired -6 dB focal width, $r = \sqrt{x^2 + y^2}$). The weight function for the ring optimization, $W(x, y) = e^{\frac{-r}{r_0}}, r_0 = 2$ mm, placed the maximum emphasis on the error on the beam axis, as the ring shaped focus is contingent on reducing the pressure amplitude on and near the focal axis. Appropriate selection of the initial guess for the delays and the weight function for each specific prescribed acoustic field facilitates efficient convergence to the prescribed acoustic field.

Since the error function is defined in the frequency domain, solving the optimization problem for the time delays for a single frequency component was not sufficient for customizing acoustic fields consisting of wide-band pulses. Therefore multiple harmonics were considered as shown in Eq. 3.17. Including all harmonics is too computationally expensive. Therefore 10 equally spaced harmonics ranging from $0.3-1.2$ MHz were chosen to represent the frequency characteristics of the waveform. Figure 3.12 shows the frequency spectrum of the waveform from a single element. The harmonics used
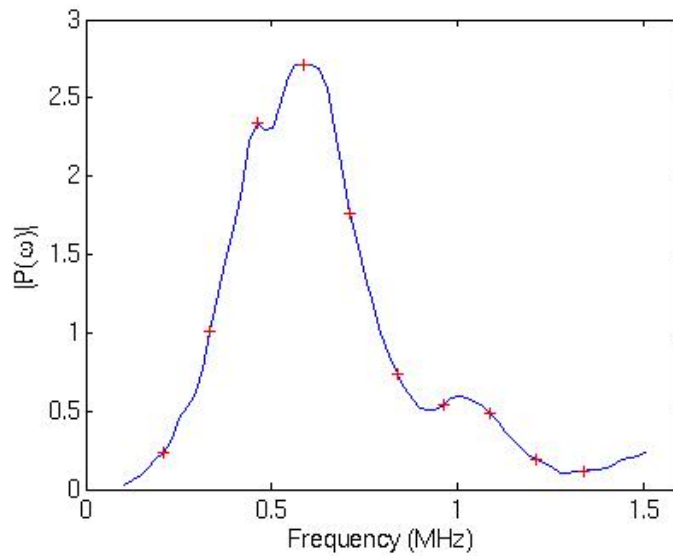
Figure 3.12: Frequency spectrum of the waveform from a single element. The frequency components used in the optimization scheme are represented by '+'.

for the optimization scheme to define the error function are represented by '+'.

This optimization scheme for obtaining different acoustic fields was implemented with the intention of enhancing specific stone fragmentation mechanisms selectively to better identify those mechanisms that play a major role in a successful treatment. The corresponding results are presented in the following chapter.

Chapter 4

Results

The results will be presented in three sections. The first section implements the acoustic field optimization and compares the predicted pressure distributions to measurements. The second section will consist of characterization of the cavitation resulting from the acoustic field produced by the array source including the customized pressure fields and waveforms and waveforms designed to reduce cavitation. The third section will focus on stone fragmentation studies designed to determine the effectiveness of the different acoustic fields for stone comminution. Statistical analysis was carried out using the 2-tailed student t-test with null hypothesis of "means are equal" and significance at $p < 0.05$ level.

4.1 Acoustic Field Customization

The time delay for each element is the only control parameter for optimization in the current piezoelectric array. Furthermore, the high voltage drivers can produce a pulse of up to 1.2 kV limiting the maximum pressure amplitude of each element to about 0.2 MPa. Therefore, the current system suffers some inherent limitations. The optimization routine is based on regression of least squared error between the prescribed and numerically predicted pressure fields which resulted in a customized acoustic field similar but not exactly equivalent to the desired acoustic field. Typically, a more complex desired acoustic field would result in a larger compromise in the amplitude of the acoustic pulse. In this work, no constraint was placed on pressure magnitude during acoustic field customization.

4.1.1 Spatial pressure distribution

As described in Chapter 2, the proposed mechanisms of stone fragmentation associated with stress can be investigated by manipulating the spatial distribution of acoustic pressure incident on the stone. The optimization routine was employed using prescribed fields of different focal widths defined as -6 dB re P_{1+}. The optimal set of delays for the array, for each focal width, was first investigated using the forward propagation model discussed in Chapter 3 and then implemented in hardware and

experimentally measured. The resulting optimal delays are shown in the appendix and the resulting acoustic fields are presented below.

Figure 4.1 shows the simulated pressure distribution (based on a driving voltage of 1 kV) of P_{1+} along the lateral axis X obtained from the optimization routine for varying focal widths. The displayed results were obtained from the linear forward wave propagation simulations using the set of optimal delays determined for each of the desired -6 dB focal widths. As the only control parameter used for optimization is the time delay for each element and the optimization is based on minimization of least square errors, the resulting simulated pressure fields do not exactly match the prescribed pressure field. However, an increase in the desired acoustic focal width resulted in an increase in the focal width of simulated pressure obtained using the optimal time delays. Prescribed focal widths 3 mm, 4 mm, and 5 mm resulted in simulated focal widths of 3.4 mm, 3.6 mm, and 5.1 mm. The focal width obtained by setting the delays to zero was 2.9 mm.

The ability to manipulate the -6 dB focal width was also confirmed using experimental measurements as shown in 4.2. The acoustic field was mapped using the PVDF membrane hydrophone while the array was driven using the appropriate optimal delay-set for each of the prescribed focal widths. The driving voltage for each run was adjusted so that magnitude of P_{1+} at X = 0 was roughly 40 MPa for all focal widths with the long term goal of investigating the dependence of stone fragmenta-
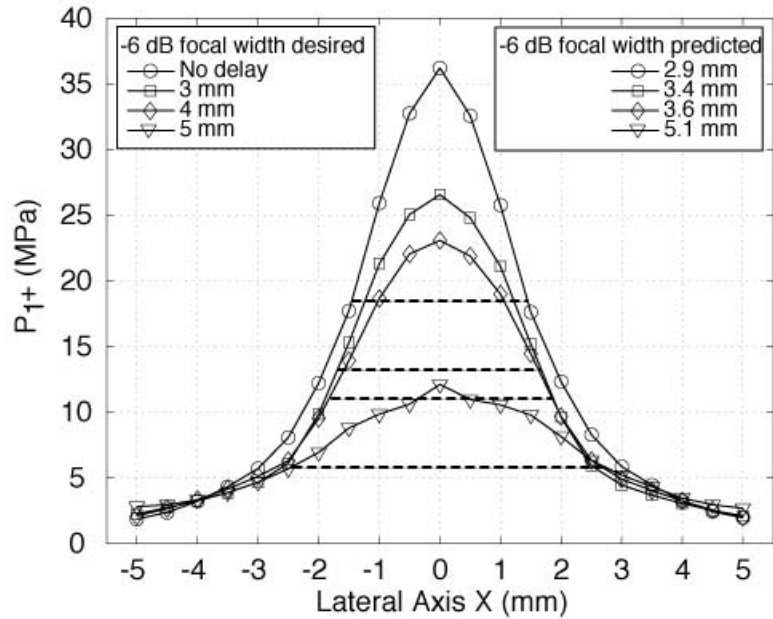
Figure 4.1: Simulated distribution of P_{1+} along the lateral axis X produced from the optimization routine for desired focal widths of 3 mm, 4 mm, and 5 mm (left legend). The optimal delays were predicted to produce focal widths of 3.4 mm, 3.6 mm, and 5.1 mm (right legend). The predicted focal width when all elements were fired synchronously was 2.9 mm.

tion on focal width alone. The driving voltages for 5 mm, 4 mm, and 3 mm focal widths were 1200 V, 850 V, and 800 V respectively. The ND field with a maximum $P_{1+} = 40$ MPa was obtained by driving the elements at 575 V.

Similar to the wave propagation simulations, the measured focal widths increased with increase in prescribed focal width. Prescribed focal widths 3 mm, 4 mm, and 5 mm resulted in simulated focal widths of 2.8 mm, 3.1 mm, and 3.9 mm. The focal width measured when all elements were driven synchronously was 1.7 mm which is smaller than that predicted by the simulations. The discrepancy can be attributed to
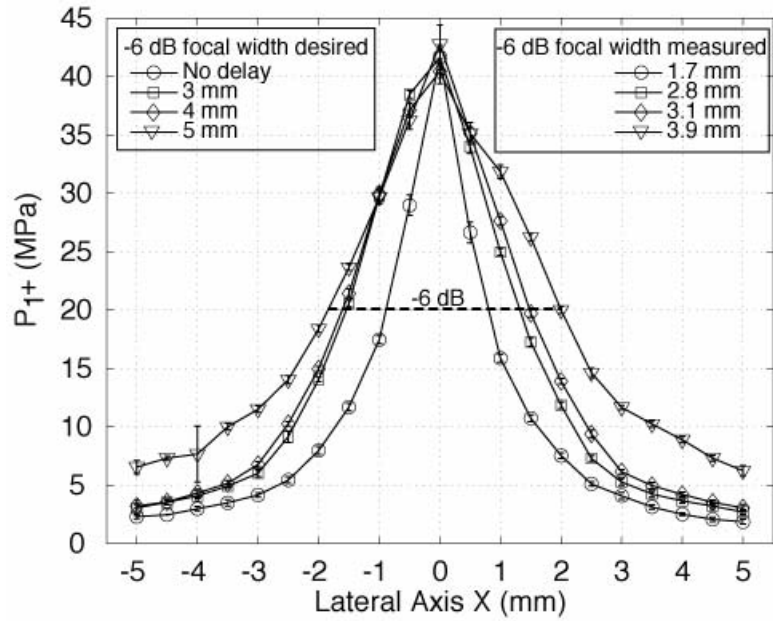
Figure 4.2: Measured distribution of P_{1+} along the lateral axis X produced from the optimization routine for desired focal widths of 3 mm, 4 mm, and 5 mm (left legend). The optimal delays produced focal widths of 2.8 mm, 3.1 mm, and 3.9 mm (right legend). The focal width when all elements were fired synchronously was 1.7 mm.

the fact that the simulation is linear and the higher harmonics generated due to the nonlinear effects will lead to tighter focusing of the acoustic field. The focal width of 3.9 mm was the maximum possible focal width while maintaining $P_{1+} = 40$ MPa. As shown in Chapter 2, the focal width when all elements are driven at 1 kV with zero delay was 1.4 mm. The optimization routine scaled the focal width by a factor of 2 with a 33 % reduction in the magnitude of P_{1+}.

Figure 4.3 shows the distribution of P_1+ and P_2- over the axial plane. The measurements indicated that the optimal method of producing a wide pressure region at $Z = Z_0$ plane is to adjust the delays to shift the focus of the array towards the

(a) Axial map of P_1+ (b) Axial map of P_2-
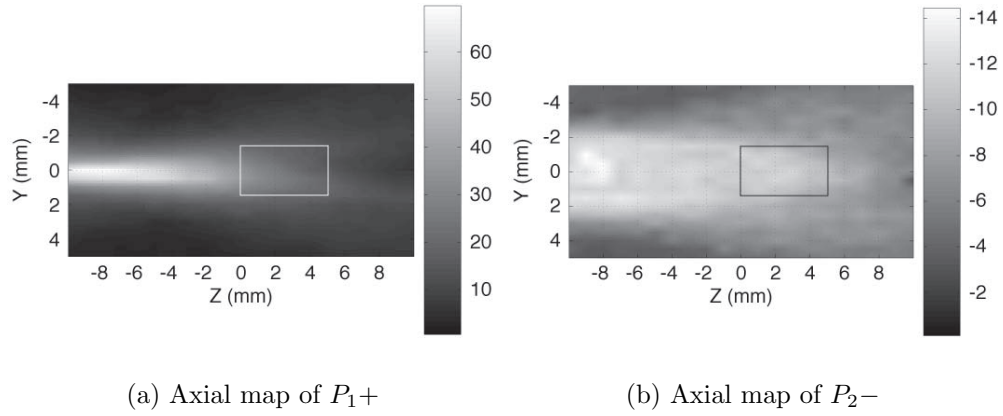
Figure 4.3: Axial pressure maps for -6 dB focal width of 3.9 mm from measurements acquired using the PVDF hydrophone. The rectangle denotes the location of the stone.

array. For truly widening the focus without shifting it towards the source, additional constraints in the pre-focal and post-focal region might be including during the optimization routine.

Since shear and squeezing effect are contingent upon the presence of a large amplitude pressure field on the periphery of the stone, a ring-shaped focal pressure distribution was desirable to isolate these effects from spallation. The optimization routine was applied to obtain a specific diameter of the pressure ring based on P_{1+}. No constraint was applied on the maximum magnitude of P_{1+}.

Figure 4.4 shows simulated and measured spatial pressure distribution based on P_{1+} and P_{2-} from the optimization routine aimed at obtaining a ring-shaped pressure distribution. Prescribed ring diameters of 4 mm and 7 mm are shown. The optimization routine was successful in producing a ring-shaped focal field. Simulated
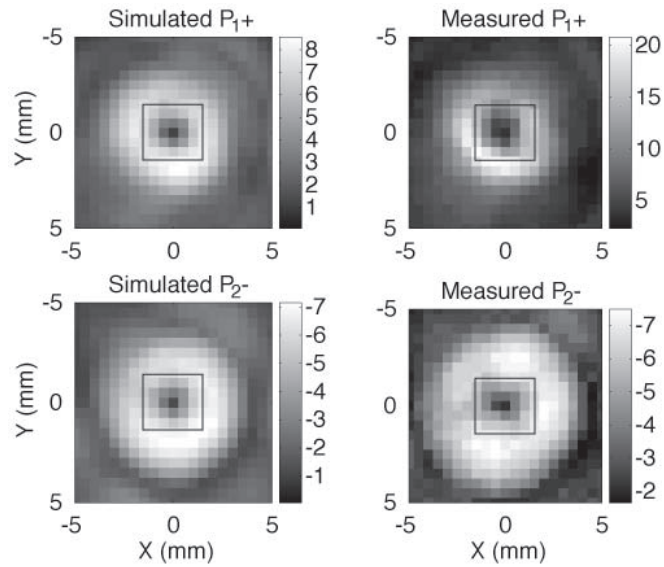
(a) Prescribed diameter 4 mm
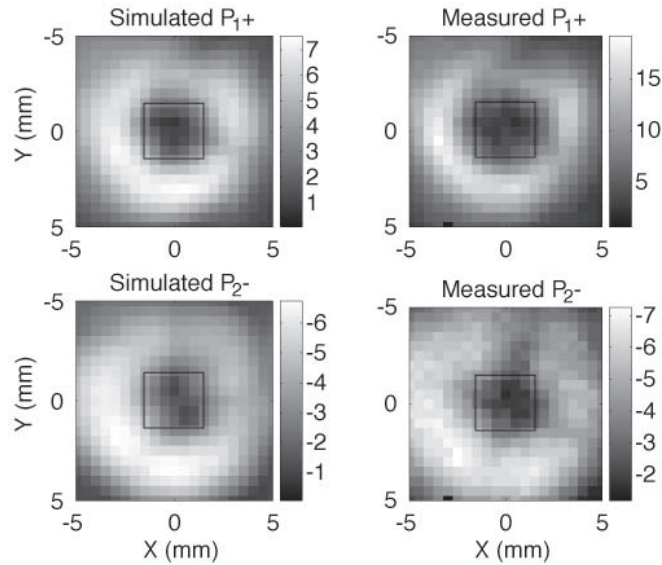
(b) Prescribed diameter 7 mm

Figure 4.4: The results from optimization routine aimed at obtaining a ring-shaped pressure distribution. Left frames field maps obtained using the angular spectrum model. Right frames are field maps from measurements acquired using the PVDF hydrophone. (a) Prescribed ring diameter of 4 mm (b) Prescribed ring diameter of 7 mm. Color-bars represent pressure in MPa. Squares denote the location of the stone.
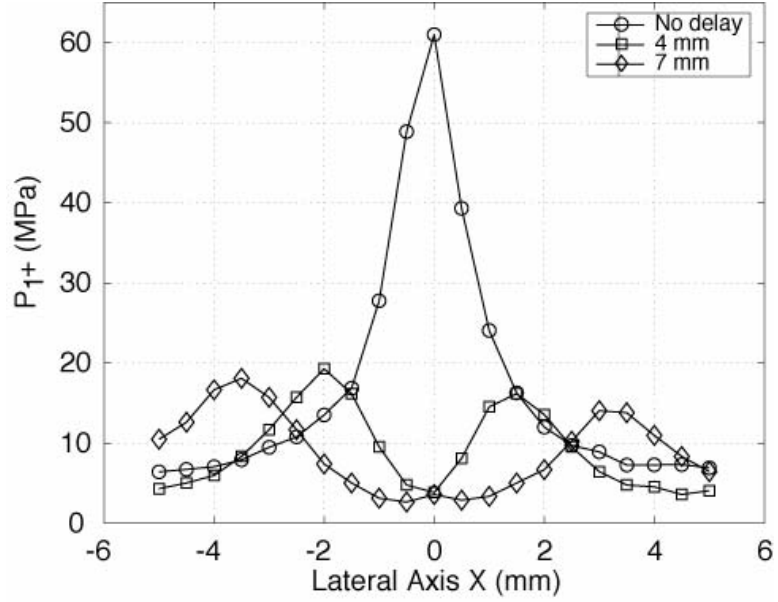
Figure 4.5: Comparison between pressure distribution (P_{1+}) along a lateral axis (X) obtained from measurements across the focal plane for acoustic field obtained by driving elements synchronously and the ring pressure distribution of diameters 4 mm and 7 mm.

field obtained using the linear angular spectrum wave propagation model and the field obtained from measurements when the array was driven using the set of optimal delays determined for each ring diameter were in good agreement. The discrepancy in the magnitude of P_{1+} can be attributed to the fact that the angular spectrum approach employed to model wave propagation in this work does not include nonlinear effects and thus cannot predict the rise in peak positive pressure induced by nonlinear distortion of the ultrasound pulse.

Figure 4.5 shows the measured distribution of P_{1+} along the lateral axis X for ring shaped acoustic fields of diameters 4 mm and 7 mm (driving voltage of 1.2 kV)

86

(a) Axial map of P_1+ (4 mm ring)

(b) Axial map of P_2- (4 mm ring)

(c) Axial map of P_1+ (7 mm ring)

(d) Axial map of P_2- (7 mm ring)
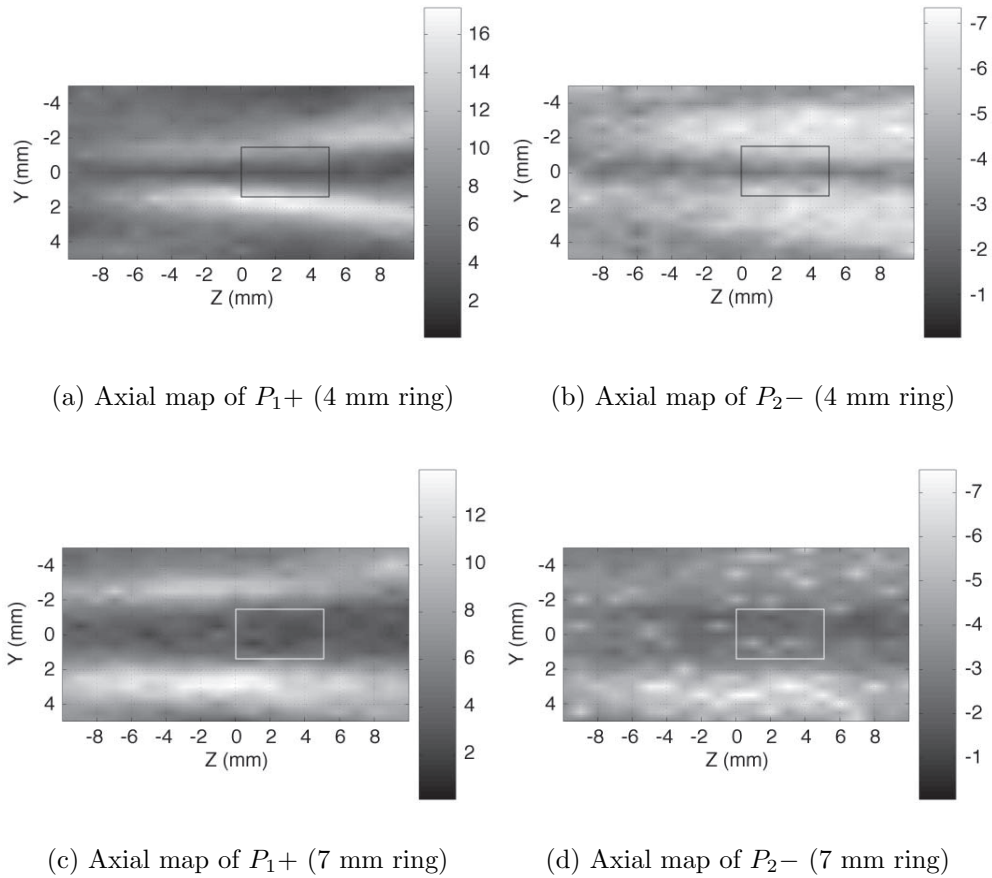
Figure 4.6: Axial pressure maps for acoustic field with a ring 4 mm and 7 mm in diameter from measurements acquired using the PVDF hydrophone. The rectangle denotes the location of the stone.

compared to that obtained when elements are driven synchronously at 1 kV. The "no delay" waveform had a maximum pressure in excess of 60 MPa. In contrast, both ring pressure distributions had a pressure minimum on axis with a peak less than 5 MPa. The ring focal field peaked off-axis at an amplitude higher than the no-delay field. However, the peak pressures did not exceed 20 MPa.

Figure 4.6 shows the distribution of P_1+ and P_2- over the axial plane for acoustic

field with a ring 4 mm and 7 mm in diameter. The measurements indicated that the optimization routine for producing ring acoustic fields does indeed reduce the pressure at the focus and the ring shape is maintained over the length of the stone.

Table 4.1: Parameters from ring field optimization

	Simulated		Measured	
Prescribed Diameter (mm)	4	7	4	7
X Diameter (mm)	3.5	6	3.5	6.5
Y Diameter (mm)	3.5	6	3.5	6
Mean Ring Thickness (mm)	$\sim$3	$\sim$3	$\sim$2	$\sim$3
P_{1+} at focus (MPa)	1	1	4	4

The relevant parameters from the ring-optimization are shown in Table 4.1. Both the simulations and the measurements were obtained at a spatial resolution of 0.5 mm. The ring diameter was determined along both lateral axes based on the maximum value of P_{1+} in the focal plane. Both the simulated and measured ring diameters resulting from the optimization routine was consistent with the prescribed ring diameter. The ring thickness based on -6 dB re P_{1+} (local peak) was between 2 mm and 4 mm in all the cases. The magnitude of P_{1+} at the focus obtained using the angular spectrum simulation was around 1 MPa and that observed through measurements was 4 MPa.

Sample waveforms at four points that lie on the peak of the ring pressure field are displayed in Figs. 4.7 (a) and (c). Since the ring pressure distribution is not exactly symmetrical four sampling locations were chosen from the points that constitute the
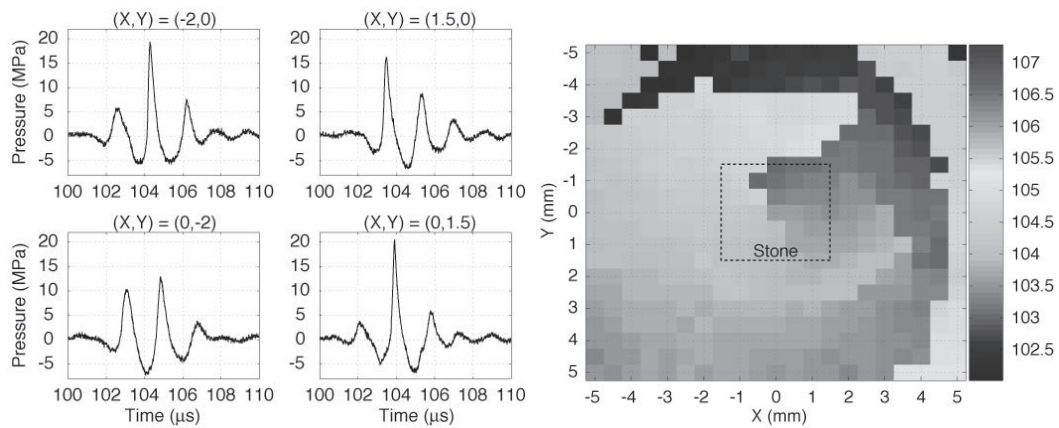
(a) Sample waveforms for 4 mm ring

(b) Map of arrival time (μs) of P_{1+} for 4 mm ring
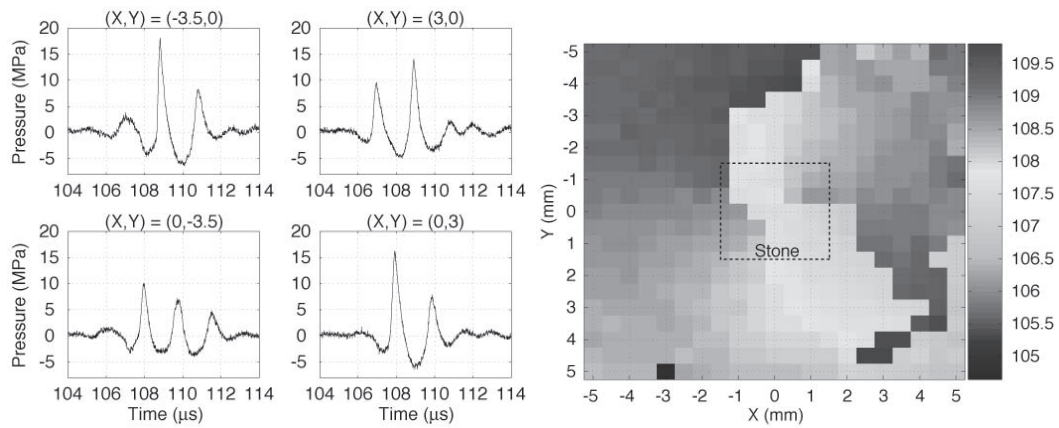
(c) Sample waveforms for 7 mm ring

(d) Map of arrival time (μs) of P_{1+} for 7 mm ring

Figure 4.7: Sample waveforms measured at the focal plane when the array was driven using the optimal delays for both the prescribed ring diameters. The measurements indicate spatial variation in the time of arrival of the waveforms. Waveforms recorded are not true shock waves.

maximum ring pressure. The measured waveforms indicate that different portions of the ring consist of different waveform shapes. In both cases, the measurements indicate that the time of arrival of the waveforms is not uniform at all locations on the focal plane. This can be attributed to the optimization routine with only time delays as the control parameter in which the pressure distribution was the only constraint and no constraint was placed on phase. The difference in arrival times of pulses at different locations on the ring presents a need for including an arrival time constraint (which was beyond the scope of this work) in the optimization routine for the ring pressure distribution. The variation in the arrival time in space is illustrated in maps of arrival time of waveform based on P_{1+} in Figs. 4.7 (b) and (d). The maps indicate that portions of the ring do have uniform arrival but the arrival times varied by up to 2 μs around the stone's circumference for the 4 mm ring.

4.1.2 Waveform Shape

As discussed in Chapter 2, the role of cavitation in fragmentation can be controlled by manipulating the waveform shape of the incident shock wave. More specifically, cavitation related effects could be affected by manipulating the integral of the negative phase of waveform. Waveform shaping was achieved by adjusting the delays for the elements in an *ad hoc* fashion (detailed methodology presented in Chapter 2) to affect the negative portions of the waveform. No constraints were employed on positive

pressure or spatial distribution. The ability to manipulate the waveform shape was further enhanced by firing some of the transducer elements twice during the generation of one pulse.

(a) No delay $\qquad$ (b) Reduce P_1- $\qquad$ (c) Reduce P_2-
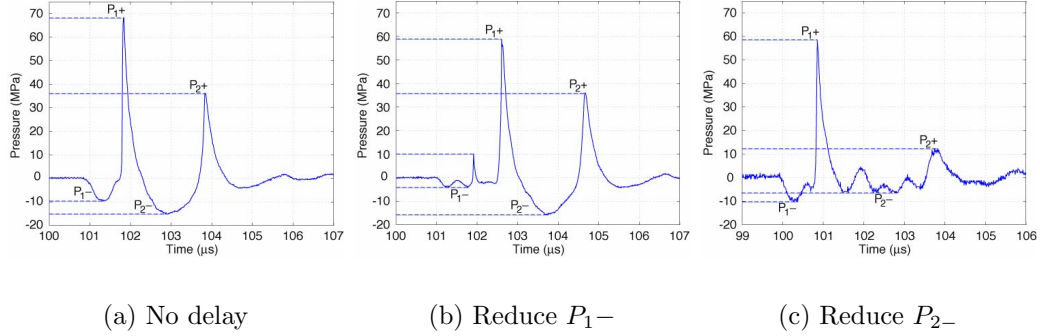
Figure 4.8: Waveform shaping for controlling the role of cavitation.

Waveform shape was customized to either inhibit the cavitation effects resulting the negative precursor (P_1-) and the main negative phase (P_2-) as shown in Fig. 4.8. When all elements were driven synchronously, the waveform consisted of a negative precursor with a local peak of -10 MPa and a duration of 0.5 μs (Fig. 4.8 (a)). This precursor will induce cavitation which can have significant influence on stone fragmentation (details in the next section). The influence of the negative precursor was diminished by reducing the magnitude of the local negative peak within the precursor (P_1-) from 10 MPa to about 4 MPa and introducing a positive peak ($\sim$10 MPa) following the negative precursor as shown in Fig. 4.8 (b). The loss in magnitude suffered by P_{1+} was 13 %. The "strength" of cavitation depends critically on the time integral of the negative phase of the shock wave or $\int -pdt$. Table 4.2

shows the calculated integral values for both the negative precursor and the main

negative phase of the SW for the three waveforms.

Table 4.2: Pressure-time integral (units of MPa·μs) of the negative phases of the shock waves produced by the piezoelectric lithotripter array

Waveform Type	Negative precursor	Main negative phase
No delay	-9	-22
Reduce P_1-	-4	-15
Reduce P_2-	-7	-7

Despite the second positive shock front, the main negative phase of the shock wave

($P_{2-} = -16$ MPa) could lead to significant cavitation related effects in stone frag-

mentation. The main tensile phase of the shock wave was also reduced by adjusting

the inter-element delays as shown in Fig. 4.8 (c). The resulting waveform had main

negative peak (P_{2-}) of around -6 MPa compared to -15 MPa in the original wave-

form. The integral of the main negative phase was reduced and the trailing positive

phase was reduced to $P_{2+} \approx 10$ MPa. The reduction in the main negative phase of

the shock wave was accompanied by a 14 % reduction in P_{1+}.

The lateral (XY) and the axial (YZ) maps of P_1+. amd P_1-, and P_2- for the the

three types of waveforms discussed above are shown in Figs. 4.9 and 4.10 respectively.

The lateral measurements were acquired on a square grid 10 mm × 10 mm with

increments of 0.5 mm. Measurements along the axial plane were acquired on a grid

that was 20 mm long along the Z (focal) axis with increments of 1 mm and 10 mm

(a) P_1+ map (No delay)

(b) P_1+ map (Reduce P_1-)

(c) P_1+ map P_1+ (Reduce P_2-)

(d) P_1- map (No delay)

(e) P_1- map (Reduce P_1-)

(f) P_1- map (Reduce P_2-)

(g) P_2- map (No delay)

(h) P_2- map (Reduce P_1-)

(i) P_2- map (Reduce P_2-)
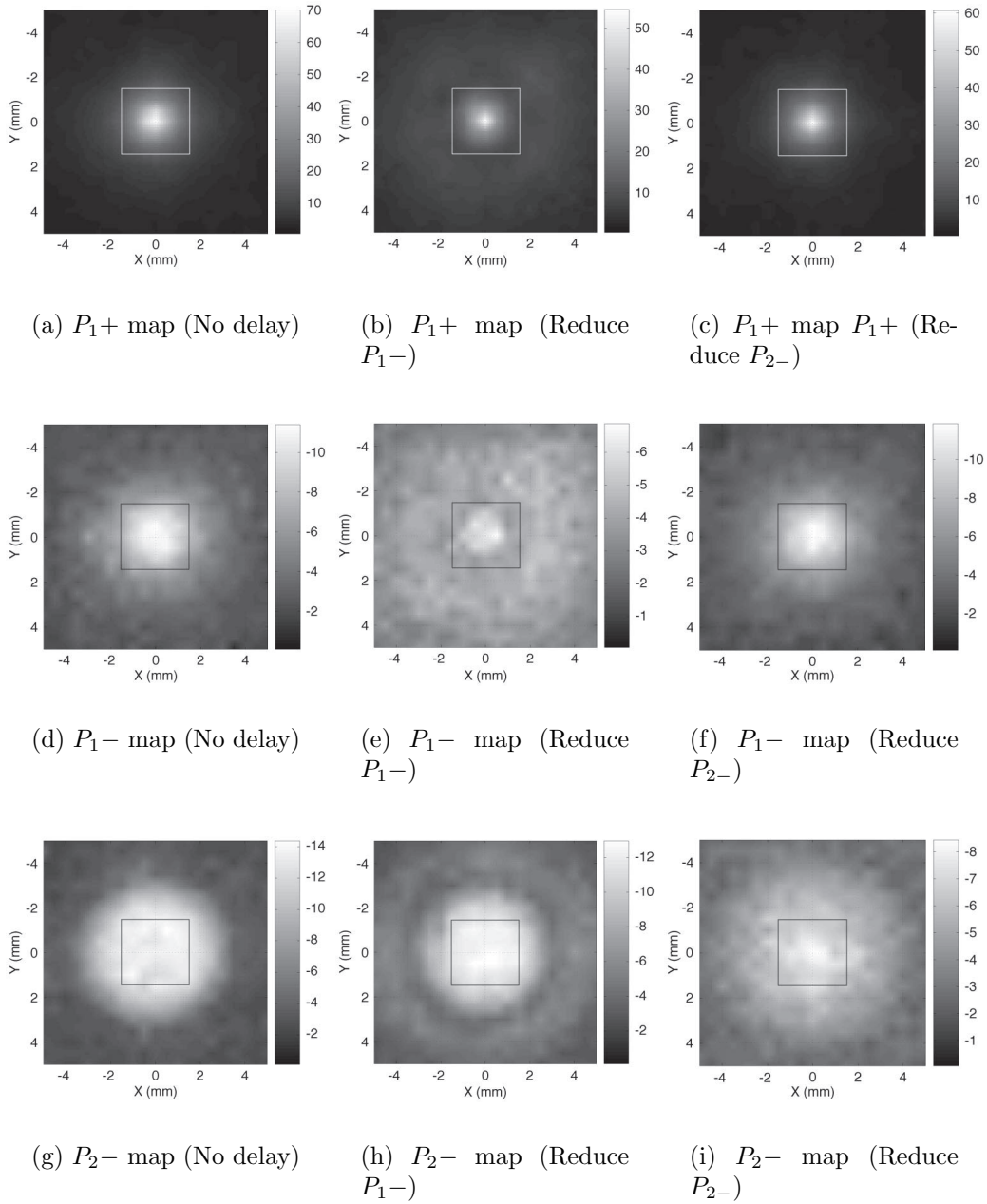
Figure 4.9: Lateral maps of P_1+, P_1-, and P_2- for the three waveforms: waveform obtained by driving the elements simultaneously, waveform designed to reduce P_1-, and waveform designed to reduce P_2-. The color-bar represents pressure in MPa. Measurements indicate that the modified waveforms still produce a tight focus comparable to the no delay field.

(a) P_1+ map (No delay)   (b) P_1+ map (Reduce P_1-)   (c) P_1+ map P_1+ (Reduce P_2-)

(d) P_1- map (No delay)   (e) P_1- map (Reduce P_1-)   (f) P_1- map (Reduce P_2-)

(g) P_2- map (No delay)   (h) P_2- map (Reduce P_1-)   (i) P_2- map (Reduce P_2-)
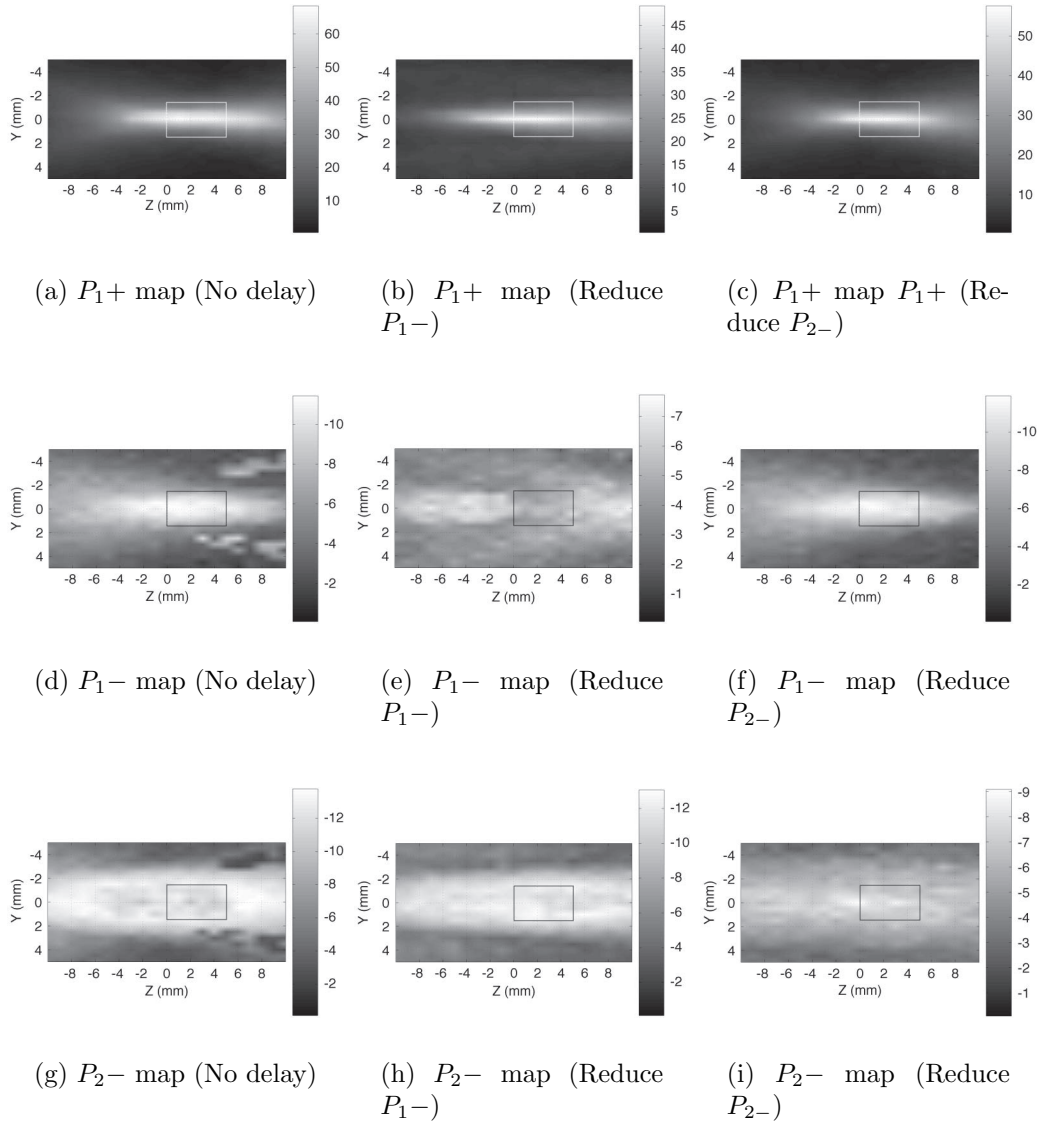
Figure 4.10: Axial maps of P_1+, P_1-, and P_2- for the three waveforms: waveform obtained by driving the elements simultaneously, waveform designed to reduce P_1-, and waveform designed to reduce P_2-. The color-bar represents pressure in MPa. Measurements indicate that the modified waveforms still produce a tight focus comparable to the no delay field.

wide along the Y axis with increments of 0.5 mm. The measurements were then interpolated to yield smooth pressure distributins on a grid such that incremental step for X, Y, and Z, were 0.1 mm, 0.1 mm, and 0.2 mm respectively.

Table 4.3: Dimensions of spatial pressure distribution based on -6 dB values of P_1+, P_1-, and P_2- for unmodified and modified waveforms.

Axis	Waveform type	-6 dB of P_1+	-6 dB of P_1-	-6 dB of P_2-
X	No delay	1.7 mm	6.3 mm	5.6 mm
Y	No delay	1.7 mm	6.3 mm	5.6 mm
Z	No delay	> 14.4 mm	> 20 mm	> 20 mm
X	Reduce P_1-	1.2 mm	7.1 mm	> 9.5 mm
Y	Reduce P_1-	1.2 mm	7.1 mm	> 9.5 mm
Z	Reduce P_1-	> 15 mm	> 20 mm	> 20 mm
X	Reduce P_2-	1.4 mm	7.7 mm	4.2 mm
Y	Reduce P_2-	1.4 mm	7.7 mm	4.2 mm
Z	Reduce P_2-	12.5 mm	> 20 mm	> 20 mm

The spatial pressure distributions, particularly that of P_1+, obtained using the modified waveforms is qualitatively similar to those obtained when all elements are driven simultaneously. The spatial distribution of P_2- obtained from the SWs designed to reduce P_1- is in good agreement with that for the no delay case. Similarly, the spatial distribution of P_1- for the SWs designed to reduce P_2- is consistent with that for no delay. Table 4.3 shows the dimensions of the spatial pressure distribution based on -6 dB values of P_1+, P_1-, and P_2- for the original and waveforms designed to control cavitation.

4.2 Cavitation

Cavitation results will be presented in three parts. The cavitation measurements in the free field will be shown first followed by numerical predictions of a single spherical bubble to the measured customized waveforms. Lastly, passive cavitation detector measurements of cavitation on the proximal surface of the stone will be presented and compared to the numerical predictions obtained using the Gilmore formulation.

4.2.1 Free field characterization

Free field cavitation was characterized by simultaneously measuring the incident SW with the FOPH and monitoring cavitation using the DPCD and the high speed camera (recall Fig. 2.9). The measured response of a single bubble to an incident lithotripter pulse is shown in Fig. 4.11. The measured pressure waveform was used as an input to a numerical model for bubble dynamics based on the Gilmore equation, the prediction of which was compared to measured cavitation. The top two frames show the incident SW measured by the FOPH and the response of a single bubble in terms of r-t curve predicted by the Gilmore formulation. The model predicted a short growth phase corresponding to the negative precursor of the wave followed by a forced collapse by the main compressive pulse. The main negative trough induces a larger cavitation bubble with a predicted maximum radius of about 175 μm which then collapsed

96

inertially 35 μs after the inception of bubble growth. The model also predicts several

rebound collapses following the inertial collapse.
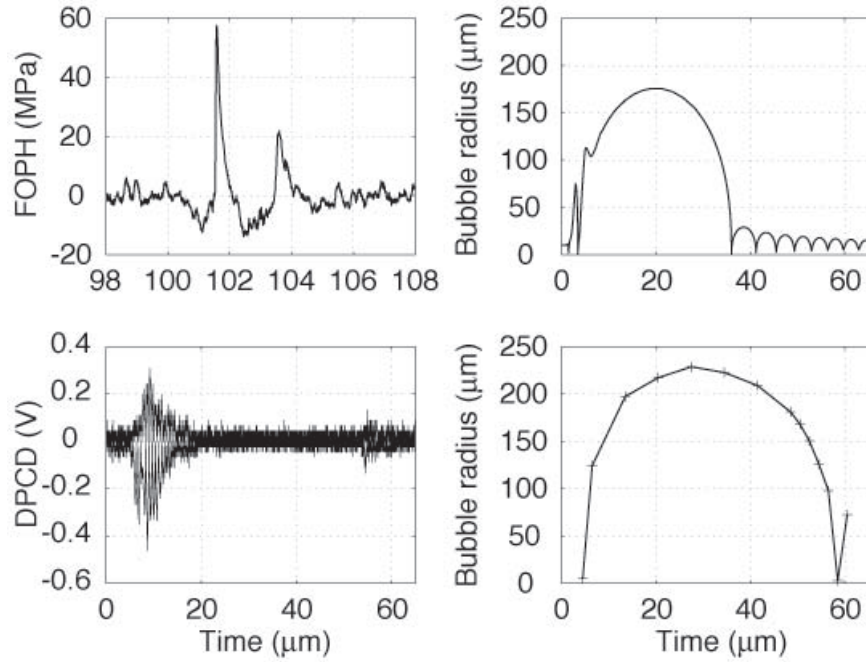
Figure 4.11: Free field cavitation characterization results. The top two frames show the incident SW measured by the FOPH and single bubble dynamics in response to the measured SW predicted by the Gilmore formulation. Measurements acquired using the DPCD and the high speed camera shown in the lower frames.

The lower frames show cavitation measurements acquired using the DPCD and the

high speed camera. An estimate for the characteristic time was determined from the

high speed camera measurements from the time difference between when bubble is first

visible after nucleation till when it collapses, that is the time of the minimum bubble

radius post bubble expansion. The characteristic time recorded by the DPCD was

46 μs and that obtained from the high speed camera measurement was 48 $\mu s \pm 4~\mu s$
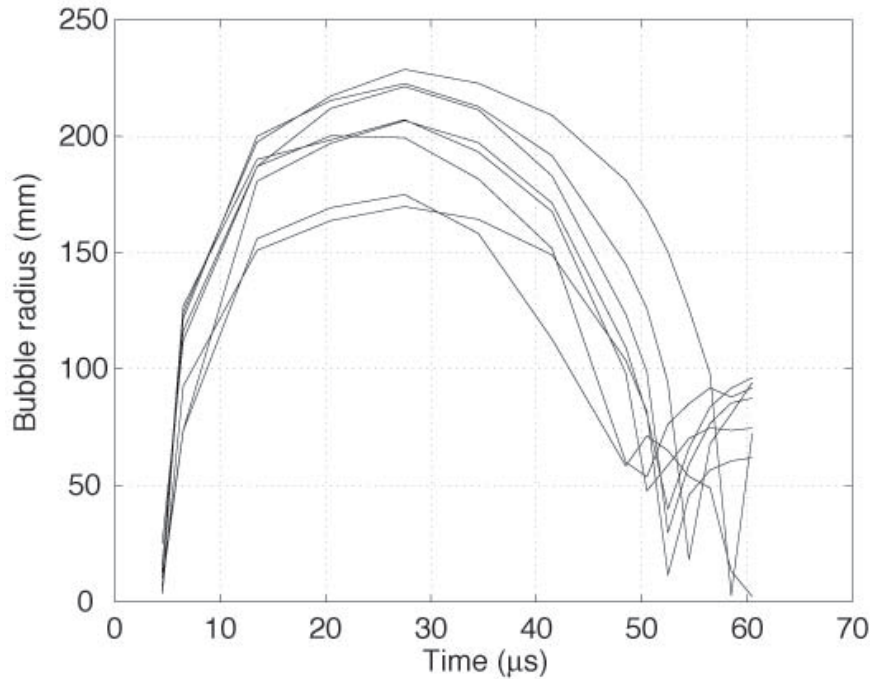
Figure 4.12: Overlay of radius-time profiles (8 runs) obtained from high speed camera images of bubbles in the free field.

(uncertainty associated with time interval between two consecutive frames during nucleation and collapse of the bubble is 4 μs) which were greater than 35 μs predicted by the Gilmore model. The discrepancy between the characteristic times measured obtained by experimental means and Gilmore formulation can be attributed to the inherent assumptions of the numerical calculations, particularly the assumption of "no mass diffusion". Though the Gilmore model under-predicts maximum bubble radius and the characteristic time, the main bubble growth-collapse cycle predicted by the model is qualitatively consistent with the measurements obtained using the high speed camera. The maximum radius was determined to be 229 μm. The radius

98

time profiles for runs obtained from the high speed camera images is shown in Fig. 4.12. Cavitation driven by shock waves produced by the piezoelectric source in the current source (all elements driven synchronously) results in a maximum bubble radius of 204 μm $\pm$ 22 μm and a characteristic time between 45 μs and 55 μs.

4.2.2 Gilmore model

The measured custom waveforms shown in the previous section were used to drive the single bubble dynamics obtained from the Gilmore formulation (details presented in Chapter 2) and the results were contrasted against the bubble response to waveform produced by driving all elements synchronously.

The results of the Gilmore formulation were determined to be relatively independent of initial bubble radius within the range 0.1 μm to 10 μm as shown in Fig 4.13. Four parameters were examined, maximum bubble radius, the characteristic time, radiated pressure from the forced collapse, and the radiated pressure from the inertial collapse. The variability in the four parameters was observed to be 17 %, 15 %, 27 %, and 38 % respectively.

Figure 4.14 shows the results from Gilmore bubble dynamics model for three waveforms: the waveform obtained by driving the elements synchronously, the waveform designed to reduce the negative precursor and the waveform customized for reducing
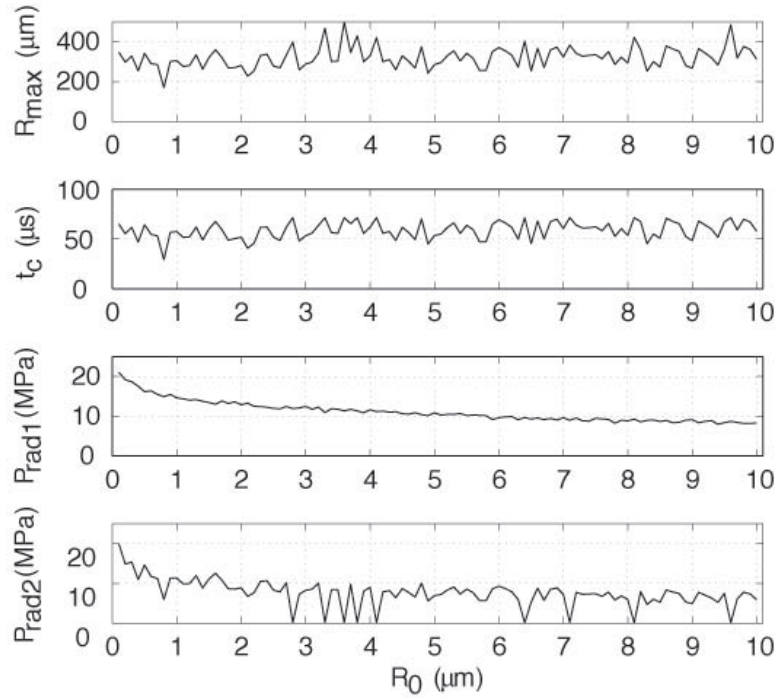
Figure 4.13: Results for Gilmore formulation for bubble dynamics in response to a focal waveform a measured at 1.2 kV for a range of initial bubble radii R_0. R_{max}: maximum bubble radius; t_c: characteristic time; P_{rad1}: predicted radiated pressure from the forced collapse 10 mm from the bubble; P_{rad2}: predicted radiated pressure from the inertial collapse 10 mm from the bubble.

the main tensile phase of the shock wave. In all cases, two collapses were observed, one coincident with the arrival of the lithotripter shock pulse and other, $10-60$ μs later, was induced by the inertial collapse of the bubble. The presence of a tensile phase prior to the main shock front strengthened the first forced collapse which was always predicted to be stronger than the inertial collapse. The weak inertial collapses were attributed to the presence of a second compressive phase following the main tensile phase which inhibited the bubble growth characteristic of lithotripsy induced

100

cavitation.

(a) No delay (ND)   (b) Reduce P_1- (NP)   (c) Reduce P_2- (NC)
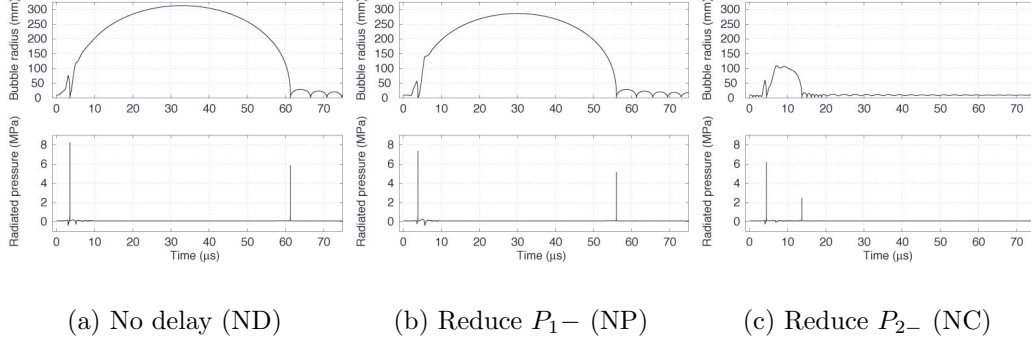
Figure 4.14: Predicted response of a 10 μm bubble to a no delay focal waveform and waveforms designed to manipulate the tensile phases of the shock wave. The Gilmore model predicted a significant reduction in cavitation strength for the waveform designed to reduce the main tensile phase while modifying the precursor reflected a modest variation in the predicted bubble response.

The shock wave produced by driving the elements synchronously resulted in a predicted $R_{max} = 300$ μs with a characteristic time $t_c \simeq 55$ μs. This value of predicted t_c is nearly double the predicted value reported in the previous section. The discrepancy in predicted t_c is due to the fact that the SW measurements in the previous section were acquired using a FOPH and the SW measurements used in this section were acquired using the UW-PVDF hydrophone, which is known to be more effective in accurately capturing the negative phase of the SW. The radiated pressure at 10 mm from the bubble from the forced and inertial collapses were predicted to be 8 MPa and 6 MPa respectively.

The waveform with the reduced precursor resulted in a modest decrease in the predicted cavitation strength i.e., t_c was 5 μs shorter and the radiated pressures were

1 MPa smaller in magnitude. In contrast, reduction in the main tensile phase of the shock wave resulted in a 66 % decrease in R_{max}, an 80 % reduction in the characteristic time, and a 65 % reduction in the radiated pressure from the inertial collapse. The simulations indicate that if fragmentation changes with change in waveform shape then it is likely due to the inertial collapse. The predicted P_{rad1} from the forced collapse did not change significantly with change in waveform shape though it should be noted that the shock wave is small compared to the bubble size.

The values shown in Fig. 4.14 were uncharacteristic of those obtained using SWs from clinical lithotripters, for example, a SW generated by a clinical EHL (Litho-DIamond, Healthtronics, Kennesaw, GA) resulted in the followiing predicted values: $R_{max} = 850$ μs, $t_c = 159$ μs, $P_{rad1} = 27$ MPa, and $P_{rad2} = 49$ MPa.

4.2.3 Cavitation control

Cavitation on the proximal surface of the stone was characterized by the passive cavitation detector (PCD) "listening"using a single transducer focused on the proximal surface of the stones (see Chapter 2). Figure 4.15 shows a typical waveform received by the PCD. The signal at t = 0 μs corresponds to the arrival of shock wave at the stone surface and contains content from the scattered shock wave and the acoustic emissions from forced bubble collapses. The acoustic emission corresponding to the inertial bubble collapse was detected at t = 162 μs. This time is the characteristic

time (t_c) and the amplitude of this signal (P_{rad2}) is related to the magnitude of radiated pressure. The measured t_c and P_{rad2} were used to investigate the extent of cavitation control and its effect on the stone for the customized waveforms (NP and NC). Cavitation induced by the NP and the NC waveforms were compared to cavitation induced by the ND waveform. Measurements were acquired for pulse repetition frequencies of 1 Hz and 0.5 Hz.
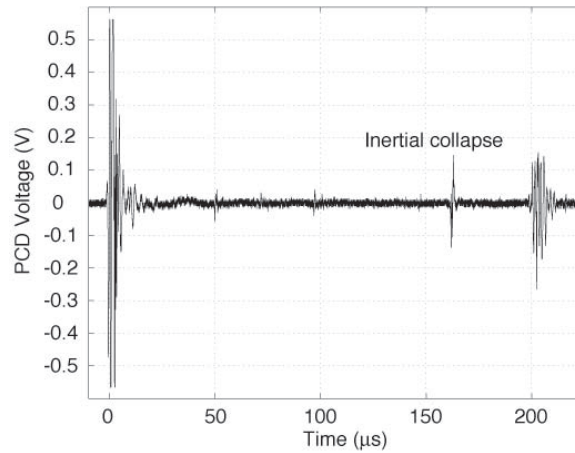
Figure 4.15: Typical waveform received by the PCD.

Figure 4.16 shows the characteristic time (t_c) measured at the proximal surface of the stone using a PCD for the three different waveforms. The ND waveforms administered at a pulse repetition frequency (PRF) of 1 Hz resulted in a $t_c = 159 \pm 4 \ \mu s$ and reducing the PRF to 0.5 Hz a $t_c = 149 \pm 22 \ \mu s$. THe result was not statistically different. The NP waveform $t_c = 126 \pm 4 \ \mu s$ was 20 % lower than for ND at 1 Hz. Similar to the case of the ND waveforms, no statistically relevant difference in t_c
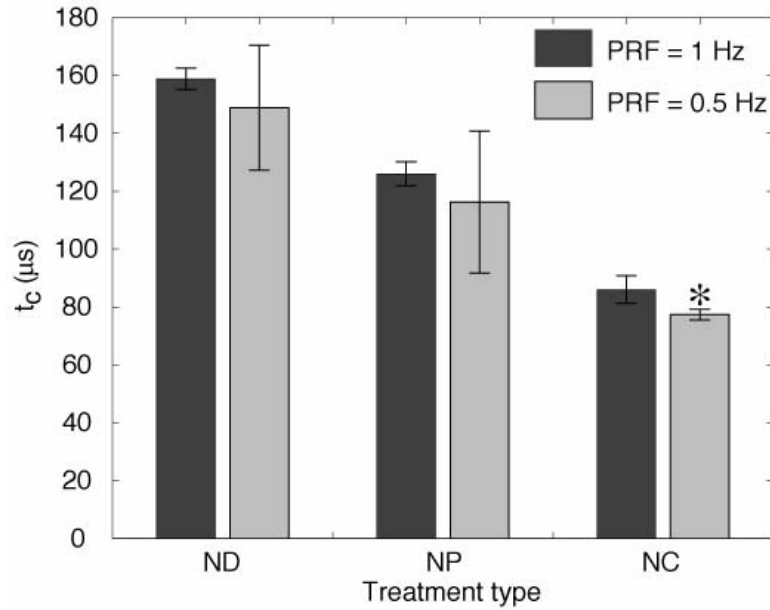
Figure 4.16: Characteristic time measured at the proximal surface of the stone (20 measurements) using a PCD for three waveforms: No delay (ND); reduced negative precursor (NP); reduced main tensile phase (NC). Measurements were acquired at a PRF of 0.5 Hz and 1 Hz. "∗"represents statistically significant difference between measurements for a particular waveform for the two PRFs. All measurements were acquired while the piezoelectric lithotripter array was driven at 1.2 kV

was observed between NP pulses fired at 1 Hz and 0.5 Hz. For NC waveform $t_c = 86 \pm 5$ μs which was about half that of the ND waveform at 1 Hz. This dramatic decrease in t_c for the NC waveform is consistent with the predictions obtained using the Gilmore formulation. A small but statistically relevant difference was observed between t_c for NC at 1 Hz and 0.5 Hz.

Figure 4.17 shows the amplitude of acoustic emission from the inertial bubble collapse (P_{rad2}) at the proximal surface of the stone as measured by the PCD for the three waveform. The acoustic emission resulting from the ND waveform at a PRF
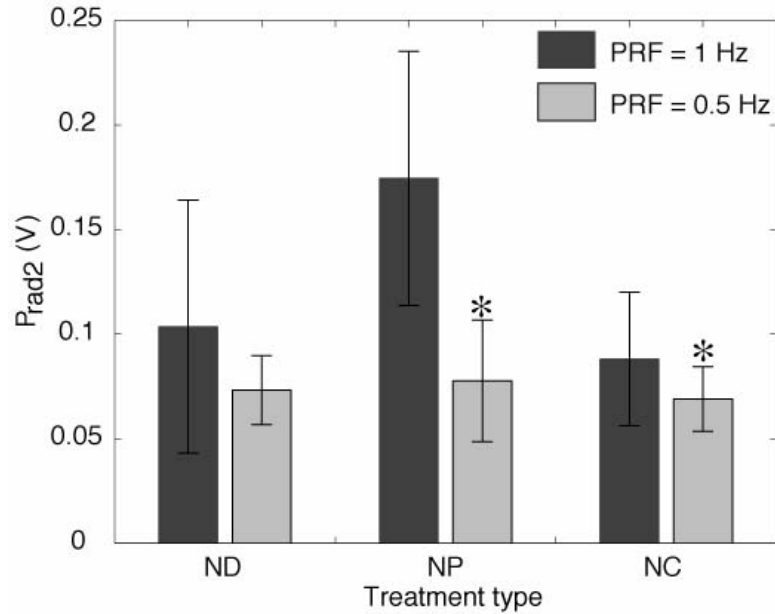
Figure 4.17: Acoustic emission from the inertial bubble collapse (P_{rad2}) measured at the proximal surface of the stone using a PCD for three waveforms: No delay (ND); reduced negative precursor (NP); reduced main tensile phase (NC). Measurements were acquired at a PRF of 0.5 Hz and 1 Hz. "∗"represents statistically significant difference between measurements for a particular waveform for the two PRFs.

of 1 Hz corresponded to a signal of 104 mV ± 61 mV. No statistically significant difference was observed in the acoustic emissions resulting from the ND waveform between 1 Hz and 0.5 Hz. At a PRF of 1 Hz, the waveform with the reduced negative precursor (NP) produced a P_{rad2} signal (175 ± 60 mV) 6 % larger than that of the ND waveform. However, at a PRF of 0.5 Hz, the magnitude of emissions induced by the NP waveform was reduced to 78 ± 29 mV, similar to that of the ND waveforms. The NC waveform resulted in a $P_{rad2} = 88 \pm 32$ mV at 1 Hz PRF and reducing the PRF produced an acoustic emission similar to that of ND and NP (70 ± 16 mV).

The P_{rad2} measurements are consistent with the Gilmore predictions that the NC waveform produces lowest magnitudes of inertial collapse emissions.

(a) Comparison of t_c (b) Comparison of P_{rad2}
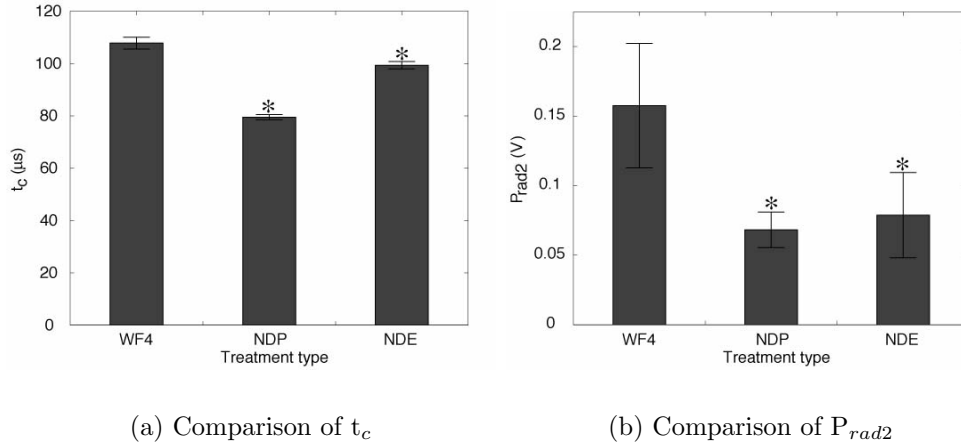
Figure 4.18: Cavitation measured at the proximal surface of the stone using a PCD for three acoustic fields: wide focus with -6 dB width of 4 mm (WF4); driving elements synchronously at 575 V (NDP) to produce the same focal P_{1+} as WF4; driving elements synchronously at 725 V (NDE) to produce net acoustic energy across the stone surface as WF4. Measurements were acquired at a PRF of 1 Hz. (a) Characteristic time (t_c). (b) Acoustic emission from the inertial bubble collapse. The means of measurements for both the NDP and NDE were statistically different from that of WF4 and thus denoted by '*'.

The dependence of cavitation on focal width was investigated by measuring cavitation on the proximal surface of the stone with the PCD for three acoustic fields: the wide focus with -6 dB width of 4 mm (WF4); the acoustic field obtained by driving elements synchronously at 575 V (NDP) to produce the same focal P_{1+} as WF4 (40 MPa); the acoustic field obtained by driving elements synchronously at 725 V (NDE) to produce net acoustic energy across the stone surface equivalent to that produced by WF4 acoustic field (0.38 mJ). The energy introduced over the stone

area was determined from the pulse intensity integral defined in the IEC standards [46] and the methodology is presented in the appendix. Figure 4.18 (a) shows the comparison of t_c for the three acoustic fields. The WF4 acoustic field resulted in the longest t_c of 108 μs $\pm$ 2 μs. The mean t_c for the NDP waveform (-6 dB focal width 1.7 mm) was 27 % lower than that for the WF4. The difference between the mean t_c for the WF4 and the NDE was 8 %. The NDP and NDE waveforms exhibited a more pronounced difference in the acoustic emission from the signal from the inertial collapse compared to the WF4 acoustic field. The mean magnitude of the acoustic emission signal for the WF4 acoustic field was 158 mV $\pm$ 45 mV. In contrast, the magnitude of acoustic emission signal from the inertial collapse from the NDP and the NDE acoustic fields were 57 % and 50 % lower than that for WF4 respectively. The results indicate that the the ND acoustic field produced cavitation different in strength compared to the WF4 field despite maintaining equivalent P_{rad2} or the net energy.

Since the inherent nature of the ring acoustic field resulted in the reduction of acoustic pressure on the axis, the RF4 acoustic field was expected to produce very little cavitation activity on the proximal surface of the stone. Cavitation produced by the RF4 acoustic field was measured using the PCD and contrasted against measurements acquired for the NC waveform. The RF4 field produced a $t_c = 33$ μs $\pm$ 3 μs compared to 86 μs $\pm$ 5 μs for the NC waveform. The acoustic emission of the inertial

107

(a) Comparison of t$_c$ (b) Comparison of P$_{rad2}$
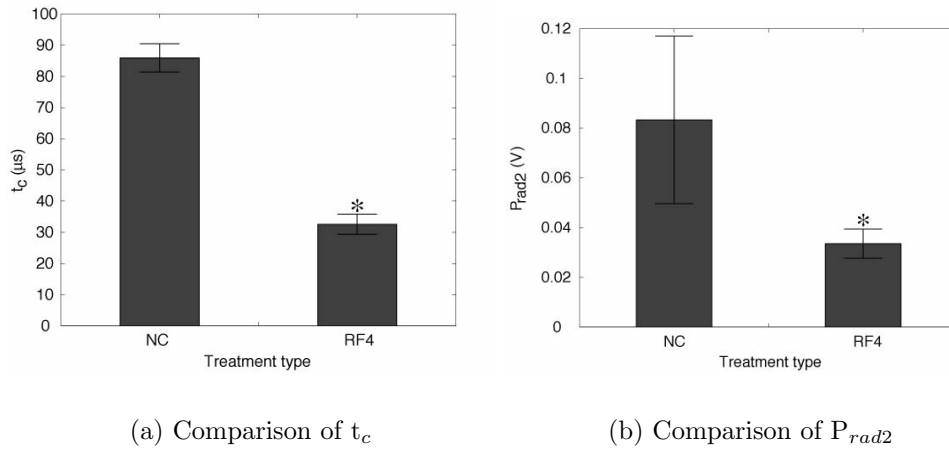
Figure 4.19: Cavitation measured at the proximal surface of the stone using a PCD for two acoustic fields: the waveform designed to reduce the main negative phase of the shock wave (NC); Ring focus of diameter 4 mm (RF4); Measurements were acquired at a PRF of 1 Hz. (a) Characteristic time (t$_c$). (b) Acoustic emission from the inertial bubble collapse. The means of measurements for RF4 were statistically different from that of NC and thus denoted by '*'.

collapse (P_{rad2}) resulted in a PCD voltage of 83 mV $\pm$ 34 mV for the RF4 field and 34 mV $\pm$ 6 mV for the NC waveform. The data showed that the cavitation generated by the RF4 waveform was dramatically less than the NC waveform, which itself had reduced cavitation. The RF4 field should therefore produce little spall or cavitation activity.

The measured t$_c$ and P$_{rad2}$ showed a decrease in cavitation activity with a decrease in the PRF, that is, at low PRF inertial cavitation was less violent. notable result was that at 1 Hz t$_c$ for the NP waveform was less than that of the ND waveform (indicative of weaker inertial collapse), but the acoustic emission, P_{rad2} for NP waveform was 68 % higher than that of the ND waveform. This indicates a shielding phenomenon which

108

will be elaborated upon in the following sections. The cavitation produced from the WF4 (-6 dB focal width of 4 mm) acoustic field was significantly higher than either the NDP acoustic field (same P_{1+}) or the NDE acoustic field (same incident energy). The RF4 acoustic field produced the least cavitation of all acoustic fields which is consistent with the low pressure amplitude on the axis.

4.3   Stone Fragmentation

The fragmentation efficacy of different spatial pressure distributions and waveform shapes were compared and contrasted by performing stone fragmentation studies. Stone fragmentation was quantified by either measuring the mass of stone remaining in the holder or determining the tensile strength of the stones after administering shock waves to the stones (see Chapter 2 for details). The mass measurements were used to primarily quantify cavitation related damage. In a limited number of cases, stones fragmented into two pieces and the separated front end was no longer exposed to the incident shock waves. In such an event, both fragments were weighed post-treatment to obtain an estimate of mass-loss induced predominantly by cavitation (cavitation associated damage occurs primarily as surface erosion and pitting leading to fine debris [55][30][92]). The tensile strength was used to quantify stress related fragmentation effects.

Five main acoustic fields were investigated: the typical acoustic field generated without any inter-element delay (ND), the waveform with reduced negative precursor (NP), the waveform with reduced main tensile phase (NC), an acoustic field with a wide focus "WF4" (a -6 dB width based on P_{1+} of 4 mm which is more than twice that of ND (1.7 mm) and larger than the stone dimension of 3 mm), and a spatial pressure distribution customized to produce a ring (RF4) of high pressure of diameter 4 mm on the periphery of the stone. Results were compared to measurements acquired from untreated (UT) stones. Ten stones were administered with shock waves for each treatment condition. The stones employed in the mass study were administered with 400 shock waves while those for the tensile strength measurements were administered 200 shock waves to restrict surface erosion to minimum in order to facilitate the tensile test and to obtain a more reproducible results.

4.3.1 Stone mass test

Different acoustic fields were first compared by driving the transducer array at 1.2 kV for each case at a pulse repetition frequency of 1 Hz. Figure 4.20 shows the mass of stone remaining after treatment. The average mass of an untreated stone was determined to be 46 mg. All waveforms and pressure distributions resulted in a mean post-treatment mass that was statistically different (denoted by '*') from the mean mass of the untreated stone. The mean post-treatment mass for all acoustic fields

statistically different from mean ND mass are denoted by 'Δ'. The stones treated with ND resulted in least remaining stone mass of 23 mg. Inhibiting cavitation by reducing either the negative precursor or the main tensile phase of the waveform resulted in an increase in post-treatment mass implying a decrease in fragmentation. Recall that the Gilmore model predicted that reducing the main negative tensile phase should have the most profound effect on cavitation aided stone fragmentation. Further, the PCD measurements (see Figs. 4.16 and 4.17) also indicated that the NC waveforms produced weaker cavitation than both ND and NP waveforms, and indeed the NC waveform had a higher post-treatment mass of 40 mg compared to ND and NP waveforms which implied poorest cavitation induced fragmentation performance of the three waveforms. However, the data indicates that the precursor may also contribute to cavitation induced stone fragmentation and the maximum reduction in mass-loss occurs when both are present. The stones treated with the WF4 acoustic field demonstrated better fragmentation with post-treatment mass of 27 mg. The RF4 stones had post-treatment mass of 38 mg which is modestly better than the NC stones. The cavitation associated stone comminution for the RF4 acoustic field is not consistent with the corresponding PCD measurements that indicate that the cavitation produced by the RF4 acoustic field is the weakest of all the fields.

The role of focal width was further investigated by administering stones with waveforms produced by driving the array at 575 V (NDP) to match the focal P_{1+} of the
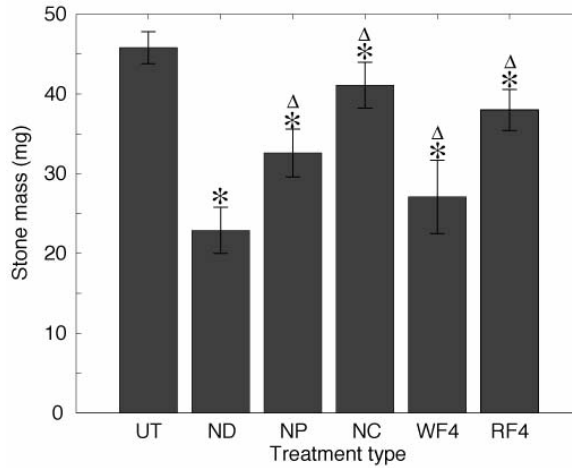
Figure 4.20: Post-treatment mass for different acoustic fields compared with the mass of untreated stones. The mass-test indicated strong dependence of stone fragmentation on cavitation particularly that induced by the main tensile phase of the waveform. Most effective treatment or least remaining stone mass post treatment was observed for the case of the ND acoustic field. Mean post-treatment mass statistically different from the mean UT mass and the mean ND mass are denoted by '∗' and 'Δ' respectively.

WF4 acoustic field or by driving the array at 725 V (NDE) to produce the net energy across the stone area equivalent to that of the WF4 acoustic field. The fragmentation results for the WF4 study are shown in Fig. 4.21. The post-treatment mass resulting from the NDP and the NDE acoustic fields were dramatically higher than that for the ND acoustic field (see Fig. 4.20) which is consistent with the PCD measurements presented in the precious section. The untreated stones in this sample set had a mean mass of 49 mg. Post-treatment mass of NDP and NDE treated stones were only moderately lower than the untreated stones. However, the stones treated with the WF4 acoustic field had a post-treatment mass that was 53 % of the UT mass. At first glance lower post-treatment stone mass for WF4 might lead to the
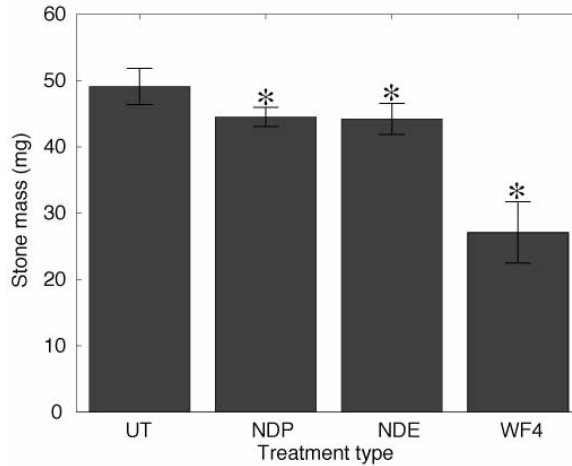
Figure 4.21: Post-treatment mass of stone after treating with the WF4 acoustic field compared to ND treated stones at two driving voltages, one to match P_{1+} of the WF4 focal waveform and other to match the net energy deposited over the stone area by the WF4 acoustic field. Mean post-treatment stone mass statistically different from mean mass of untreated stones were denoted by '$*$'.

conclusion that wider focal fields are more effective in fragmenting stones and that stress related effects such shear which rely on a wide focus are critical. However, PCD measurements acquired for the WF4 acoustic field (see Fig 4.18) indicated that the WF4 acoustic field produced more cavitation than both the NDP and the NDE acoustic fields. Furthermore, the -6 dB region based on P_{2-} and the magnitude of P_{2-} for the WF4 acoustic field were 7 mm and 14 MPa respectively compared to that for NDP were 5 mm and 11 MPa. Thus, the WF4 acoustic field produces conditions more conducive to cavitation related fragmentation than the NDP and NDE acoustic fields. Lastly, in qualitative terms none of the acoustic fields produced fragmentation modes (cleaving) characteristic of stress induced effects such as spallation or shear.
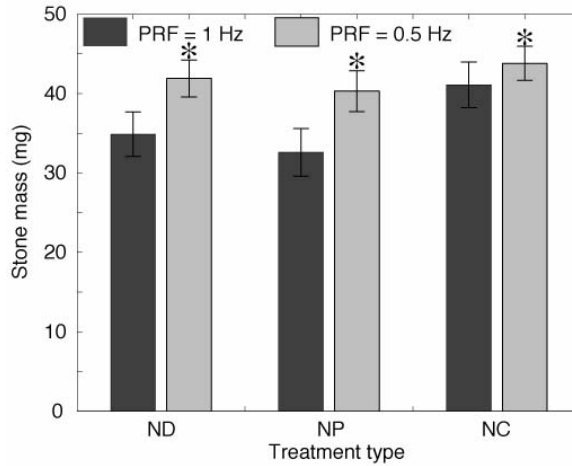
Figure 4.22: Post-treatment mass of stones treated with ND, NP, and NC shock waves at pulse repetition frequencies of 0.5 Hz and 1 Hz. The results illustrate a decrease in fragmentation with a decrease in pulse repetition frequency indicating that the mass reduction is predominantly a cavitation induced effect. The driving voltage for ND was adjusted so as to match the P_{1+} of the NC waveform. Post-treatment mass at 0.5 Hz that were statistically different from those at 1 Hz are denoted by '$*$'.

Presence of debris and cavitation nuclei in the free field in front of the stone is known to shield the stone from the incident acoustic energy, in particular the tensile phase of the shock wave and the shielding effect is dependent on PRF [67]. In order to investigate the effect of shielding, stones were treated with typical ND shock waves as well as the waveforms customized to manipulate cavitation (NP and NC) at pulse repetition rates of 0.5 Hz and 1 Hz. The driving voltage for ND was adjusted to 850 V so as to match the focal P_{1+} of the NC waveform. The post-treatment mass results from the shielding study are presented in Fig. 4.22. Post-treatment mass at 0.5 Hz that were statistically different from those at 1 Hz are denoted by '$*$'. The results indicate an overall decrease in stone fragmentation for all three acoustic fields with

114

decrease in pulse repetition frequency which also translates into an overall decrease in the influence of cavitation on the stone at the lower pulse repetition frequency. The decrease in treatment efficacy with decrease in PRF indicates that pre-focal shielding does not hinder cavitation induced stone comminution. The NP waveform at 1 Hz is the most effective which is consistent with the notion that cavitation related fragmentation is dominated by the main tensile phase and more nuclei are available prior to each pulse at a higher pulse repetition frequency. Even though the waveforms administered at the slower pulse repetition frequency were determined to be less effective as quantified by post-treatment mass, indications of stress related effects such as spallation-like cracks and occasional cleaving of the stone were observed creating a need for measuring specifically the stress induced effect on stones.

4.3.2   Tensile strength test

As the post-treatment mass measurements were limited in their ability to quantify stone fragmentation associated only with cavitation, tensile strength of the treated stones was determined for quantifying stress induced fragmentation.

Figure 4.23 shows the results from the tensile strength study for stones treated with each of the acoustic fields at a pulse repetition frequency of 1 Hz and driving voltage of 1.2 kV. The tension required to induce failure in an untreated stones was determined to be 12.5 N. The mean tensile strength of stones statistically different
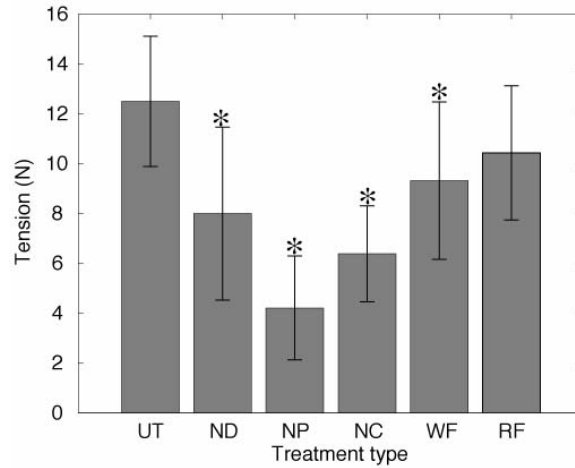
Figure 4.23: Results from tensile test data for stones treated with each of the acoustic fields at a pulse repetition frequency of 1 Hz and a driving voltage of 1.2 kV. The mean tensile strength of stones statistically different from the mean tensile strength of the UT stones are denoted by '∗'.

from the mean tensile strength of the UT stones are denoted by '∗'. The typical ND pulse generated by driving elements synchronously reduced the failure point to about 8 N indicating that the ND waveform does induce some stress related effects weakening the structural integrity of stone. However, the NP waveform (designed to reduce the effects of the negative precursor) further reduces the failure point by a factor of two. The contrast between the tensile strength measurement for the ND and NP waveforms is a strong indication that cavitation in the region in front of the stone aided by the negative precursor might hinder the trailing shock front from inflicting stress related damage on the stone. Recall that the mass measurements indicated that maximum cavitation related damage was inflicted upon the stone when both the negative precursor and the main tensile phase were present, i.e. the ND

116
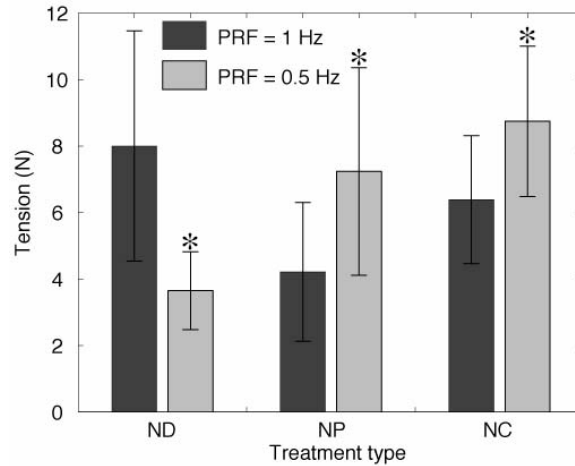
Figure 4.24: Results from tensile test data for stones treated with ND, NP, and NC waveform at a pulse repetition frequency of 1 Hz compared to those treated at 0.5 Hz. All measurements were acquired at a driving voltage of 1.2 kV. Mean tensile strength values determined for the PRF of 0.5 Hz that are statistically different from the corresponding tensile strengths at 1 Hz are denoted by '∗'.

waveform. Furthermore, the PCD measurements indicated that cavitation on the proximal surface of the stone is not inhibited by shielding, which further implies that the difference in tensile strength of the stone for ND waveform and the NP waveform might be due to increased contribution from the positive shock front for the NP waveform. Although the main tensile phase also produces cavitation in the free field in front of the stone, a higher failure point of 6.5 N resulting from the NC waveform indicates that the the main tensile phase is not a dominant contributer to the shielding effect. The WF4 waveforms suffer from cavitation related effects similar to the ND waveforms but has a lower $P_{1+} = 45$ MPa in comparison to the ND waveform at 1.2 kV (65 MPa) therefore subjecting the stone to less stress resulting in stone failure

at over 10 N. The RF4 acoustic field did not produce a statistically different stress compared to the untreated stones. However, the pressures induced around the stone by both the ND and the RF4 acoustic fields were in the range of $15-20$ MPa (see Fig. 4.5).

To further elucidate upon the shielding phenomenon, a tensile strength study was also performed using the ND, NP, and the NC waveforms for pulse repetition frequencies of 1 Hz and 0.5 Hz as shown in Fig. 4.24. Mean tensile strength values determined for the PRF of 0.5 Hz that are statistically different from the corresponding tensile strengths at 1 Hz are denoted by '$*$'. At a pulse repetition frequency of 1 Hz, the ND waveform resulted in stone failure at 8 N. Tension required to induce failure was reduced by more than 50 % when the stones were administered with the ND waveform at a pulse repetition frequency of 0.5 Hz. Higher tension values for NP and NC waveform at 0.5 Hz compared to that of 1 Hz indicates that there might also be some contribution to the stress related damage from secondary acoustic emissions from bubble collapses. However, since the mass measurements indicate that the strongest cavitation is induced by the ND waveform (Fig. 4.20) and that cavitation activity is reduced by decreasing the pulse repetition frequency (Fig. 4.22), the dramatic difference in the failure points for stones treated with the ND waveform at 1 Hz and 0.5 Hz is an indication that the positive phase of the shock wave is the dominant contributer for the stress related effects. Further, the piezoelectric lithotripter system

in the current study could lead to extensive pre-focal shielding due to debris and cavitation in front of the stone, particularly when aided by the negative precursor, thus hindering the positive phase of the shock wave from effectively entering the stone and inducing the stress related effects characteristic of lithotripsy.

4.4 Cavitation Induced Shielding

The shielding phenomenon was investigated using a diagnostic ultrasound system. B-mode images were obtained during the course of the shock wave treatment and the pre-focal volume in front of the stone was probed using the diagnostic ultrasound system. The details of the methodology are presented in Chapter 2. Figure 4.25 shows a B-mode image of the stone. The proximal surface of the stone is placed at the focus. The net shielding is related to the amount of pre-focal debris, which was quantified in terms of the spatial average brightness or echogenecity of the B-mode image of the region of interest.

Figure 4.26 shows B-mode images of the region of interest for two conditions, one with very little debris and other with a significant amount of debris. The images were acquired while administering shock waves at a PRF of 1 Hz. Of the 30 pulses fired, frames corresponding to time-span between the 20th and the 27th pulse were recorded. Higher average brightness was an indicator of more debris particles and
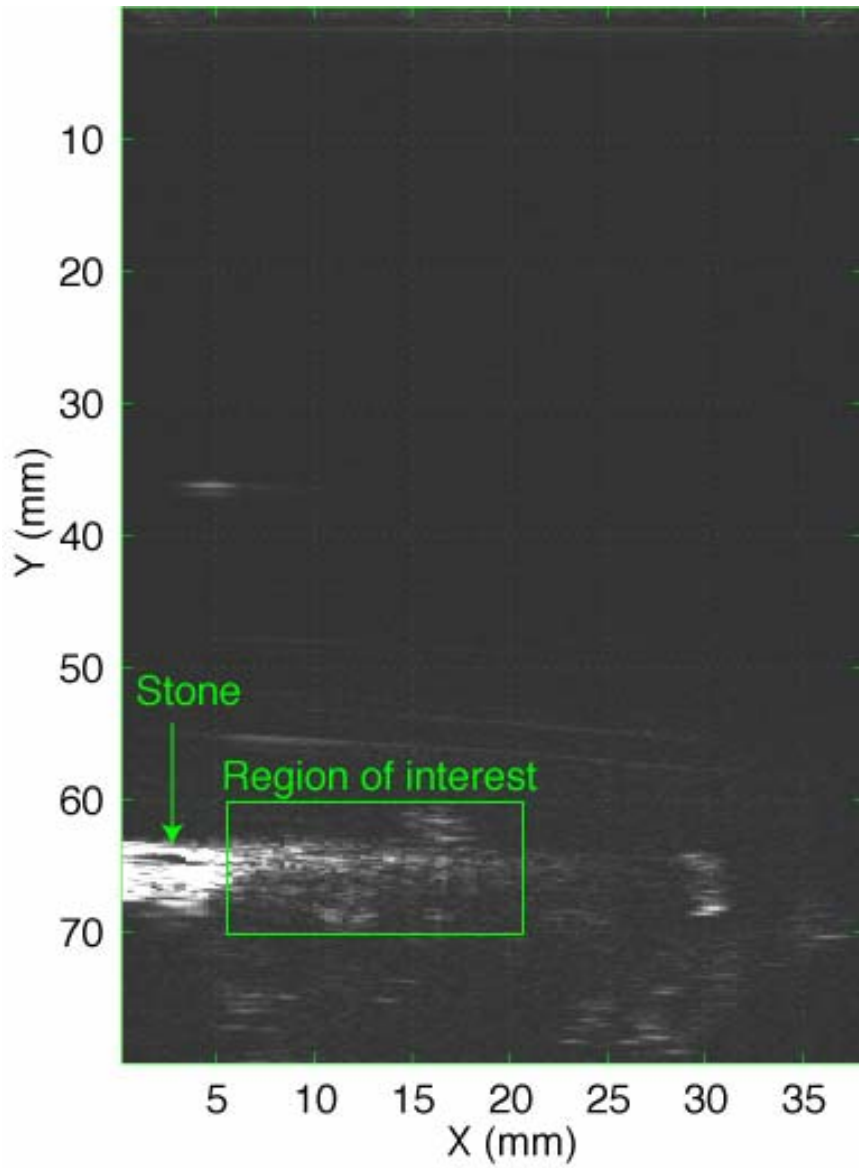
Figure 4.25: B-mode image of the stone acquired during treatment. The proximal surface of the stone is placed at the focus.

(a) Image with less debris   (b) Image with more debris
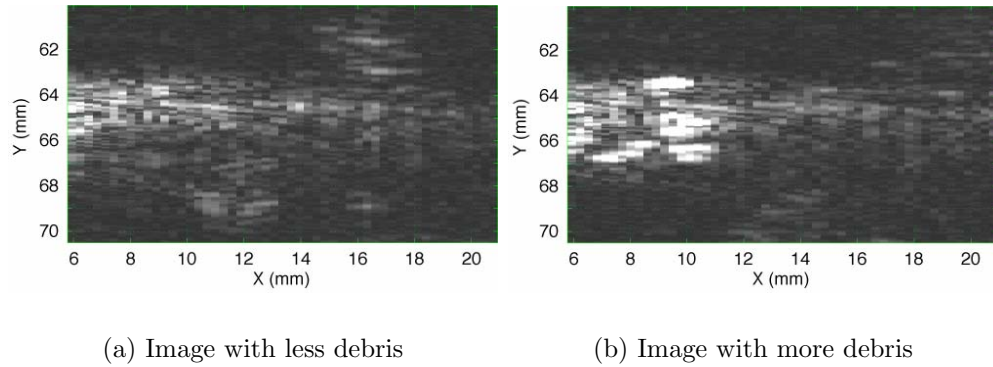
Figure 4.26: The B-mode image of the region of interest for two cases, one with less debris, other with significantly more debris. The brightness relates to the size of a debris particle and amount of gas entrapped in the debris.

more entrapped gases potentially leading to more nucleation sites for shielding. The average brightness between shock waves will be referred to as the baseline. The baseline brightness and the time required for the brightness to settle back to the baseline were used for comparing the amount of pre-focal debris.

Figure 4.27 (a) shows the average B-mode brightness over time for the ND, NC, and NP waveforms at a PRF of 0.5 Hz. The sharp peaks indicate the arrival of the shock wave. The average brightness resulting from the ND waveforms had the highest baseline of approximately 70. The time required for the average brightness to fall back to the baseline was between 25 % and 100 % of the period (t_{PRF} =1/PRF). Similarly, the baseline average brightness for the NC waveform was around 60 and in most cases, the the brightness reached baseline following a shock in 10 % to 20 % of the t_{PRF}. The NP waveforms produced the least amount of debris resulting in
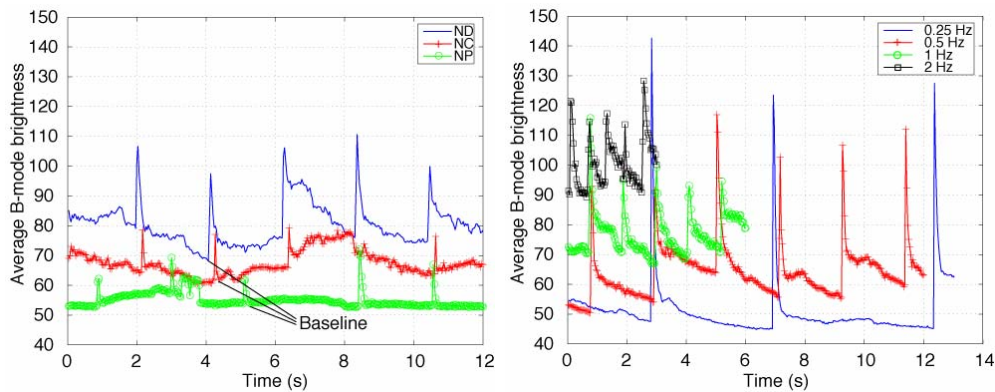
(a) Amount of debris dependent on waveform shape at 1 Hz

(b) Amount of debris dependent on PRF for the ND waveform

Figure 4.27: Amount of debris in front of the stone quantified in terms of the spatially averaged brightness of the B-mode image in the pre-focal region. Sharp peaks indicate the arrival of the shock wave. Amount of debris exhibited a dependence on both waveform shape and PRF. ND waveform had the most pre-focal debris. Amount of debris increased with an increase in PRF.

a baseline average brightness of 52. Following a shock wave, the brightness reached baseline within 10 % of the t_{PRF}. The results from the B-mode brightness indicate that the NP waveform would produce the least amount of pre-focal debris and would lead to least shielding. This result is consistent with the results from the stone mass and tensile strength measurements. It is noteworthy that there appear to be two different time-scales for the decay of the B-mode brightness, faster drop followed by a more gradual decay. The two time-scales might be associated with movement of the debris (fast), and bubble dissolution (slow).

The dependence of pre-focal debris on the PRF is illustrated from the results shown in Fig. 4.27 (b) for the ND waveform. The baseline of average B-mode brightness

increases with an increase in PRF from 45 for 0.25 Hz to about 90 for 2 Hz. The results also indicate that the brightness value does not settle back to the baseline prior to the subsequent shock wave for PRFs of 1 Hz and 2 Hz. The B-mode results for varying PRF's indicate that PRF has a profound effect on the amount pre-focal debris and thus shielding of the stone from the incident shock wave.

Chapter 5

Discussion and Conclusions

The primary goal of this study was to gain insight into the mechanisms of stone fragmentation in shock wave lithotripsy which might lead to improvement in treatment efficacy while reducing the bio-effects associated with lithotripsy. In order to investigate different proposed modes of stone fragmentation, a piezoelectric shock wave source consisting of a spherically focused array with 170 elements each of which could be driven independently, was employed. The piezoelectric lithotripter array was used to customize the acoustic output (spatial pressure distribution and waveform shape) with aim of specifically enhancing or suppressing the effects of specific mechanisms. Despite the ability to customize the acoustic output, the system utilized in this study was determined to be ill-suited for exciting some of the proposed fracture modes when operated at a PRF of 1 Hz , specifically stress induced fragmentation. The implica-

tions of the results discussed in the previous chapter and the conclusions followed by future directions will be presented in the following sections.

5.1   Discussion

The piezoelectric source used in this study was capable of producing peak positive pressures of around 65 MPa with a focal width of around 2 mm when all elements were driven synchronously at the highest driving voltage of 1.2 kV. The peak pressure was well within the range (30 MPa to 110 MPa) produced by clinical lithotripters [25][10][14]. The shock waves induced detectable cavitation in the free field with the characteristic time for bubble collapses ranging between 50 μs and 60 μs. This time was significantly less than measured in clinical lithotripters (between 150 μs and 400 μs) due to the presence of a second shock front with a ~30 MPa peak pressure following the main tensile phase of the incident SW which inhibits bubble growth.

The second positive peak of the waveform (P_{2+}) inhibited cavitation growth resulting in a maximum bubble radius of 200 μm.

Artificial stones (3 mm $\times$ 3 mm $\times$ 5 mm) made of Ultracal-30 (U30) gypsum cement were used for studying stone fragmentation. Previous work with U30 stones exhibited both stress and cavitation induced stone fragmentation for an electromagnetic lithotripter with a high peak pressure (115 MPa) and a narrow focal region

(2.5 mm) and an electrohydraulic lithotripter with a moderate peak positive pressure (35 MPa) and a wide focal region (11 mm). Therefore, the piezoelectric lithotripter array was also expected to induce fragmentation modes associated with both stress and cavitation in these model stones.

In this study, stress related mechanisms were investigated selectively by manipulating the spatial distribution of pressure across the focal plane and cavitation related effects were selectively studied by waveform shaping. Five main acoustic fields were employed: the acoustic field generated by driving all elements synchronously (ND), the acoustic field customized to produce a wide focal region (WF4) such that the -6 dB focal width was 4 mm (more than twice that of ND and larger than the stone dimension of 3 mm), the acoustic field designed to produce a spatial pressure distribution in the shape of a 4 mm diameter ring (RF4) on the periphery of the stone, the waveform with reduced negative precursor (NP), and the waveform with reduced main tensile phase (NC).

5.1.1 Results obtained at PRF of 1 Hz

First results are discussed for experiments carried out at a PRF of 1 Hz which is in the range of clinical treatments. Contributions from specific waveform features will be discussed in terms of damage associated with direct stress and cavitation and compared to the results obtained by customizing the waveform shape and spatial

pressure distribution.

Since spallation depends on the portion of the incident wave that enters the stone and reflects from the distal surface of the stone resulting in large tensile stress, a focal width narrower than the stone dimension was desired for isolating spallation from other stress effects. Since the ND focal width (1.7 mm) was less than the stone diameter of 3 mm, driving all elements synchronously should isolate the effects of spallation from other stress effects. However, the stones exposed to ND acoustic field did not exhibit a crack near the distal surface of the stone or cleaving characteristic of spallation [13][50][70]. Rather, the damage was characteristic of cavitation, with surface pitting and erosion of the proximal and distal surfaces of the stone. The PCD measurements indicated that indeed the ND acoustic field produced the strongest cavitation on the stone surface of all the acoustic fields investigated.

Shear waves are predicted to produce large tensile stresses, particularly when they interact the reflected longitudinal wave in the stone [19]. For a cylindrical stone, effective generation of shear waves depends on the presence of a high amplitude pressure wave passing through the fluid on the sides of the stone. The WF4 acoustic field was designed to ensure generation of shear waves in the stone which should also result in crack formation near the distal end of the stone. Stones treated with the WF4 acoustic field also exhibited cavitation mediated fragmentation without evidence of cracks near the distal surface or cleaving. The amount of erosion was less than

the ND waveform and was consistent with the reduced cavitation measured with the PCD.

The ring acoustic field (RF4) was designed in order to exclude the contribution from spallation to stone comminution and selectively investigate squeezing and shear effects [36] by projecting the highest pressure magnitudes on the periphery of the stone while minimizing the magnitude of the pressure wave entering the stone. Since no constraints were applied to the arrival times of the pulses, some portions of the ring were delayed in time potentially rendering the RF4 acoustic field less effective in producing the desired stress effects. The peak positive pressures generated in the fluid outside of the stone by the RF4 acoustic field were between $15-22$ MPa which were larger than the ND acoustic field (12 MPa at X $= \pm$ 1.5 mm) but lower than the WF4 acoustic field (25 MPa at X $= \pm$ 1.5 mm). The RF4 acoustic field did not result in visible cracks or cleaving associated with stress induced fragmentation. However, a modest decrease in post-treatment mass was measured for the RF4 stones consistent with PCD measurements showing a weak cavitation field. The lack of a coherent wavefront passing on the periphery of the stone means that this data cannot be used to dismiss the role of squeezing or shear waves.

The lack of stress related damage to the stone for the ND, WF4, and RF4 acoustic outputs could be attributed to the fact that the negative precursor in the ND waveform induced cavitation bubbles that shielded the stone from direct stress. This

is supported by data at 1 Hz which showed almost exclusively cavitation erosion to the stones despite a peak positive pressures and a spatial pressure distribution that would typically induce strong spallation/shear effects. Further, modifying the spatial pressure distribution did not change the stress associated fragmentation but rather was consistent with the measured cavitation for the respective fields. Furthermore, the stones treated with the ND waveforms did not exhibit a significant difference in measured tensile strength when compared to the untreated stones. However, stones treated with the NP waveform (which might have reduced the shielding effect induced by the precursor) had a much lower tensile strength at about 50 % that of the ND waveforms.

Although the ND, WF4, and RF4 acoustic fields did not produce visible cracks or cleaving associated with stress, measurable cavitation mediated surface erosion (post-treatment mass measurements) was observed for all three cases. The role of cavitation in stone comminution for the piezoelectric lithotripter array was further investigated by means of waveform shaping. The ND waveform can lead to two types of cavitation events: bubble growth induced by the negative precursor (0.5 μs in duration and P_{1-} =-10 MPa, see Fig. 2.5) followed by forced collapse due to trailing positive shock front, and bubble growth induced by the main negative phase (1.5 μs in duration and P_{2-} =-15 MPa, see Fig. 2.5) and subsequent inertial collapse.

Two waveforms were designed to isolate and distinguish between the cavitation

events and their contribution to stone comminution. The first waveform (NP) had a reduced negative precursor thus reducing the 'strength'of the forced collapse while retaining the inertial collapse comparable to that from the ND waveform. The second waveform (NC) was designed to reduce the main negative phase of the shock wave resulting in an inertial collapse weaker than that induced by the ND waveform while not affecting the forced collapse.

Changes in cavitation activity for the two customized waveforms were predicted using the Gilmore formulation for single bubble dynamics and confirmed using passive cavitation detector (PCD) measurements acquired at the proximal surface of the stone. The characteristic time t_c for the NP waveform was 80 % of that resulting from the ND waveform indicating relatively similar inertial cavitation but NC waveform resulted in a t_c that was 54 % of the t_c for the ND waveform (see Fig. 4.16).

The effect of waveform shaping on cavitation was also reflected in the post-treatment mass measurements which indicated that the fragmentation of the NP waveform was 40 % less than the ND waveform and the NC waveform was 79 % less than the NP waveform. Although measured t_c appears to correlate well with the post-treatment mass measurements, the radiated pressure from the inertial collapse (P_{rad2}) did not correlate well with the mass loss and was not consistent with predictions of the bubble dynamics model. These data indicate that t_c maybe a better metric by which to evaluate cavitation strength in lithotripsy.

When the SW delivery rate was reduced to 0.5 Hz, the shielding effects were strongly reduced which subsequently resulted in an increase of stress associated damage to the stones. The details of this study and its implications are described in the next subsection.

5.1.2 Results obtained at PRF of 0.5 Hz

The fragmentation of stones treated with shock waves at 0.5 Hz was dramatically different than the results at 1 Hz. In particular, many stones exhibited a spall-like fracture especially when treated with the ND and NP waveforms. Furthermore, the cavitation mediated surface erosion decreased with decrease in PRF for all three waveforms (see Fig. 4.16). Since the dissolution time of bubbles ranging from 100 μm to 1 mm can be on order of seconds [44], the rate effect is indicative of a phenomenon depending on the bubble population of the fluid when the shock wave is incident. Pishchalnikov et al. [67] have reported that fragmentation efficacy improves with decrease in PRF in both an electrohydraulic and an electromagnetic lithotripter. Pishchalnikov's results indicated that the negative phase of the shock waves was reduced at higher PRF's, particularly for fluid with higher gas concentration. The loss of amplitude of the negative phase was demonstrated to be consistent with calculations of the energy required to grow cavitation bubbles in the shock path. The positive phase of the pulse was not affected because of the low void fraction of the

bubbles prior to the arrival of the pulse resulted in minimal scattering. Thus, for a typical lithotripter shock wave, the bubbles in the shock path act like an acoustic diode.

The observations made during this study are consistent the shielding mechanism suggested by Pishchalnikov. However, the specific nature of the waveform generated by the piezoelectric lithotripter array, particularly the negative precursor, complicates the shielding process. The data from this study supports the hypothesis that the negative precursor induces a cavitation bubble cloud on the surface of the stone that shields the stone from the trailing positive peak. The shielding effect is reduced with a decrease in PRF because of the presence of fewer nuclei, and the positive portion of the wave can enter the stone leading to spallation.

We used the conservation of energy approach similar to that of Pishchalnikov's to examine the effect of the negative precursor on the shielding effect. Suppose the fluid preceding the stone contains N bubble nuclei with mean initial radius of 10 μm. Based on the the Gilmore prediction of a single 10 μm bubble to a ND waveform, the bubble growth (prior to the arrival of the main shock front) induced by the negative precursor leads to a bubble radius of about 25 % of the maximum bubble radius (see Fig. 4.14). Based on the measurements of the maximum bubble radius of around 200 μm acquired by the high speed camera, this translates to a bubble size of 50 μm by the time the main shock front reaches the bubbles.

Since the work done against the atmospheric pressure during cavitation bubble growth is two orders of magnitude greater than that against surface tension or viscosity [90], the work required for cavitation growth of a solitary bubble can be approximated as the product of atmospheric pressure and change in bubble volume (for change in radius from 10 to 50 μm) which was determined to be 0.05 μJ. The net acoustic energy (determined from the pressure measurements acquired along the focal plane) corresponding to the negative precursor introduced over the surface area equivalent to that of the U30 stone (3 mm in diameter) was 64 μJ. Pishchalnikov predicted that up to 50 % of the tensile energy was spent in growing cavitation bubbles which translates to 32 μJ of energy being spent to grow bubbles to 50 μm radius. Based on these values, estimated values for N and initial void fraction (radius of 10 μm) prior to the arrival of the SW were determined to be 600 and 3 % respectively. When the bubbles grow to be 50 μm in radius, the predicted void fraction prior to the arrival of the shock front reaches as high 60 %. Although the values presented above do not represent actual quantitative measurements, they present a likely scenario where the shielding of the stress wave is strongly enhanced due to the negative precursor. Since the number of bubble nuclei prior to the arrival of a SW depends largely on the number of residual bubbles from cavitation bubble collapses from the previous SWs, the number of nuclei depends directly on the PRF of incident SWs. In contrast, conventional lithotripters where the waveforms do not have the strong negative precursor

result in a significantly lower void fraction of the bubbles prior to the arrival of the shock front allowing the shock front to enter the stone unhindered. Therefore, the cavitation bubbles present in the fluid preceding the stone will only affect the tensile phase of the SW and cavitation effects while allowing the fragmentation associated with the stress wave.
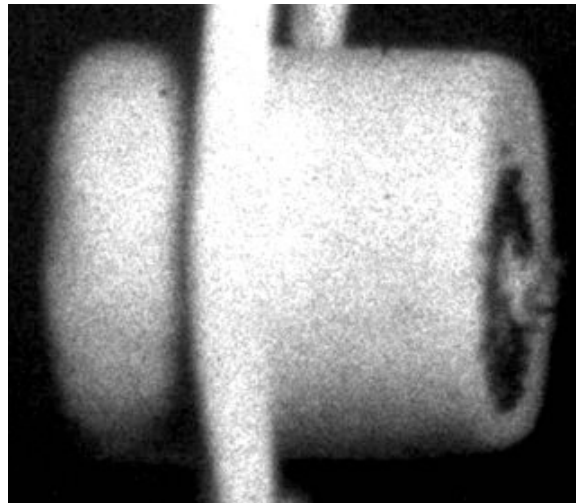
Figure 5.1: High speed camera image of bubbles covering the proximal surface of 6.5 mm diameter U30 stone treated with the ND waveform produced by piezoelectric lithotripter array. The image was acquired at 40 μs after the arrival of shock wave at the stone face and camera was operated at an exposure time of 1 μs.

The presence of shielding was confirmed using B-mode ultrasound imaging of the region in front of the stone. The amount of debris in the fluid in front of the stone was higher at 1 Hz PRF compared to 0.5 Hz PRF. Of the three waveforms, the ND waveform had the most debris. The amount of debris was reduced by either lowering the PRF or using the NP waveform. The debris in the shock path provide nucleation

sites for bubbles to grow. The negative precursor induces bubble growth at these sites that subsequently leads to attenuation of the trailing positive pulse. The shielding of the positive phase is particularly enhanced at the proximal surface of the stone where "pressure doubling" enhances the growth of bubbles and the surface acts as a stable source for cavitation nuclei. The bubbles can grow as a gas layer on the surface as shown in Fig. 5.1.

(a) Transmission loss as function of frequency and gas layer thickness

(b) Frequency dependent transmission loss for 1 μm gas layer
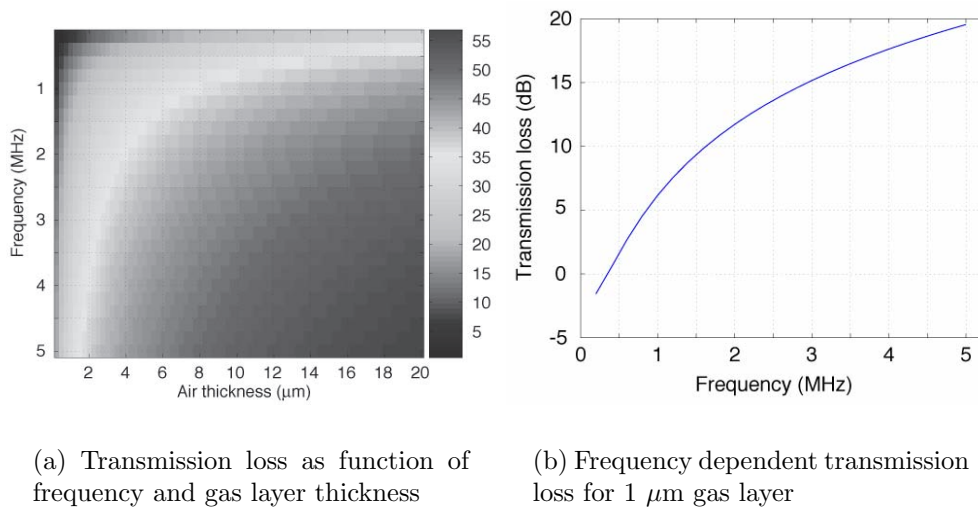
Figure 5.2: Plane wave transmission loss (dB) calculated for a range of frequencies and air film thicknesses. The calculations predict that higher harmonics such as those associated with a shock front, suffer high transmission loss even for thin air films.

The impact of a gas layer on sound propagation was treated to a first approximation by modeling the propagation through a 3 layer medium consisting of water, air, and the stone. The predicted transmission loss [8] as a function frequency and gas layer thickness as shown in Fig. 5.2 (a). The calculations predict that higher harmonics such as those associated with a shock front, suffer high transmission loss for thin air

films thus potentially hindering the stress effects. For instance, a 1 μm gas layer results in a transmission loss of over 30 dB for 5 MHz but only 12 dB for 0.5 MHz. The transmission loss results indicate that a thin gas layer on the proximal surface might severely hinder spallation but allow cavitation to occur on the proximal and distal surfaces of stone.

The PCD measurements were consistent with the transmission loss predictions. Although reducing the PRF from 1 Hz to 0.5 Hz led to a considerable improvement in spallation, t_c for the ND and NP waveforms were not dependent on PRF and only modestly dependent on PRF for the NC waveform. However, post treatment mass measurements indicated a significant reduction in treatment efficacy when PRF was reduced from 1 Hz to 0.5 Hz which indicates changes in cavitation due to changes in PRF might be manifested as change in bubble population or number density at the surface.

5.1.3   Tensile strength study

The shielding of the positive phase due to the negative precursor was further confirmed with the tensile strength measurements of stones treated with the ND, NP, and NC waveforms. The tensile strength of stones treated with ND waveforms reduced by more than 50 % when the PRF was lowered from 1 Hz to 0.5 Hz, which is consistent with the notion of spallation being enhanced at a lower PRF. However, the tensile

strength measurements for the NP and the NC waveforms at 0.5 Hz were not consistent with the PRF trend exhibited by the ND waveform. Since the NC waveform has a precursor similar to the ND waveform, stones treated with the NC waveform at 0.5 Hz were expected fail under tension more readily than those treated at 1 Hz. Further, since the NP waveform inhibits the negative precursor, stones treated with the NP waveform at 0.5 Hz were expected to have tensile strengths similar to those treated at 1 Hz. However, stones treated with either the NP or NC waveforms exhibited an increase in tensile strength with decrease in PRF.

The increase in the tensile strength from 1 Hz to 0.5 Hz for the NP and NC waveforms is a contradiction to the shielding hypothesis. In order to further explore this issue, tensile strength measurements were repeated. The mean tensile strength of the stones treated with the NP waveform at 1 Hz was 6 N $\pm$ 3 N compared to 7 N $\pm$ 2 N for 0.5 Hz. Although the means were statistically different from each other, the measurements indicated that lowering PRF from 1 Hz to 0.5 Hz had a much lower impact on stress related damage from the NP waveforms than the ND waveforms. The tensile strength for the stones treated with NC waveforms at 0.5 Hz was determined to be 7 N $\pm$ 3 N which is reasonable as at the lower PRF, both waveforms would suffer less from shielding. The tensile strengths measured from the stones treated with NP and NC waveforms are higher than that of stones treated with ND waveforms at 0.5 Hz, which is expected since the peak positive pressure for

the ND waveforms is higher than NP and NC waveforms. The new data indicates that the shielding hypothesis is a possible explanation for the lack of stress related damage at 1 Hz. However, the data also indicates a need for a more reliable and accurate method for measuring the tensile strength of the treated stones. Further, the sample size of 10 stones for each case is not sufficient and a much larger sample size is necessary for obtaining an accurate measure of direct stress on the stones.

Alternately, the PRF tensile study that contradicts the shielding hypothesis above presents a possibility that the presence of spall-like fractures at the lower rates may not be due to direct stress effects but rather due to enhanced cavitation, particularly if cavitation induced stress waves in the stone lead to fractures [87][45][70] rather than pitting. Cavitation can act on the stone in two ways. One mechanism, micro-jets impacting the surface, which likely are responsible for surface erosion, did not increase with increase in PRF. This was indicated by the fact that the surface erosion which depends directly on micro-jets did not vary with change in PRF. The second mechanism by which cavitation may act upon a stone is though high amplitude secondary acoustic emissions produced from spherical bubble collapses near the stones surface. This can launch stress waves in the stone which can produce spall in a similar manner to the direct wave [45]. However, if spherical bubble collapses were more intense at lower PRF, then the increase in cavitation intensity should have been measured by the PCD as an increase in t_c or increase in P_{rad2} or both. Since the PCD did not

detect an increase in either t_c or P_{rad2}, the nature of cavitation damage did not alter dramatically with change in PRF.

5.2   Conclusion

The piezoelectric lithotripter array and the optimization routine presented in this study enabled customization of both spatial distribution of pressure across the focal plane and the waveform shape. Acoustic customization was utilized to selectively activate different proposed mechanisms of stone fragmentation. Although a linear propagation model was employed to customize an acoustic field with significant non-linear propagation effects, the resulting customized fields were in good agreement with the prescribed acoustic fields. The optimization routine suffered two limitations: amplitude was traded for the desired pressure distribution or waveform shape, and the arrival times of pulses for the ring focus were not uniform and thus did not produce a perfect hoop-stress.

The proposed study of fragmentation mechanisms was confounded by the specific nature of the waveform which had a negative precursor that led to cavitation induced shielding thus preventing the positive shock from entering the stone. The shielding effect was compounded by the presence of debris and bubbles from cavitation erosion on the proximal surface of the stone. Acoustic fields that mitigated shielding and

allowed the direct stress wave to enter the stone induced spall-like fragmentation in addition to the surface erosion, which is consistent with the conclusions presented by Zhu et al. [92]. The issue of pre-focal shielding might be a reason the electrohydraulic lithotripter designed by Bailey et al. [4][5], comprising of a pressure release reflector, might have failed to induce stone comminution. The pressure release reflector results in a shock wave that consists of a leading negative phase followed by a positive pressure spike. Bailey attributed the lack of stone fragmentation to that fact that cavitation initiated by the leading negative portion of the pulse was inhibited by the trailing shock front. However, the results from this study indicate that Bailey's waveform could have been inducing a shielding effect, similar to that produced by the negative precursor of the piezoelectric lithotripter array, that prevented the positive phase from entering the stone.

5.3   Future Directions

The current study can be significantly improved by upgrading the hardware to enable higher peak pressures or independent control of amplitude and time delay for each element for more effective optimization. Given a system with both amplitude and delay control, the optimization routine can be modified so that inversion could be achieved by directly solving Eq. 3.18 for $\mathbf{D}(\omega)$ where the solution will take a form

of $\mathbf{A}e^{i\mathbf{\Delta t}\omega}$. Scaling the output of lth element by A_l and delaying the signal by Δt_l for all elements will then produce the desired acoustic field. Improvement in the system would enable more selective investigation of each mechanisms by providing the ability produce an acoustic field more conducive to excite a specific fracture mode The results from the optimization for the wide focal field indicate that performing the optimization in a single plane may not be sufficient. The optimization routine produced a wide focal field at geometric focus by shifting the acoustic focus along the axis of propagation rather than manipulating the pressure distribution. Performing the optimization on at least three planes including the focal plane will enforce better control of the optimization scheme in manipulating the spatial pressure distribution while maintaining the acoustic focus at the geometric focus.

The results from prior studies indicate that different mechanisms might act synergistically resulting in stone comminution although spallation seems to be the dominant mechanism. Stress effects such as spallation appear to be more effective in the earlier stages of the treatment, and the efficacy of these fragmentation modes might be improved by minimizing cavitation. Once, the stone has broken into larger fragments, the stress effects, particularly spallation, becomes less effective in breaking stones, at which time cavitation becomes a dominant mechanism in further reducing the stone into clinically passable fragments. Therefore, an effective treatment protocol might consist of two stages: first to activate the stress effects and minimize

cavitation; second to enhance cavitation.

However, the results from our work indicate that due to the presence of the negative precursor, the piezoelectric lithotripter array is unable to produce spallation or other stress damage effectively. Therefore, in order to incorporate the treatment protocol described above with the piezoelectric lithotripter array, mitigation of shielding due to the precursor is essential. The results from our work further establishes the dependence of treatment efficacy on the PRF of incident SWs, particularly for those devices that might have waveforms with tensile features that accentuate the shielding of stress wave.

Kidney stones can vary greatly in chemical composition, hardness, shape, and size [72]. Therefore, given sufficient knowledge of dominant fragmentation mechanisms for a specific type of stone, in theory, it might be possible to customize the acoustic characteristics to improve the treatment of that stone and reduce the number of SWs required for fragmentation. A piezoelectric lithotripter design based on our piezoelectric lithotripter array can provide the flexibility and dynamic control to adapt different treatment protocols necessary to each specific case. The internal structure of kidney stones could be determined using medical imaging modalities such as CT and acoustic output modified accordingly. This could be a considerable improvement over the existing lithotripters that are rigid and lack the ability to drastically modify the acoustic output.

The focused array used as the piezoelectric lithotripter could also be used for tracking and monitoring the stone. Instantaneous location of the stone with the respect to lithotripter could be determined by triangulation based on pulse-echo arrival times for any three elements. Further, the echo from the stone could be analyzed to gain information about the stone for potentially monitoring treatment progress.

Knowledge of dominant mechanisms obtained through the current and future work could be applied by selectively enhancing the effects responsible for stone failure and suppressing those effects that do not contribute to comminution thus potentially reducing bio-effects. The current study could also be extended further by examining stones constrained in tissue mimicking phantom to determined the dominant mechanisms in a situation more akin to the *in vivo* case which would also allow a more direct investigation of possible bio-effects resulting from the current piezoelectric lithotripter array. Improving the treatment efficacy and target tracking/monitoring would also lead to a reduction in the SW dosage further reducing bio-effects and risk of complications.

Appendix A

Electronic driving system

The high voltage drivers are assembled into 6 racks, each with 8 boards. Each boards has 4 channels referred A, B, C, and D. Each rack has 32 elements. The triggering for the high voltage pulsar circuits (Gammell Applied Technologies, LLC, Exmore, VA) was achieved using a pulse-pattern generator (81104A, Agilent, Palo Alto, CA). A 78-pin connector cable was used for sending TTL pulses to groups of 32 high voltage pulser circuits. Synchronization with the pulse-pattern generator was accomplished using the clock signal from the second bank of board one (Line 62 of Port 2). The clock signal was fed into the interrupt line (INT − pin 6) on all six boards.

The high voltage power supply (model P02HP30, Acopian, Easton, PA) has a working range of $0-2000$ V but was limited to 1200 V due to the maximum permissible voltage for the IGBTs. The high voltage live and ground are split into 6 lines, each

made of high voltage plastic cable (Digikey, Thief River Falls, MN). Molex connectors were used to connect the high voltage lines to each rack. Two low voltage lines, 24 V and 9 V, were also supplied to each cage.

Appendix B

Optimization

The optimization was performed using the optimization toolbox in Matlab (Release 14, Mathworks, Natick, MA). The optimization function used was "lsqnonlin". The optimization employed the Levenberg-Marquardt method for determining the set of delays that minimizes the error between the modeled and prescribed pressure. The search direction used in this algorithm is a solution of the linear set of equations:

$$\left(\mathbf{J}(x_k)^T \mathbf{J}(x_k) + \lambda_k \mathbf{I}\right) d_k = -\mathbf{J}(x_k)^T \mathbf{\Pi}(x_k), \qquad \text{(B.1)}$$

where $\mathbf{J}$ is the Jacobian of the error function $\mathbf{\Pi}$. The magnitude and direction of the search direction is controlled by a scalar value λ. This method is not immune to local minima, therefore, the effectiveness in obtaining the global minimum depends

on how close the initial guess is to the global minimum. The initial guess for the time delays and the corresponding optimization results for wide focus and ring focus are presented below.

Figures B.1, B.2, and B.3 show the initial guess and optimization results for the delays necessary to produce an acoustic field of a prescribed -6 dB focal width of 3, 4, and 5 mm respectively. Acoustic measurements in Chapter 4 indicate that in all instances, the wider focal widths were obtained by shifting the focus along the acoustic axis. Consequently, the delays assigned to the transducer elements are distributed axis-symmetrically in an annular ring arrangement.

Initial guess for the delay and the optimization results for the ring pressure fields are shown in Figs. B.4 and B.5. The optimization routine is less successful in achieving this complex focal pressure distribution and is likely trapped in a local minimum. Convergence to a true solution obtaining a ring pressure field ought to result in assignment of optimal delays to the transducer elements in an axis-symmetric manner. However, neither the acoustic field produced using the 'optimal 'delays, nor the delay assignment to the elements are axis-symmetric.
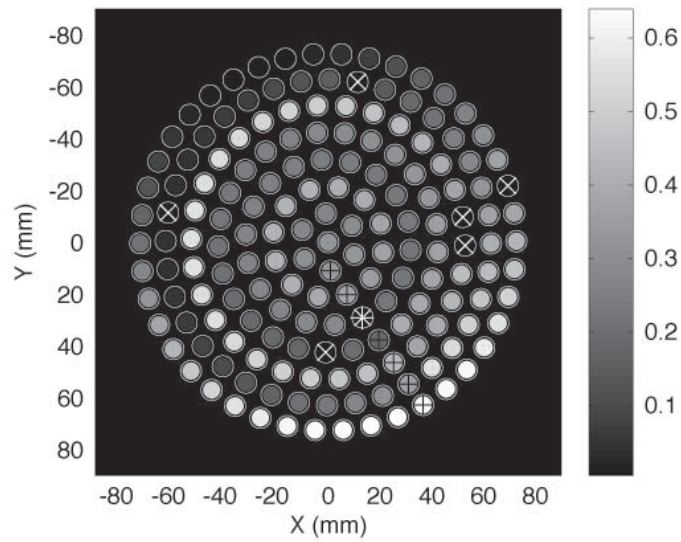
(a) Initial guess for $\Delta t(\mu s)$
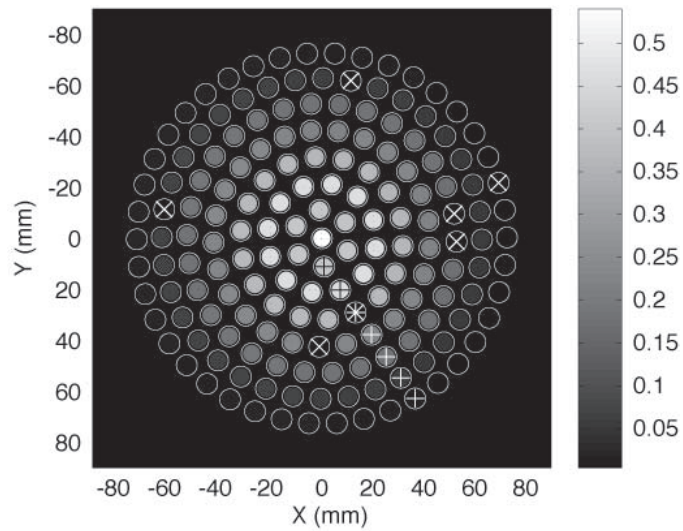
(b) Optmization results for $\Delta t(\mu s)$

Figure B.1: Optimization results for prescribed pressure field with a -6 dB focal width of 3 mm (a) Initial guess for delays(b) Optimal delays obtained using the optimization routine. The delays are plotted on a color-map where each element is represented by a circle and the color-bar represents delay in μs. The non-fuctional transducer elements are marked by a $\times$. The central element is designated as the first element (e_1) and the first element in each subsequent ring is marked by $+$ and the elements are numbered in the clockwise direction.

(a) Initial guess for $\Delta t(\mu s)$

(b) Optmization results for $\Delta t(\mu s)$

Figure B.2: Optimization results for prescribed pressure field with a -6 dB focal width of 4 mm (a) Initial guess for delays(b) Optimal delays obtained using the optimization routine. The delays are plotted on a color-map where each element is represented by a circle and the color-bar represents delay in μs. The non-fuctional transducer elements are marked by a $\times$. The central element is designated as the first element (e_1) and the first element in each subsequent ring is marked by $+$ and the elements are numbered in the clockwise direction.

149

(a) Initial guess for $\Delta t(\mu s)$
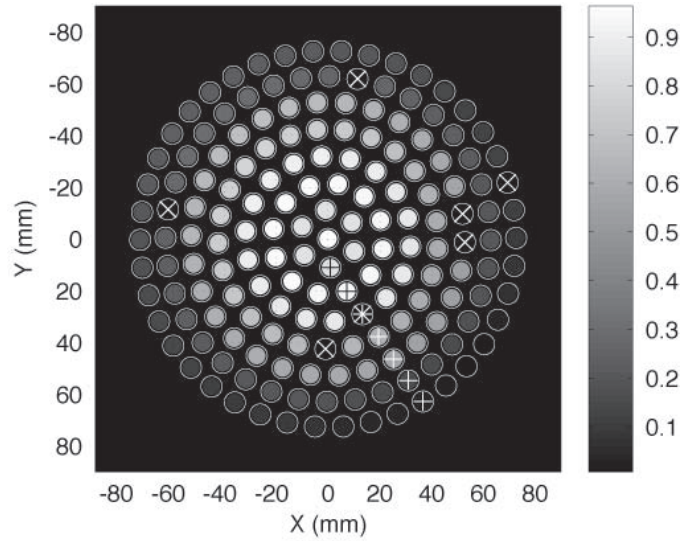
(b) Optmization results for $\Delta t(\mu s)$

Figure B.3: Optimization results for prescribed pressure field with a -6 dB focal width of 5 mm (a) Initial guess for delays(b) Optimal delays obtained using the optimization routine. The delays are plotted on a color-map where each element is represented by a circle and the color-bar represents delay in μs. The non-fuctional transducer elements are marked by a $\times$. The central element is designated as the first element (e_1) and the first element in each subsequent ring is marked by $+$ and the elements are numbered in the clockwise direction.
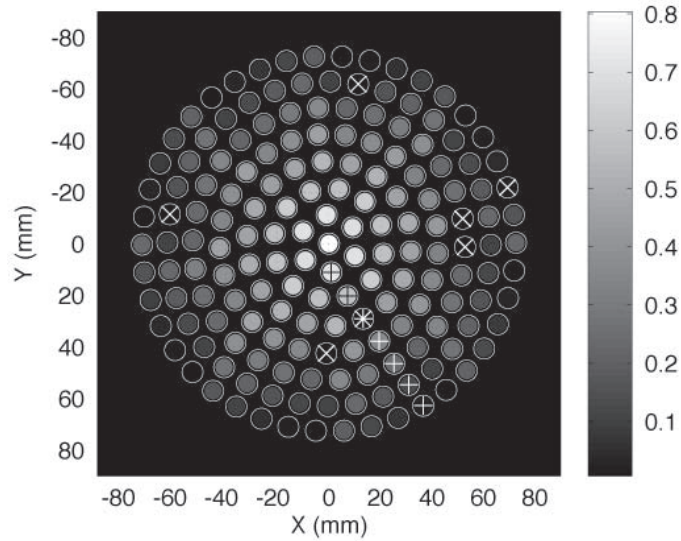
(a) Initial guess for $\Delta t(\mu s)$
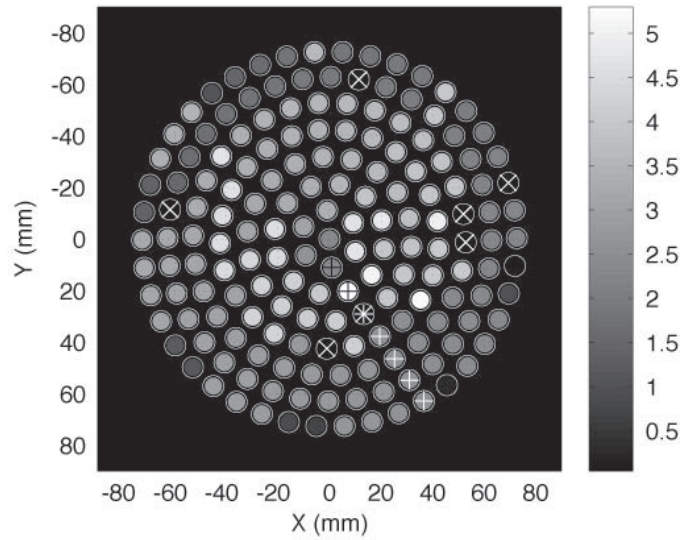
(b) Optmization results for $\Delta t(\mu s)$

Figure B.4: Optimization results for prescribed pressure field with a ring focal field 4 mm in diameter (a) Initial guess for delays(b) Optimal delays obtained using the optimization routine. The delays are plotted on a color-map where each element is represented by a circle and the color-bar represents delay in μs. The non-fuctional transducer elements are marked by a $\times$. The central element is designated as the first element (e_1) and the first element in each subsequent ring is marked by $+$ and the elements are numbered in the clockwise direction.
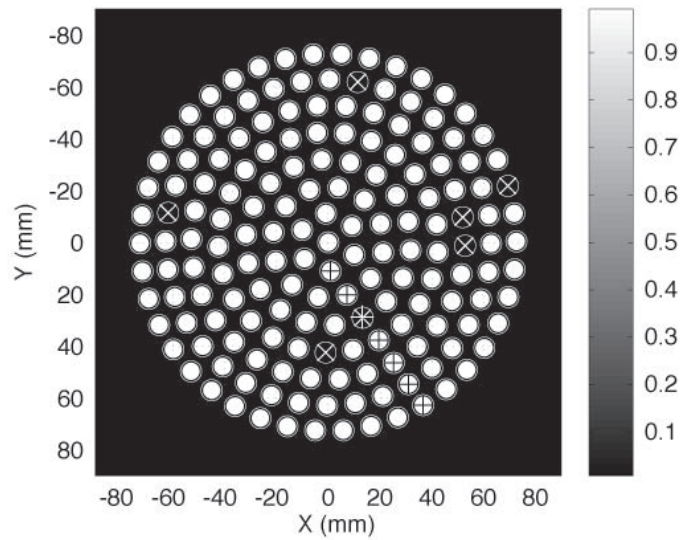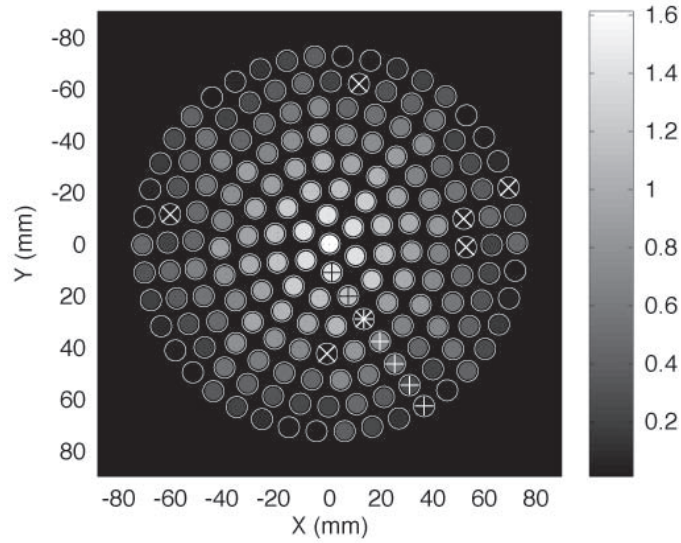
(a) Initial guess for $\Delta t(\mu s)$
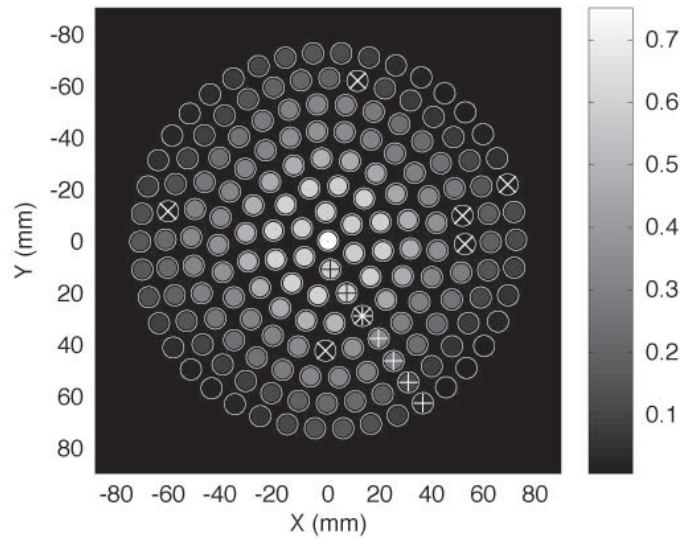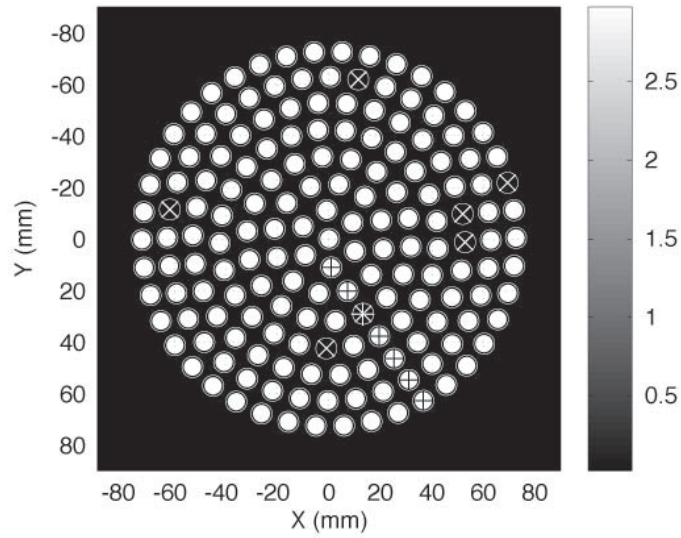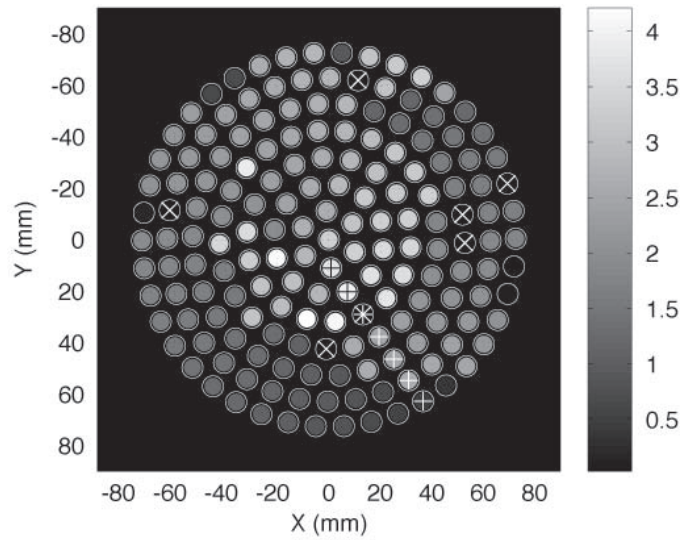

(b) Optmization results for $\Delta t(\mu s)$

Figure B.5: Optimization results for prescribed pressure field with a ring focal field 7 mm in diameter (a) Initial guess for delays(b) Optimal delays obtained using the optimization routine. The delays are plotted on a color-map where each element is represented by a circle and the color-bar represents delay in μs. The non-fuctional transducer elements are marked by a $\times$. The central element is designated as the first element (e_1) and the first element in each subsequent ring is marked by + and the elements are numbered in the clockwise direction.

In order to examine the effectiveness of the "lsqnonlin" in obtaining the optimal delays for achieving the desired pressure field, we investigated the behavior of the error-residual and directional derivative obtained for each iteration during the optimization routine as shown in Figs. B.6, B.7 and B.8. The maximum number of functional evaluations was 32600 and maximum number of iterations was 500. The tolerance for functional evaluation was 0.0001 and the tolerance for Δt_l was 0.001 μs for the wide focus optimization and 0.01 for the ring focus optimization. In all cases, the optimization was terminated when the magnitude of the search direction was less than the tolerance for Δt_l.

(a) Error-residual   (b) Direction derivative

Figure B.6: Optimization results for prescribed pressure field for focal width with -6 dB region of 5 mm. During the course of the optimization, the residue decreases and the derivative approaches zero indicating that the optimization routine is indeed approaching a minimum.

(a) Error-residual   (b) Direction derivative
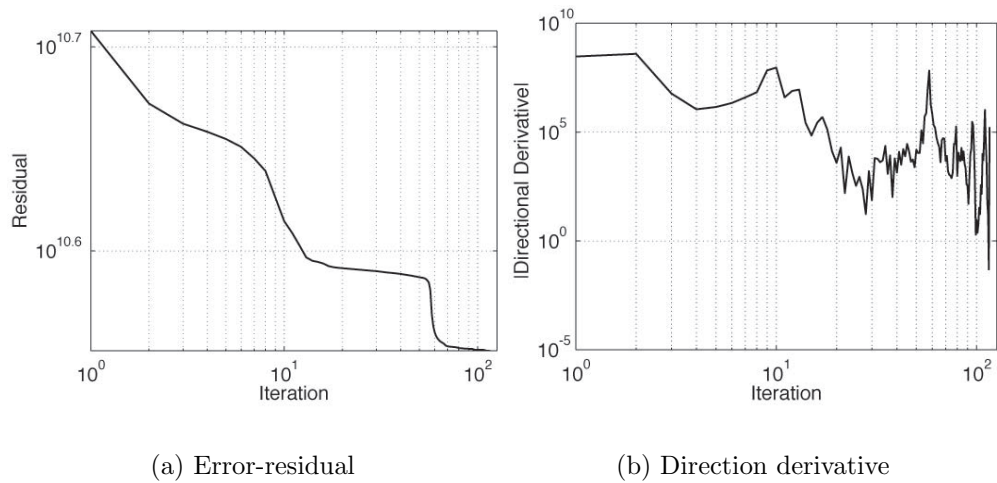
Figure B.7: Optimization results for prescribed pressure field with a ring focal field 4 mm in diameter. During the course of the optimization, the residue and the derivative exhibit a modest decrease indicating that optimization might have encountered a local minimum.

Figure B.6 shows that the optimization routine effectively reduced the residual and the magnitude of directional derivative for the desired pressure field of prescribed -6 dB focal widths. However, the residuals and the directional derivatives did not decrease as effectively for the prescribed fields with a ring pressure distributions (Figs. B.7 and B.8) indicating that the optimization routine might have encountered a local minimum. More sophisticated optimization routines specifically tailored to this problem might be desirable for better results.

(a) Error-residual   (b) Direction derivative
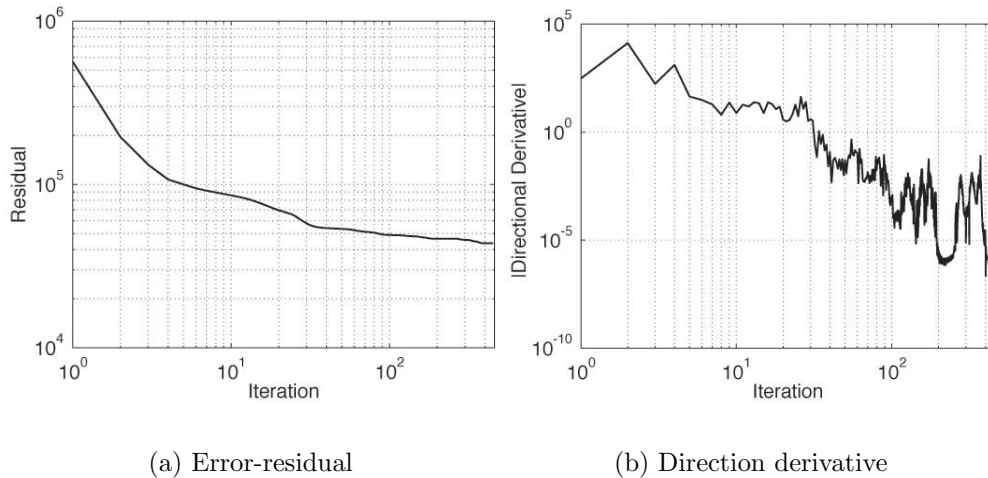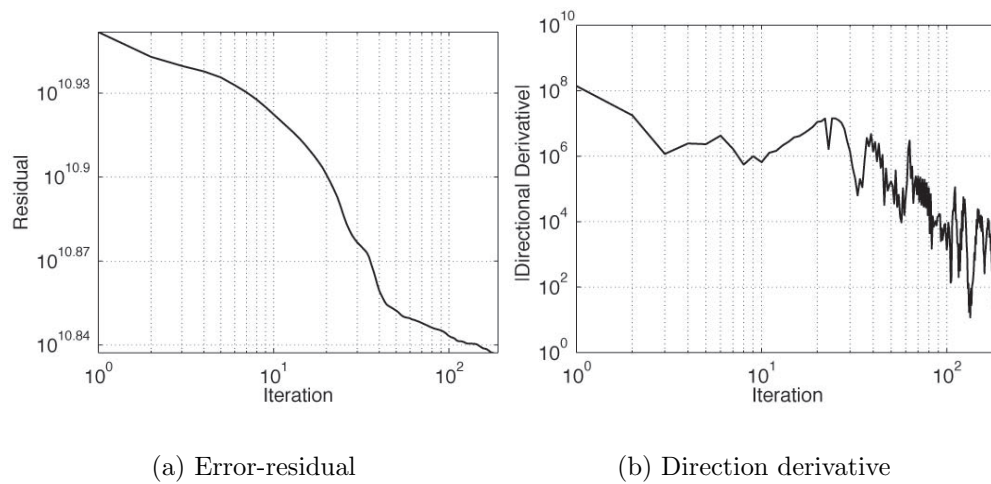
Figure B.8: Optimization results for prescribed pressure field for a ring focal field 4 mm in diameter. During the course of the optimization, the residue and the derivative exhibit a modest decrease indicating that optimization might have encountered a local minimum.

Bibliography

[1] R. Agarwal and V. Singh. A comparative study of fracture strength, ultrasonic properties and chemical constituents of kidney stones. *Ultrasonics*, 29:89–90, 1991.

[2] M. A. Averkiou and R. O. Cleveland. Modeling of an electrohydrualic lithotripter with the KZK equation. *Journal of the Acoustical Society of America*, 106(1):102–112, July 1999.

[3] M. A. Averkiou and L. A. Crum. Cavitation: Its role in stone comminution and renal injury. In James E. Lingeman and Glenn M. Preminger, editors, *New Developments in the Management of Urolithiasis*, pages 21–40. Igaku–Shoin, New York, 1996.

[4] M. R. Bailey, D. T. Blackstock, R. O. Cleveland, and L. A. Crum. Comparison of electrohydraulic lithotripters with rigid and pressure–release ellipsoidal reflectors. i. acoustic fields. *Journal of the Acoustical Society of America*, 104(4):2517–2524, August 1998.

[5] M. R. Bailey, D. T. Blackstock, R. O. Cleveland, and L. A. Crum. Comparison of electrohydraulic lithotripters with rigid and pressure–release ellipsoidal reflectors. ii. cavitation fields. *Journal of the Acoustical Society of America*, 106(2):1149–1160, August 1999.

[6] A. Bierkens, A. Hendrikx, and W. DeKort. Efficacy of second generation lithotripters: a multicenter comparative study of 2206 extracorporeal shock wave lithotripsy treatments with Sienmens Lithostar, Dornier HM4, Wolf Piezolith 2300, Direx Tripter X1, and Breakstone lithotripters. *Journal of Urology*, 148:1052, 1992.

[7] D. Blackstock. *Fundamentals of Physical Acoustics.* New York: John Wiley & Sons, 2000, Ch. 13.

[8] D. Blackstock. *Fundamentals of Physical Acoustics.* New York: John Wiley & Sons, 2000, Ch. 4.

[9] F. Brummer, T. Brauner, and D. F. Usler. Biological effects of shock waves. *Journal of Urology*, 8:224–232, 1990.

[10] A.Buizza, T Dell'Aquila, P. Giribona, and C. Spagno. The performance of different pressure pulse generators for extracorporeal lithotripsy: A comparison based on commercial lithotripters for kidney stones. *Ultrasound in Medicine and Biology*, 21(2):259–272, 1989.

[11] J. Van Cauwelaert. Use of micro-computed tomography to follow the progression of crack formation in artificial and human kidney stones during shock wave lithotripsy. *M. S. Thesis*, Boston University, September 2004.

[12] D. Cathignol, A. Birer, S. Nachef, and J. Chapelon. Electronic beam steering of shock waves. *Ultrasound in Medicine and Biology*, 21(3):365–377, 1995.

[13] C. Chaussy, W. Brendel, and E. Schiemdt. Extracorporeally induced destruction of kidney stones by shock waves. *The Lancet*, 2:1265–1268, December 1980.

[14] P. V. Chitnis. Characterization and comparative analysis of extracorporeal shock wave devices. *M. S. Thesis*, Boston University, September 2002.

[15] P. V. Chitnis and R. O. Cleveland. Quantitative measurements of acoustic emissions from cavitation at the surface of a stone in response to a lithotripter shock wave. *Journal of the Acoustical Society of America*, 119(4):1929–1932, 2006.

[16] C. J. Chuong, P. Zhong, G. M. Preminger. A comparison of stone damage caused by different modes of shock wave generation. *Journal of Urology*, 148:200–205, July 1992.

[17] C. C. Church. A theoretical study of cavitation generated by an extracorporeal shock wave lithotripter. *Journal of the Acoustical Society of America*, 86(1):215–227, July 1989.

[18] R. O. Cleveland and J.A. McAteer, in press. The Physics of Shock Wave Lithotripsy. In A. D. Smith, G. H. Badlani, D. H. Bagley, R. V. Clayman, S. G. Docimo, G. H. Jordan, L. R. Kavoussi, B. R. Lee, J. E. Lingeman, G. M. Preminger, J. W. Segura, editors, *Smith's Textbook on Endourology*, Chap. 38, pp. 317-332, BC Decker Inc., Hamilton, ON, Canada, 2007.

[19] R. Cleveland and O. Sapozhnikov. Modeling elastic wave propagation in kidney stones with application to shock wave lithotripsy. *Journal of the Acoustical Society of America*, submitted July 2005.

[20] R. O. Cleveland, O. A. Sapozhnikov, M. R. Bailey, L. A. Crum. A dual passive cavitation detector for localized detection of lithotripsy–induced cavitation in vivo. *Journal of the Acoustical Society of America*, 107(3):1745–1758, March 2000.

[21] W. T. Coakley. Acoustical detection of single cavitation events in a focused field in water at 1 MHz. *Journal of the Acoustical Society of America*, 49:792–801 1971.

[22] N. Cohen and H. Whitfield. Mechanical testing of urinary calculi. *World Journal of Urology*, 11:13–18, 1993.

[23] A. J. Coleman, J. E. Saunders, L. A. Crum, M. Dyson. Acoustic cavitation generated by an extracorporeal shock wave lithotripter. *Ultrasound in Medicine and Biology*, 13(2):69–76, 1990.

[24] A. J. Coleman, M. J. Choi, J. E. Saunders. Detection of acoustic emission from cavitation in tissue during clinical extracorporeal lithotripsy. *Ultrasound in Medicine and Biology*, 22:1079–1087, 1996.

[25] A. J. Coleman and J. E. Saunders. A survey of the acoustic output of commercial extracorporeal shock wave lithotripters. *Ultrasound in Medicine and Biology*, 15(3):213–227, 1989.

[26] A. J. Coleman, M. J. Choi, J. E. Saunders, and T. G. Leighton. Acoustic emission and sonoluminescence due to cavitation at the beam focus of an electrohydraulic lithotripter. *Ultrasound in Medicine and Biology*, 18(3):267–281, 1992.

[27] B. Conners, A. Evan, L. Willis. The effect of discharge voltage on renal injury and impairment caused by lithotripsy in the pig. *Journal of the American Society of Nephrology* 11:310–318, 2000.

[28] L. A. Crum. Cavitation microjets as a contributory mechanism for renal calculi disintegration in ESWL. *Journal of Urology*, 140:1587–1590, 1988.

[29] G. Delacretaz, K. Rink, G. Pittomvils, J. P. Lafaut, H. Vandeursen, and R. Boving. Importance of the implosion of eswl-induced cavitation bubbles. *Ultrasound in Medicine and Biology*, 21(1):97–103, 1995.

[30] M. Delius, W. Brendel, and G. Heine. A mechanism of gallstone destruction by extracorporeal shock waves. *Naturwissenschaften*, 75:200–201, 1988.

[31] M. Delius, G. Enders, Z. Xuan. Biological effects of shock waves: kidney damage by shock waves in dogs–dose dependance. *Ultrasound in Medicine and Biology*, 14:117–122, 1988.

[32] M. Delius, M. Jordan, H. Eizenhoefer. Biological effects of shock waves: kidney hemorrhage by shock waves in dogs–rate dependance. *Ultrasound in Medicine and Biology*, 14:689–694, 1988.

[33] M. Delius. Minimal static excess pressure minimises the effect of etracorporeal shock waves on cells and reduces it on gall stones. *Ultrasound in Medicine and Biology*, 23(4):611–617, 1997.

[34] M. Delius, R. Denk, C Berding, G Heine, H. Liebich, M. Jordan, W. Brendel. Biological effects of shock waves: Cavitation by shock waves in piglet liver. *Ultrasound in Medicine and Biology*, 13(2):69–76, 1987.

[35] C. Devevey, F. Denis, and G Gimenez. Real time tracking of gallstones on ultrasonic images for extracorporeal lithotripsy. In: B. R. McAvoy, ed. *IEEE Ultrasonic Symposium*, vol. 2. Tucson; 1992:226–231.

[36] W. Eisenmenger. The mechanisms of stone fragmentation in ESWL. *Ultrasound in Medicine and Biology*, 27:683–693, January 2001.

[37] W. Eisenmenger, X. Du, C. Tang, S. Zhao, Y. Wang, F. Rong, D. Dai, M. Guan, and A. Qi. The first clinical results of the "wide–focus and low–pressure "ESWL. *Ultrasound in Medicine and Biology*, 28(6):769–774, 2002.

[38] A. P. Evan, L. A. Willis, J. McAteer. Kidney damage and renal functional changes are minimized by waveform control that suppresses cavitation in shock wave lithotripsy. *Journal of Urology*, 168:1556–1562, 2002.

[39] A. P. Evan and J. A. McAteer. Q-Effects of shock wave lithotripsy. In F. Coe, et al., editors, *Kidney Stones: Medical and Surgical Management*, pages 549–570. Raven Press, New York, 1996.

[40] A. P. Evan and J. A. McAteer. Current perspectives on shock wave lithotripsy adverse effects. In James E. Lingeman and Glenn M. Preminger, editors, *New Developments in the Management of Urolithiasis*, pages 3–20. Igaku–Shoin, New York, 1996.

[41] A. P. Evan and L. R. Willis. Extracorporeal Shock Wave Lithotripsy: Complications. In A. D. Smith, G. H. Badlani, D. H. Bagley, R. V. Clayman, S. G. Docimo, G. H. Jordan, L. R. Kavoussi, B. R. Lee, J. E. Lingeman, G. M. Preminger, J. W. Segura, editors, *Smith's Textbook on Endourology*, Chap. 41, pp. 353-365, BC Decker Inc., Hamilton, ON, Canada, 2007.

[42] P. M. Gammell and G. R. Harris. IGBT based kilovoltage pulsers for ultrasound measurement applications. *IEEE Transactions on Ultrasonics, Ferroelectrics, and Frequency Control*, 50(12):1722–1728, 2003.

[43] Gilmore F. R. The growth or collapse of spherical bubble in a viscous compressible liquid. *Office of Naval Research, Report No. 26-4*, April 1952.

[44] R. K. Gould. Rectified diffusion in the presence of, and absence of, acoustic streaming. *Journal of the Acoustical Society of America*, 56(6):1740–1746, December 1974.

[45] S. M. Gracewski, G. Dahake, Z. Ding, S. J. Burns, and E. C. Everbach. Internal stress wave measurements in solids subjected to the lithotripter pulses. *Journal of the Acoustical Society of America*, 94:652–661, August 1993.

[46] International Electrotechnical Committee, "Ultrasonics – pressure pulse lithotripters – characteristics of fields," IEC standard: 61846, 1998.

[47] A Ishida. A lithotripsy apparatus having a missed-shot preventative function. *Patent No. 0461 479 A1*, 1991.

[48] A Ishida. Apparatus for destroying calculi. *Patent No. 0 336 620 A2*, 1989.

[49] G. Janetschek, F. Frauscher, and R. Knapp. New onset hypertension after extracorporeal shock wave lithotripsy: age related incidence and prediction by resistive index. *Journal of Urology*, 158:346-351, 1997.

[50] D. Jocham, C. Chaussy, and E. Schmiedt. Extracorporeal shock wave lithotripsy. *Urology International*, 41:357–368, 1986.

[51] A. R. Kaiser, C. A. Cain, E. Y. Hwang, J. B. Fowlkes, and R. J. Jeffers. A cost effective degassing system for use in ultrasonic measurements: The multiple pinhole degassing (mpd) system. *Journal of the Acoustical Society of America*, 99(6):3857–3859, 1996.

[52] J. V. Kaude. Renal morphology and function immediately after extracorporeal shock-wave lithotripsy. *American journal of Roentology* 145:305–313, 1985.

[53] K. Kerbl, J. Rehman, and J. Landman. Current management of urolithisasis: progress or regress? *Journal of Endourology* 16:281–288, 2002.

[54] A. Krambeck, M. Gettman, and A. Rohlinger. DIabetes mellitus and hypertension associated with shock wave lithotripsy or renal and proximal ureteral stones. *Journal of Urology*, 175:1742-1747-351, 2006.

[55] T. Leighton. *The Acoustic Bubble*, pages 531–545. Academic Press, Boston, 1997.

[56] P. Lewin, J. Chapelon, J. Mestas, A. Birer, and D. Cathignol. A novel method to control $P+/P-$ ratio of the shock wave pulses used in the extracorporeal piezoelectric lithotripsy (PEL). *Ultrasound in Medicine and Biology*, 16(5):473–488, 1990.

[57] J. E. Lingeman. Lithotripsy Systems. In A. D. Smith, G. H. Badlani, D. H. Bagley, R. V. Clayman, S. G. Docimo, G. H. Jordan, L. R. Kavoussi, B. R. Lee, J. E. Lingeman, G. M. Preminger, J. W. Segura, editors, in press *Smith's Textbook on Endourology*, Chap. 39, pp. 333-342, BC Decker Inc., Hmailton, ON, Canada, 2007.

[58] J. E. Lingeman. Extracorporeal shock wave lithotripsy devices: Are we making progress? In James E Lingeman and Glenn M Preminger, editors, *New Developments in the Management of Urolithiasis*, pages 21–40. Igaku–Shoin, New York, 1996.

[59] D. Liu and R. Waag. Propagation and backpropagation for ultrasonic wavefront design. *IEEE Trans. Ultrasonics, Ferroelectrics, and Frequency Control*, 44(1):1–13, January 1997.

[60] H. Lokhandwalla, J. McAteer, J. Williams, B. Sturtevant. Mechanical hemolysis in shock wave lithotripsy (SWL). *Physics in Medicine and Biology*, 46:1245-1264, 2001.

[61] A. Loske, F. Prieto,F. Fernandez, J. Cauwelaert. Tandem shock wave cavitaiton enhancement for extracorporeal lithotripsy. *Physics in Medicine and Biology*, 47:3945–3957, 2002.

[62] D. Marquardt. An Algorithm for Least-Squares Estimation of Nonlinear Parameters *SIAM Journal of Applied Mathematics*, 11: 431441, 1963.

[63] A. D. Maxwell, O. A. Sapozhnikov, and M. R. Bailey. A PVDF membrane hydrophone for accurate measurement of medical shock waves. *IEEE Ultrasonics Symposium* (Vancouver BC Canada October, 2006) submitted.

[64] J A. McAteer, J.C. Williams, Jr., R.O. Cleveland, J. Van Cauwelaert, M.R. Bailey, D.A. Lifshitz, A.P. Evan. Ultracal-30 gypsum artificial stones for lithotripsy research. *Urology Research*, 2005.

[65] P. Morse and K. Ingard. *Theoretical Acoustics.* Princeton: Princeton University Press, 1986, Ch. 14.

[66] Y. A. Pischalnikov, O. A. Sapozhnikov, M. R. Bailey. Cavitation bubble cluster activity in the breakage of kidney stones by lithotripter shock waves. *Journal of Endourology*, 17:435–446, 2003.

[67] Y. A. Pischalnikov, O. A. Sapozhnikov, M. R. Bailey, I. V. Pischalnikov, J. C. Williams, and J. A. McAteer. Cavitation selectively reduces the negative-pressure phase of lithotripters. *Acoustics Research Letters Online*, 6(4):280–286, November 2005.

[68] R. E. Riedlinger. Self–focusing piezoelectric high–power sound–pulser for painless disintegration of urinary canal. *Ultrasonics International 87 Conference Proceedings*, 220–225.

[69] O. A. Sapozhnikov, M.R. Bailey, L. A. Crum. Ultrasound guided localized detection of cavitation during lithotripsy in pig kidney in vivo. *IEEE Ultrasonics Symposium*, 1347–1350, 2001.

[70] W. Sass, M. Braunlich, H. Dreyer, E. Matura, W. Folberth, H. Priesmeyer, and J. Seifert. The mechanism of stone disintegration by shock waves. *Ultrasound in Medicine and Biology*, 17(3):239–243, 1991.

[71] M. Schafer and P. Lewin. Transducer characterization using the angular spectrum method. *Journal of the Acoustical Society of America*, 85(5):2202–2214, May 1989.

[72] L. H. Smith. Overview of Urolithiasis. *Journal of Urology*, 141(2):707–710, March 1989.

[73] . Use of a dual-pulse lithotripter to generate a localized and intensified cavitation field. *Journal of the Acoustical Society of America*, 110(3):1685–1695, 2001.

[74] D. Sokolov, M. Bailey, L. Crum. Dual pulse lithotripter accelerates stone fragmentation and reduces cell lysis *in vitro*. *Ultrasound in Medicine and Biology*, 29(7):1045–1052, 2003.

[75] J. Staudenraus and W. Eisenmenger. Fiber-optic probe hydrophone for ultrasonic and shock–wave measurements in water. *Ultrasonics*, 31(4)267:273, 1993.

[76] P. Stephanishen and K. Benjamin. Forward and backward projection of acoustic fields using FFT methods. *Journal of the Acoustical Society of America*, 71(4):803–812, April 1982.

[77] P. Stephanishen. The relationship between the impulse response and angu;lar spectrum methods to evaluate acoustic transient fields. *Journal of the Acoustical Society of America*, 90(5):2794–2798, April 1991.

[78] B. Sturtevant. Shock wave physics of lithotripters. In A. D. Smith et al., editor, *Smith's Textbook of Endourology*, 529–592. Quality Medical Publishing, 1996.

[79] M. Tanter, J. Aubry, J. Gerber, J. Thomas, and M. Fink. Optimal focusing by spatio-temporal inverse filter. I Basic principles. *Journal of the Acoustical Society of America*, 110(1):37–47, July 2001.

[80] J. Thomas, F. Wu, and M. Fink. Self focusing on extended objects with time reversal mirror, application to lithotripsy. *IEEE Ultrasonic Symposium*, 1994:1809–1814.

[81] F. Ueberle. Location of kidney stones for non-invasive piezoelectric lithotripsy. *Ultrasonics International 1987 Conference Proceedings*, London:Butterworth; 1987:226–231.

[82] A. Vogel and W. Lauterborn. Acoustic transient generation by laser–produced cavitation bubbles near solid boundaries. *Journal of the Acoustical Society of America*, 84(2):719–731, 1988.

[83] O. Wess and A. Feige. Introduction to the physics and technology of extracorporeal shock wave therapy (ESWT). Storz Medical AG, Kreuzlingen, Switzerland, February 1997.

[84] L. Willis, A. Evan, J. Lingeman. The impact of high dose lithotripsy on renal function. *Contemporary Urology* 45–50, 1999.

[85] L. Willis, A. Evan, B. Conners. Prevention of lithotripsy-induced renal injury by pretreating kidneys with low energy shock waves. *Journal of the American Society of Nephrology* 17:663–673, 2006.

[86] X. Xi and P. Zhong. Improvement of stone fragmentation during shock-wave lithotripsy using a combined EH/PEAA shock wave generator-in vitro experiments. *Ultrasound in Medicine and Biology*, 26(3):457–467, 2000.

[87] X. Xi and P. Zhong. Dynamic photoelastic study of the transient stress fields in solids during shock wave lithotripsy. *Journal of the Acoustical Society of America*, 109(3):1226–1239, 2001.

[88] C. Zarse, J. McAteer, M. Taan, A. Sommer. S. Kim, R. Paterson, E. Hatt, J. Lingeman, A. Evan, and J. Williams, Jr. Helical computer tomography accurately reports urinary stone compostition using attenuation values: in vitro verification using high-resolution micro-computed tomography calibrated to fourier transform infrared microspectroscopy. *Journal of Urology*, 63(5):828–833, 2004.

[89] P. Zhong, I. Cionta, F. Cocks, G. Preminger. Inertial cavitation and associated acoustic emission produced during electrohydraulic lithotripsy. *Journal of the Acoustical Society of America*, 101:2940–2950, 1997.

[90] P. Zhong, Y. Zhou, S. Zhu. Dynamics of bubble oscillation in constrained media and mechanisms vessel rupture in SWL. *Ultrasound in Medicine and Biology*, 27:119–134, 2001.

[91] P. Zhong and Y Zhou. Suppression of large intraluminal bubble expansion in shock wave lithotripsy without compromising stone comminution: Methodology and in vitro experiments . *Journal of the Acoustical Society of America*, 110:3283–3291, May 2001.

[92] S. Zhu, F Cocks, G. Preminger, and P. Zhong. The role of stress waves and cavitation in stone comminution in shock wave lithotripsy. *Ultrasound in Medicine and Biology*, 28(5):661–671, 2002.

[93] S. Zhu, T. Dreyer, M. Liebler, and P. Zhong. Effects of an acoustic diode on lithotripter shock wave, cavitation, and stone fragmentation. *Journal of the Acoustical Society of America*, 111(5):2461, May 2002.

[94] S. Zhu and P. Zhong. Effects of an acoustic diode on the pressure waveform and cavitation bubble dynamics produced by a piezoelectric shock wave generator. *Journal of the Acoustical Society of America*, 114(4):2466, October 2003.

VITA

Parag Vijay Chitnis

Boston University
Department of Aerospace and Mechanical Engineering
110 Cummington Street, Boston, MA 02215
(617) 823-8312, pchitnis@bu.edu

RESEARCH INTERESTS

Shock wave therapy
High intensity focused ultrasound
Time reversal acoustics
Ultrasound-mediated drug delivery

EDUCATION

Ph.D. Mechanical Engineering, Boston University, Boston, MA, expected August 2006 Thesis: Application of a Piezoelectric Phased Array for Studying Stone Fragmentation Mechanisms in Shock Wave Lithotripsy

M.S. Mechanical Engineering, Boston University, Boston, MA, 2002 Thesis: Characterization and Comparative Analysis of Extracorporeal Shock Wave Devices

B.S. Engineering Physics and Mathematics, WV Wesleyan College, Buckhannon, WV, 2000

ACADEMIC PROJECTS

Physical Acoustics Laboratory, Boston University, 2000-present

Investigating mechanisms of kidney stone fragmentation through control of waveform shape and spatial pressure distribution by means of a phased array shock wave source (Doctoral thesis)

Compared in vitro acoustic pressure and cavitation fields of electrohydraulic and ballistic orthopedic shock wave therapy devices

Compared in vitro stone fragmentation, acoustic pressure and cavitation fields for electrohydraulic and electromagnetic lithotripters

Developed a Matlab algorithm for analyzing stone fracture images using edge detection techniques

Department of Physics and Engineering, West Virginia Wesleyan College, 1999-2000

Developed a system for determining the frequencies of molecular vibrations using Fourier Transform Infrared Spectroscopy

POSITIONS HELD

Research Assistant, Physical Acoustic Laboratory, Boston University, 2001-present

Characterized various shock wave therapeutic devices and investigated the mechanisms of stone fragmentation in extracorporeal shock wave lithotripsy

Teaching Assistant, Boston University

AM 310, Instrumentation and Theory of Experiments, 2002

AM 308, Structural Mechanics, 2000

Conducted discussion sessions, laboratory sessions and graded experimental reports

Student Council member, Acoustical Society of America, 2001 2003

Planned activities and addressed issues related to all aspects of student participation Developed an ASA mentor award to foster and award mentoring within the society

HONORS/AWARDS

Best Student Paper Award for the Acoustical Society of America, 2002, 2005

ASA/NCPA/ONR Physical Acoustics Summer School Fellowship, 2004

Distinguished Student Award of Mathematics Department, WV Wesleyan College, 2000

Presidential Scholarship, WV Wesleyan College, 1996-2000

PROFESSIONAL AFFILIATION

Acoustical Society of America

International Society of Therapeutic Ultrasound

PEER-REVIEWED PUBLICATIONS

Chitnis, P. V. and Cleveland, R. O., Quantitative measurements of acoustic emissions from cavitation at the surface of a stone in response to a lithotripter shock wave. J. Acoust. Soc. Am. 119(4), 1929-1932, April 2006

Chitnis, P. V. and Cleveland, R. O., The acoustic and cavitation fields of an encapsulated electrode lithotripter. Acoustics Research Letters Online. (in preparation)

Chitnis, P. V., Cleveland, R. O., Pishchalnikov, Y. and Mcateer, J., Comparison acoustic fields and stone fragmentation between an electrohydraulic and electromagnetic lithotripter. Ultrasound in Medicine and Biology. (in preparation)

Cleveland, R. O., Gerbus, B. D. Chitnis, P. V. and Mcateer, J. A., In vitro assessment of an encapsulated electrode for electrohydraulic shock wave lithotripsy. Journal of Urology. (in preparation)

CONFERENCE PROCEEDINGS

Chitnis, P. V. and Cleveland, R. O., Acoustic and cavitation fields of shock wave therapy devices. 5th International Symposium of Therapeutic Ultrasound. 2005 (in press)

ORAL PRESENTATION ABSTRACTS

Chitnis, P. V. and Cleveland, R. O., Customization of acoustic output in lithotripsy using a piezoelectric transducer array. J. Acoust. Soc. Am. 119:3407, 2006.

Chitnis, P. V. and Cleveland, R. O., Measuring bubble dynamics in lithotripsy using a high speed camera. J. Acoust. Soc. Am. 119:3407, 2006.

Cleveland, R. O. and Chitnis, P. V., The acoustic fields of shock wave therapy devices. J. Acoust. Soc. Am. 117:2383, 2005.

Chitnis, P. V. and Cleveland, R. O., Secondary shock wave emission from cavitation in lithotripsy. J. Acoust. Soc. Am. 117:2372, 2005.

Chitnis, P. V. and Cleveland, R. O., Comparison between an open-cage electrode lithotripter and an encapsulated electrode lithotripter. J. Acoust. Soc. Am. 115:2562, 2004.

Cleveland R. O., Chitnis, P. V., Gerbus, B. and Mcateer, J., An in vitro comparison of open-cage and encapsulated electrodes in shock wave lithotripsy (SWL). European Urology Supplements. 3(2): 235, 2004.

Chitnis, P. V., Cauwelaert J. and Cleveland, R. O., Simultaneous measurements of the cavitation and acoustic fields of an electrohydraulic lithotripter. J. Acoust. Soc. Am. 114:2464, 2003.

Cleveland, R. O. and Chitnis, P. V., Acoustic and cavitation fields produced by shock wave therapy (SWT) devices with different generating principles. J. Acoust. Soc. Am. 114:2464, 2003.

Chitnis, P. V. and Cleveland, R. O., Comparison of the cavitation fields of an electromagnetic and electrohydraulic lithotripter. J. Acoust. Soc. Am. 112:2291, 2002.

Chitnis, P. V. and Cleveland, R. O., Acoustic and cavitation field of an orthopedic shock wave device HMT Equitron. J. Acoust. Soc. Am. 110:2614, 2001.

Cleveland, R. O., Chitnis, P. V., Anglade, R., and Babayan, R. K. Measurements of the pres-sure field and in vitro stone fragmentation of a Storz Modulith SLX lithotripter. J. Acoust. Soc. Am. 109:2482, 2001.

STUDENT MENTORING

Brad Gerbus, undergraduate research assistant 2003-present

Molly Johnson, REU student 2003

Summer Gibbs, REU student 2002

Sam Ratterman, REU student 2001